ABSTRACT

BROWNE, MICHAEL CHARLES. Preparation for Deployment of the Neutral Current Detectors (NCDs) for the Sudbury Neutrino Observatory (SNO). (Under the direction of John F. Wilkerson and Christopher R. Gould.)

The Sudbury Neutrino Observatory (SNO) is the latest generation of solar neutrino experiments designed to investigate the Solar Neutrino Problem (SNP). Through detection of all flavors of neutrinos, SNO will be capable of testing the neutrino oscillation hypothesis as a solution to the SNP. This unique capability stems from the flavor independent $\nu_x(^2H, n\ \nu_x)^1H$ reaction ($\nu_x = \nu_e$ or ν_μ or ν_τ). Observation of this Neutral Current (NC) reaction is through detection of the free neutron. One method of detection utilizes an array of ^{3}He-filled proportional counters, and is called the Neutral Current Detector array (NCD array).

This thesis describes the preliminary testing and characterization of the individual counter components of the array during an underground storage period at the SNO site. These tests were performed to verify the operational characteristics of the counters, assess the long-term stability of the counters, and measure potential backgrounds to the NC measurement in SNO. In addition, a measure of the underground thermal neutron flux was made. The measurements to characterize the counters and assess the background contamination levels required the development of data acquisition electronics and analysis routines.

Potential backgrounds to the NC measurement can be grouped into two

categories: events intrinsic to the counters that arise from the decays of naturally occurring radioactive isotopes contained in the NCD construction materials, and photodisintegration neutrons that arise from radioactive impurities in the SNO detector and NCD counters. Measurements taken for this thesis work were aimed at determining the level of ^{238}U, ^{232}Th, ^{210}Po, and daughter isotopes in the NCD counters. An estimation of the total NC measurement background is included in this work based on measurements of this contamination.

**PREPARATION FOR DEPLOYMENT OF THE
NEUTRAL CURRENT DETECTORS (NCDs)
FOR THE
SUDBURY NEUTRINO OBSERVATORY (SNO)**

by

MICHAEL CHARLES BROWNE

A dissertation submitted to the Graduate Faculty of
North Carolina State University
in partial fulfillment of the
requirements for the Degree of
Doctor of Philosophy

PHYSICS

Raleigh

1999

APPROVED BY:

_____   _____

_____   _____
Co-chair of Advisory Committee   Co-chair of Advisory Committee

To my parents

The truth knocks on the door and you say, "Go away, I'm looking for the truth," and so it goes away. Puzzling.

Robert M. Pirsig
Zen and the Art of Motorcycle Maintenance

But when one is young one must see things, gather experience, ideas; enlarge the mind.

Joseph Conrad
Heart of Darkness

Biography

Michael C. Browne

Current Address:	**Home Address:**
The University of Washington	3833 23rd Ave W.
Nuclear Physics Laboratory	Seattle, WA 98199
Seattle, WA 98195	(206) 282-9607
(206) 543-4035	
mcbrowne@npl.washington.edu	

Birthdate:

October 1, 1970; Pottstown, Pennsylvania

Education:

1992	B.A., Physics, Franklin and Marshall College
1999(expected)	Ph.D., Physics, North Carolina State University
	Thesis Title: "Preparation for Deployment of the Neutral Current Detectors for the Sudbury Neutrino Observatory"
	Thesis Directors: Prof. John F. Wilkerson (UW) and Prof. Chris Gould (NCSU)

Positions:

1988-92	Teaching Assistant, Franklin and Marshall College
	Student Technician - Electronics, Franklin and Marshall College
1990-92	Undergraduate Student Research Program, Los Alamos National Laboratory
1992-95	Teaching Assistant, North Carolina State University, Graduate Research Assistant Program, Los Alamos National Laboratory
1995-	Research Assistant, University of Washington - Nuclear Physics Laboratory
	Tandem Accelerator Operator, University of Washington - Nuclear Physics Laboratory

Professional Societies:

Member, American Physical Society
Member, The Institute of Electrical and Electronics
Engineers (IEEE)

Abstracts:

T.D. Steiger, M.C. Browne, S.R. Elliott, R.G.H. Robertson, J.F. Wilkerson, J. Anaya, T.J. Bowles, G.L. Greene, W.A. Teasdale, J. Adams, M.S. Dewey, D. Gilliam, G.L. Jones, J.S. Nico, A.K. Thompson, F.E. Wietfeldt, S.J. Freedman, B.K. Fujikawa, L.J. Lising, E.G. Wasserman, K.P. Coulter, T.E. Chupp, S.-R. Hwang, and A. Garcia; "Time Reversal in Polarized Neutron Decay---A Progress Report on the emiT Experiment," Bulletin of the American Physical Society 42, 1627 (1997).

L.J. Lising, S.J. Freedman, B.K. Fujikawa, E.G. Wasserman, M.C. Browne, S.R. Elliott, R.G.H. Robertson, T.D. Steiger, J.F. Wilkerson, J.M. Adams, G.L. Jones, M.S. Dewey, J.S. Nico, A.K. Thompson, F.E. Wietfeldt, T.E. Chupp, K.P. Coulter, S.-R. Hwang, A. Garcia, J.M. Anaya, T.J. Bowles, G.L. Greene, and W.A. Teasdale; "Time Reversal in Polarized Neutron Decay---Theory and Analysis for the emiT Experiment," Bulletin of the American Physical Society 42, 1627 (1997).

S.R. Elliott, M.C. Browne, P.J. Doe, C. Duba, J.V. Germani, K.M. Heeger, A.W.P. Poon, R.G.H. Robertson, M. Smith, T.D. Steiger, J.F. Wilkerson, R.W. Ollerhead, K.T. Lesko, R.G.Stokstad, T.J. Bowles, S.J. Brice, E.I. Esch, M.M. Fowler, A. Goldschmidt, A. Hime, G.G. Miller, P.M. Thornewell, J.B. Wilhelmy, and J.M. Wouters; "The Neutral Current Detector Project of the Sudbury Neutrino Observatory," Bulletin of the American Physical Society 42, 1631 (1997).

S-R Hwang, T.E. Chupp, K.P. Coulter, M.C. Browne, P.H. Mumm, R.G.H. Robertson, T.D. Steiger, J.F. Wilkerson, S.J. Freedman, B.K. Fujikawa, L.J. Lising, E.G. Wasserman, J.M. Adams, M.S. Dewey, D. Gilliam, G.L. Jones, J.S. Nico, A.K. Thompson, F.E. Wietfeldt, A. Garcia, J.M. Anaya, T.J. Bowles, G.L. Greene, and W.A. Teasdale; "Time Reversal in Polarized Neutron Decay---Data Analysis Issues for the emiT Experiment," Bulletin of the American Physical Society (1998).

Other Publications:

A.W.P. Poon, M.C. Browne, R.G.H. Robertson, C.E.Waltham,
and N. Kherani; "Development of a compact 20 MeV gamma-ray source
for energy calibration at the Sudbury Neutrino Observatory" Particles
and Cosmology (World Scientific, 1996)

Publications in Preparation:

M.C. Browne, M. Hindman, A. Myers, S.M. Newcomer, J. Nico,
R.G.H. Robertson, T.D. Steiger, R. VanBerg, T.D. VanWechel, J.F.
Wilkerson; "VME-Based Shaper/Peak-Detect ADC Board" to be
submitted to Nuclear Instruments and Methods

M.C. Browne, T.J. Bowles, S.J. Brice, P.J. Doe, C.A. Duba, S.R. Elliott,
E.I.Esch, M.M. Fowler, J.V. Germani, A. Goldschmidt, K.M. Heeger,
A. Hime,K.T. Lesko, G.G. Miller, R.W. Ollerhead, A.W.P. Poon,
R.G.H. Robertson, M.W.E. Smith, T.D. Steiger, R.G. Stokstad,
P.M. Thornewell, J.B. Wilhelmy, J.F. Wilkerson , J.M. Wouters; "Low-
background ^{3}He Proportional Counters for Use in the Sudbury Neutrino
Observatory" submitted to Transactions in Nuclear Physics

Acknowledgements

The realization that my graduate career is about to end didn't hit home until I started to think about how many people have helped me to get here. It is at the same time wonderful to have interacted with so many individuals, and frightening to think that I have been in graduate school so long that I have interacted with so many individuals…

The foundation of this work has been my research group. When I joined as an undergraduate nearly 10 years ago, I was fortunate to be mentored by a core of individuals who were simultaneously excellent physicists, and exceptional people. My primary advisor, John Wilkerson, has provided me with years of advise and knowledge for which I am deeply indebted. Hamish Robertson, Steve Elliott, Peter Doe, Andrew Hime, and Tom Bowles have likewise been an incredible source of information, and have all contributed to whatever skills I may claim as a physicist. I would like to additionally thank Andrew for many enjoyable conversations throughout my graduate career. The analysis work led by him at Los Alamos is the foundation on which the content of this thesis was built.

I have been extremely fortunate in that I have been able to work with people from many institutions and labs over the years. At Los Alamos alone, I have had the great pleasure of meeting and working with many varied characters. Mel Anaya, Bill Teasdale, Pete Thornewell, Frank McGirt, Miles

facility is based on the quality of the individuals both professionally and personally. Believe me, NPL has a ton of personality…

One individual in particular was paramount to my well-being. Throughout some of the darkest days, Christina has been there for me. I certainly would not be writing any acknowledgements if it weren't for her ever-present support. Few people recognize that sometimes the best thing you can do to help someone is stand nearby and leave them alone. Christina, thank you for every day - no exceptions. For all the times you sent me to my basement to tinker with the bikes, for every time you sent me to the mountains to ride, and for every time you simply listened to me - Thank You.

The bulk of the data for this thesis work is the result of much time spent in Sudbury over the past few years. While on site, many people helped to make it all possible, with special thanks to Hardy Seifert for the many and varied roles he has played in ensuring the success of the NCDs.

Finally, thanks to my family. They may be the only people whose joy surpasses my own about finally getting out of school. They have provided unwavering support throughout my graduate career - wherever it took me. Thanks guys!

TABLE OF CONTENTS

Page

LIST OF TABLES

LIST OF FIGURES

Chapter 1

1.1 Introduction to Neutrinos and the Solar Neutrino Problem

In the early 1900s   decay was presumed to result in the emission of a single monoenergetic particle, as had been previously observed in alpha decay. However, in 1914, the   spectra of ^{214}Pb and ^{214}Bi were determined to be continuous [1]. In order to reconcile this apparent violation of linear and angular momentum, as well as energy, Pauli proposed the existence of a neutral spin-1/2 particle which carried away part of the energy in the decay process [2]. In the absence of experimental observation of such a particle, its existence was debated for many years, with opinion in the physics community divided over the issue: "Not everyone would be willing to say that he believes in the existence of the neutrino but it is safe to say that there is hardly one of us who is not served by the neutrino hypothesis in   decay" - H.R. Crane [3].

The first tests designed to look for evidence of the neutrino involved a determination of the recoil energy of the nucleus in the ^{7}Be and ^{37}Ar inverse decay systems [4,5]. According to the Fermi-Pauli theory of   decay, a single neutrino would be emitted after these nuclei capture an outer-shell electron as shown in Equation 1.1.

$$^{37}\text{Ar} + e^{-} \quad ^{37}\text{Cl} + \quad_{e} \quad (Q = 816\text{keV}) \tag{1.1}$$

By conservation of momentum, the nuclei in this process should then have a monoenergetic recoil spectrum. In the ^{37}Ar experiment the nuclear recoil

spectrum was measured by a time-of-flight method. The nucleus captures a k-shell electron resulting in the emission of a neutrino, and the recoil of the ^{37}Cl nucleus in an excited state. The excited ^{37}Cl decays to the ground state by emission of an Auger electron which is tagged for the beginning of the time-of-flight measurement. The detection of the ionized ^{37}Cl nucleus ends the timing measurement, and is used to determine the recoil energy. These experiments did yield monoenergetic recoil spectra, which is consistent with the theoretical construct of single neutrino emission. While this was an important step towards understanding the -decay process, the neutrino had still not been directly observed.

In 1953, Reines and Cowan began a series of reactor-based experiments [6,7] looking for the positron and neutron products of the inverse   decay of protons as shown in Equation 1.2.

$$\bar{\nu}_e + p \rightarrow e^+ + n \tag{1.2}$$

Their target was a cadmium-doped, hydrogenous liquid scintillator. The initial experiments were carried out at the Hanford Engineering Works in Hanford, Washington. At the time, this was the largest fission reactor, and therefore would be the largest source of antineutrinos[1]. The positron would annihilate with electrons in the target, resulting in the emission of gammas. Photomultiplier tubes surrounding the target detected the photons from the gamma scintillations. The neutron would scatter and thermalize, eventually being captured by the

---
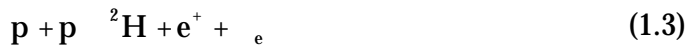
[1] For several years prior to 1953, Reines and Cowan intended to use a 20-kiloton fission bomb as the source of antineutrinos. Eventually, they decided that it would it be easier to reduce background events from a "controlled" source.

cadmium in the target. This capture resulted in the emission of gammas which also gave rise to scintillation photons. Neutron capture was therefore observed as a time-delayed signal in coincidence with the positron annihilation. Reines and Cowan observed a rate dependent on reactor power, but a factor of 50 higher than the theoretically predicted rate. Attempts to limit external background coincidences were unsuccessful, leading the team to believe that the additional signal was due to cosmic ray interactions in the target.

The next year, Reines and Cowan developed a new detector design which would better differentiate the anticipated signal from cosmic components. The new detector was segmented into two target volumes sandwiched by three scintillation detectors. This spacially separated target volume could veto the more energetic cosmic interactions by discriminating against events which deposited energy in all three scintillation detectors. The new system was installed at the recently-constructed Savannah River Plant reactor which was even more powerful than the Hanford reactor. The experiment was run for over 1100 hours and once again the anticipated delayed coincidence signal was observed, but this time the ratio of signal to accidental coincidences was over 4 to 1. Based on these experiments, Reines and Cowan confirmed the existence of the neutrino in 1956.

The discovery of the neutrino had consequences beyond the confines of particle physics. Astrophysics, and in particular, stellar evolutionary theory, stood to benefit greatly from this discovery. In 1926 A. S. Eddington combined classical thermodynamics, radiation equilibrium, and atomic structure in his

book "The Internal Constitution of Stars." This was the first work suggesting that nuclear reactions were the source of the Sun's radiant energy. Twelve years later, Gamow published his work investigating stellar evolution and the specific reactions which could drive stellar fusion [8]. In the same year, Bethe and Critchfield published their monumental paper [9] reporting on the probability of the fusion of two protons under solar conditions. This critical first reaction is shown in Equation 1.3.

$$p + p \rightarrow {}^{2}H + e^{+} + \nu_{e} \tag{1.3}$$

By the late 1930's, the Fermi theory of β-decay was gaining acceptance, with the implication that neutrinos would be a by-product of the stellar fusion process. Now that the detection of neutrinos was technologically feasible, methods were available to test stellar theory.

The first detector specifically designed to look for solar neutrinos was based on Bruno Pontecorvo's 1946 suggestion to use chlorine as a target to observe the reaction in Equation 1.4.

$$\nu_{e} + {}^{37}Cl \rightarrow e^{-} + {}^{37}Ar \tag{1.4}$$

In 1955, Ray Davis developed this idea into an experiment by placing a 3800 l tank of CCl_4 19 ft below ground at Brookhaven National Laboratory. His first results placed an upper limit on the neutrino production from the Sun at 10^{14} neutrinos-cm^{-2}-s^{-1}. This result was greeted warmly at best, and interest in larger scale solar neutrino detectors was weak due to a limited understanding of the neutrino production reactions in the Sun. The chlorine experiment had a threshold of 0.86 MeV which was believed to be too high to observe the majority

4

of the neutrinos created by the Sun. Over the next few years however it was determined that solar neutrinos were produced at higher energies from the decay of ^{8}B. This information led Davis to construct a 615 metric ton chlorine detector in the Homestake Gold Mine in Lead, South Dakota. Concurrent with the construction and running of this experiment was work led by John Bahcall on predicting the solar neutrino production rates to which the experiment would be sensitive. In 1968, both the theoretical prediction and experimental results of the initial two runs were presented. The predicted capture rate for the Homestake experiment was determined to be between 8 and 29 SNU[2]. The observed rate however had an upper limit of 3 SNU.

Systematic uncertainties associated with both the predicted and experimental rates were studied, but no reconciliation was achieved. A second generation of detectors was designed and built to examine this apparent deficit (Section 1.4 describes these experiments in detail). Each of these successive experiments confirmed the initial Davis results: solar neutrino experiments simply do not detect as many neutrinos as predicted by solar models. This discrepancy has become known as the Solar Neutron Problem (SNP).

The disagreement between observed flux and the flux predicted by solar models was especially disturbing given the success of these models at predicting other stellar observables such as luminosity and pressure waves. Much effort has been devoted on both theoretical and experimental fronts towards the resolution of the SNP. The currently favored solution is a scenario in which the neutrino oscillates from one type to another which may not be detected by current

---

[2] SNU is a Solar Neutrino Unit, 1 SNU = 10^{-36} events per target atom per second.

neutrino observatories. A detailed description of this proposed solution is presented in Section 1.3.

1.2 Solar Models

Eddington's 1926 publication marked the beginning of modern stellar astrophysics. Until this time, stars were thought to have been powered by mechanical or radioactive sources. Eddington realized that the luminosity of the Sun could not have changed drastically since the formation of the Earth some 10^9 years ago, and subsequently, the Sun's radiant output would require an energy supply much more abundant than these sources. The Bethe and Critchfield publication in 1938 [9] showed that nuclear reactions were possible under "solar conditions," and that the energy released by such processes was consistent with the Sun's observed energy output.

By the early 1940s, most of the reactions which can occur at solar temperatures had been calculated. These reactions coupled with measured cross-sections developed into a modern solar model. By the end of the 1950s, computers had been employed to model stellar interiors, enabling the inclusion of smaller perturbations into the models.

A detailed calculation of the energy and neutrino production in stellar interiors requires numerically-intensive calculations. An understanding of stellar structure, however, can be obtained from the application of basic physics concepts, and balancing the necessary equations of state.

6

1.2.1 Formulation of a Solar Model

There are four basic equations used to model stellar interiors [10]. These equations essentially relate the energy production and transport to the chemical composition of the stellar interior.

$$\frac{dM(r)}{dr} = 4\pi r^2 \rho(r) \tag{1.5}$$

$$\frac{dL(r)}{dr} = 4\pi r^2 \rho(r) \; \epsilon(\rho, T) \tag{1.6}$$

$$\frac{dT}{dr} = -\frac{3}{4acT(r)^3}\frac{\kappa(r)}{4\pi r^2}\frac{L(r)}{} \tag{1.7}$$

$$\frac{dT}{dr} = (1 - \frac{1}{\gamma})\frac{T(r)}{P(r)}(-\rho(r)\frac{GM(r)}{r^2}) \tag{1.8}$$

Equation 1.5 describes the mass $M(r)$ contained within the star as a function of the interior density $\rho(r)$. Folded into the density is the interior pressure, temperature, and mean molecular mass; a measure of the ratio of hydrogen to helium to heavier elements. Equation 1.6 characterizes the nuclear energy production $L(r)$ in terms of the energy released $\epsilon(\rho,)$ per unit time by all nuclear reactions which occur at temperature T and density ρ. Equations 1.7 and 1.8 describe the energy transport by radiant and convective processes respectively, and are characterized by the stellar interior's opacity (κ), ratio of specific heats ($\gamma = c_p/c_v$), the gravitational constant (G), and the Stephan-Boltzmann radiation constant ($\sigma = ca/4$ where c=speed of light, a=7.65×10^{-16} Jm^{-3} K^{-4}).

The basic solar model is the application of these equations with boundary conditions obtained from observable quantities such as luminosity and the size of the star. The initial ratio of elemental constituents H:He:heavier elements of the stellar interior is then estimated based on observations of the atmospheres of stars. The model simulates the burning of hydrogen, and evolves by taking into account the production and subsequent use of heavier elements in the stellar fusion process. These input parameters are varied until the model predicts the observed luminosity and effective temperature for the star.
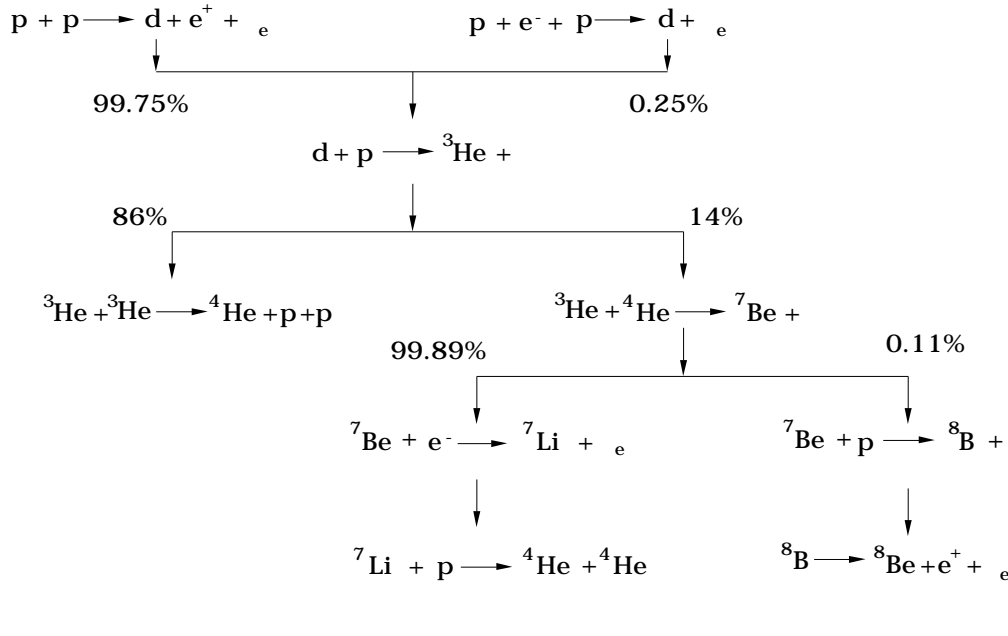
These solar model calculations suggest a correlation between a star's mass and energy production. This relationship, known as the mass-luminosity relation, was first noted by Eddington in 1924. Observational data taken since that time has confirmed the relation as illustrated by noting that the majority of stars populating the main sequence on H-R diagrams[3] adhere to the relationship. The ability of solar models to predict the observed macroscopic properties of a large percentage of the visible universe attests to the accuracy of the underlying physics and input parameters used in the models.

Applying these models to predict solar neutrino fluxes requires a much more detailed understanding of the specific reactions occurring in stellar interiors. The fusion of hydrogen into helium is the only known process by which the Sun could maintain its luminosity over the period of time indicated by both the fossil record and meteoric evidence. In the years since the original Bethe and Critchfield paper [9], alternate nuclear reactions that can occur under solar

---
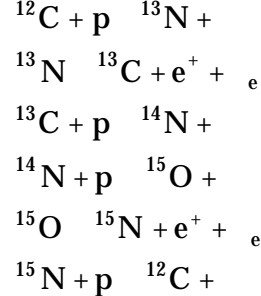
[3] Hertzsprung-Russell (H-R) Diagrams are graphical plots used to characterize large numbers of stars based on luminosity, mass, and spectral emission.

conditions have been considered, many of which contribute either negligibly or not at all. Figure 1.1 lists the primary reactions which are believed to drive energy and neutrino production in stars.

$$p + p \longrightarrow d + e^+ + \nu_e \qquad\qquad p + e^- + p \longrightarrow d + \nu_e$$

99.75% | 0.25%

$$d + p \longrightarrow {}^3He + \gamma$$

86% | 14%

$${}^3He + {}^3He \longrightarrow {}^4He + p + p \qquad\qquad {}^3He + {}^4He \longrightarrow {}^7Be + \gamma$$

99.89% | 0.11%

$${}^7Be + e^- \longrightarrow {}^7Li + \nu_e \qquad\qquad {}^7Be + p \longrightarrow {}^8B + \gamma$$

$${}^7Li + p \longrightarrow {}^4He + {}^4He \qquad\qquad {}^8B \longrightarrow {}^8Be + e^+ + \nu_e$$

<u>p-p process</u>

$${}^{12}C + p \longrightarrow {}^{13}N + \gamma$$
$${}^{13}N \longrightarrow {}^{13}C + e^+ + \nu_e$$
$${}^{13}C + p \longrightarrow {}^{14}N + \gamma$$
$${}^{14}N + p \longrightarrow {}^{15}O + \gamma$$
$${}^{15}O \longrightarrow {}^{15}N + e^+ + \nu_e$$
$${}^{15}N + p \longrightarrow {}^{12}C + \gamma$$

<u>CNO cycle</u>

Figure 1.1: Primary neutrino producing reactions in the Sun.

9

These reactions are categorized into two cycles: the p-p and the CNO cycles. Both cycles involve the fusion of four protons into an α-particle and the release of 26.7 MeV. The p-p process however occurs 1000 times more frequently due to the rate limiting $^{14}N(p, \gamma)^{15}O$ reaction in the CNO cycle [11]. As a result, the p-p process is responsible for generating 98% of the total energy produced by stellar fusion. While the CNO cycle generates only a small fraction of the total energy, it remains important to neutrino astrophysics because of the higher energies of the neutrinos emitted by this cycle (in comparison to the neutrinos from the p-p process).

Calculation of the solar neutrino spectrum from these reactions requires the coupling of reaction cross-sections and elemental abundances at solar temperatures. At these temperatures, the thermal energy of a proton is only a few hundredths of an MeV while the Coulomb barrier for two protons is on the order of a few MeV. Under these conditions, reaction rates are extremely slow; the mean lifetime for two protons to be fused together is 10 billion years [12]. It is because of these extremely low energies that it is difficult to determine solar reaction cross-sections through laboratory-based experiments. Reaction cross-sections for solar temperatures are often extrapolated down to a few keV from their measured values at a few hundred keV. Much effort has been spent on determining these quantities, and it is in general believed that the solar neutrino problem can not be explained via uncertainties associated with the nuclear physics behind solar models.

Figure 1.2 shows the predicted solar neutrino energy spectrum calculated by Bahcall and Pinsonneault [13,14]. Many models exist [13, 14, 15, 16, 17, 18, 19, 20]; the main differences between them are due primarily to the choice of input parameters. While the predicted neutrino fluxes vary slightly from model to model, the underlying physics remains nearly identical. For this reason, these models are referred to collectively as Standard Solar Models (SSM).
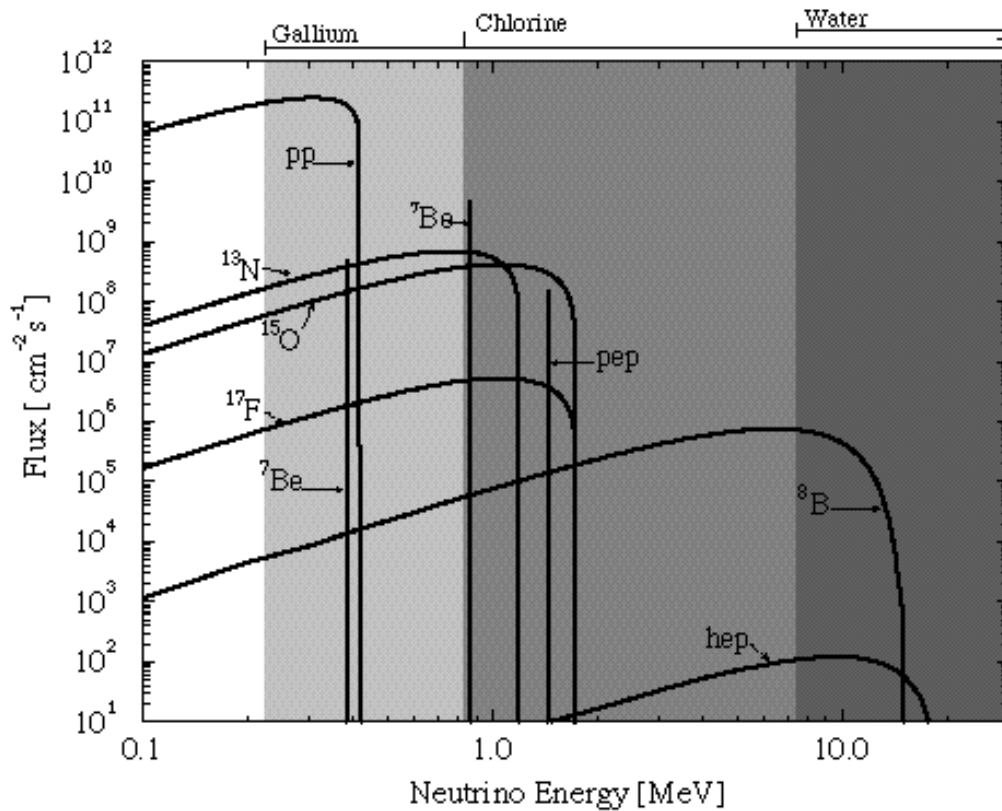
Figure 1.2: Predicted solar neutrino energy spectrum [13,14]. Continuous lines are in units of $cm^{-2}s^{-1}MeV^{-1}$, discreet lines are in units of $cm^{-2}s^{-1}$. The thresholds for various types of solar neutrino detectors (see Section 1.4) is shown at the top of the figure.

11

1.2.2 Solar Model Verification

Verification of these solar models is most often accomplished through comparison of predicted and observed solar properties. The speed of sound at various fractions of a solar radius and the depth of the convective zone are both well measured quantities [21, 22]. The solar speed of sound (c) is a particularly sensitive diagnostic for the prediction of neutrino fluxes. The solar interior is essentially a fully ionized perfect gas, with speed of sound, c $(T/\mu)^{1/2}$ where T is the temperature and μ is the mean molecular mass. The Bahcall – Pinsonneault 1998 solar model (BP 98) predicts a speed of sound which agrees with measured values to better than 0.2% as shown in Figure 1.3.
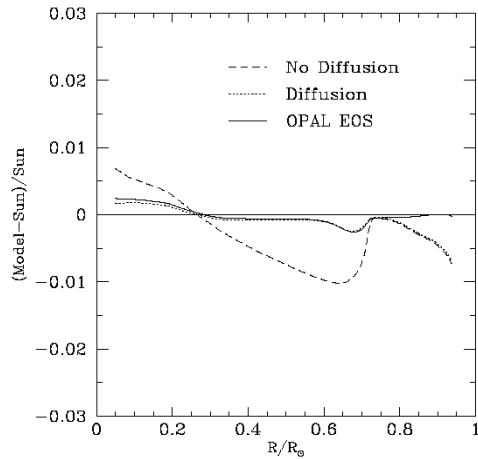
Figure 1.3: Comparison of the fractional difference of the calculated and measured speed of sound in the Sun for three solar models. The solid line represents a solar model with the latest improvements in the solar equation of state and opacities. The heavy dashed lines represent a model with helium and heavy element diffusion, and the dotted line is a model in which diffusion is ignored [23].

This is particularly important to solar neutrinos as the flux is proportional to T^n with $n \sim -1.1$ for p-p neutrinos and ~ 24 for ^{8}B neutrinos. Assuming that the ratio T/μ is accurate to the 0.2% level, it is highly unlikely that the predicted solar temperature T and the mean molecular mass μ are inaccurate by offsetting amounts such that their ratio is consistent with observed values.

1.3 Possible Solutions to the Solar Neutrino Problem

There are two general classes of proposed solutions to the SNP; astrophysical and new particle physics. In the following sections each of these possible solutions are considered.

1.3.1 Astrophysical Solutions

Astrophysical solutions to the SNP tend to revolve around perturbations to the SSM which alter the predicted neutrino flux in a manner so as to be consistent with observed fluxes [24]. These solutions rely on modifying the temperature profile of the solar core, or on non-uniform mixing of material at small radii in the sun. Both of these proposals result in a depression of the predicted solar neutrino flux.

These solutions have been suggested due to recent calculations of the temperature dependence of specific branches of the solar neutrino energy spectrum. Initially it was believed that a slightly decreased core temperature ($T_c \sim 0.96 T_{ssm}$) could explain the deficit of observed ^{8}B neutrinos. There is however

13

an additionally observed suppression of the flux of ^{7}Be neutrinos in relation to observed ^{8}B neutrinos ((^{7}Be)∕ (^{8}B)), requiring an increased core temperature (T$_c$ > T$_{ssm}$). This apparent contradiction tends to indicate that modifying the solar core temperature profile is not a viable solution to the SNP.

Another proposed astrophysical solution to the SNP involves a phenomenologically derived scenario in which ^{3}He "fingers" extend inward to small solar radii [24]. This mixing initiates out-of-equilibrium burning of ^{3}He in the solar core, resulting in a predicted decreased flux of ^{8}B neutrinos as well as a decreased (^{7}Be)∕ (^{8}B). Such mixing alters the mean molecular mass profile of the solar core however, and hence the speed of sound in the core. SSM predicted sound speeds agree with measured values to better than 0.2% as can be seen in Figure 1.3. Comparison of the sound speeds from the mixing model with the helioseismologically-obtained values indicates an 8% difference [23]. This large discrepancy tends to rule-out deep mixing models.

Most recently, there have been several model independent studies [25,26] based on the current experimental data which now tend to exclude the possibility of astrophysical solutions to the SNP entirely. While the proposed astrophysical solutions appear inadequate, additional work is required to reduce the uncertainties associated with solar models.

1.3.2 Particle Physics Solutions

One of the most theoretically investigated of the proposed solutions to the SNP involves neutrinos exhibiting properties beyond the Standard Model of particle

physics. In the minimal Standard Model, neutrinos are generally treated as massless for simplicity. If as an extension of the Standard Model, neutrinos are described by a non-zero mass, then there exists a probability for the neutrinos to change flavor or "oscillate." The mathematical description of oscillations stems from the definition of the neutrino as a superposition of mass eigenstates. In this description, each flavor of neutrino is actually a linear combination of the individual mass states. The process of oscillating from one flavor state to another is therefore described by a quantum mechanical probability.

Applying this to the SNP, if the electron neutrinos which are created by the stellar fusion process oscillate into another flavor, they may not be detected[4]. Oscillation in the absence of external influences or "vacuum oscillations" are described below.

Define the neutrino flavor eigenstates ($_l$) as a superposition of n mass eigenstates ($_m$) as shown in Equation 1.9. At time t=0 and position x the neutrino is described in Equation 1.10 by a wavefunction ($(x,0)$) of the momentum operator (p).

$$_l = \sum_{m=1}^{n} U_{lm} \ _m \tag{1.9}$$

$$(x,0) = \sum_m U_{lm} \ _m e^{ip \ x} \tag{1.10}$$

Considering just the two flavor case, U_{lm} is a unitary matrix describing rotation in two dimensions (Equation 1.11).

---

[4] Current solar neutrino detectors are primarily sensitive only to $_e$ neutrinos. See Section 1.4 for details.

$$U_{lm} = \begin{matrix} \cos\theta_v & \sin\theta_v \\ -\sin\theta_v & \cos\theta_v \end{matrix} \qquad (1.11)$$

Since the wavefunction describing the neutrino is an eigenfunction of energy, the time dependence of the wavefunction can be described by Equation 1.12.

$$\psi(x,t) = \psi(x,0)\,e^{-iEt} \qquad (1.12)$$

For relativistic neutrinos (v ~ c), the time t can be replaced with the distance x traveled by the neutrino. The probability of having an l l' transition (flavor oscillation) is the inner product of the wavefunction in Equation 1.12 ($P(\nu_l \to \nu_{l'}) = \psi^*\psi$), and is given by Equation 1.13.

$$P(\nu_l \to \nu_{l'}) = \sin^2 2\theta \, \sin^2 \frac{x}{L_{mm'}} \qquad (1.13)$$

$L_{mm'} = \frac{4\pi p}{\Delta m^2}$ is called the oscillation length, and defines the scale on which a flavor oscillation can be observed. The magnitude of the oscillation probability depends on the neutrino mass difference (Δm^2), as well as $\sin^2 2\theta$. This mixing angle is assumed to be small by analogy to known quark mixing parameters, and therefore the vacuum oscillation effect is likely to be small. A viable vacuum oscillation solution for such a small mixing angle exists, however, but requires very fine-tuning of the mass differences, Δm^2, and a remarkable coincidence in that the oscillation length be comparable to the Earth-Sun distance. Recently however, Mikheyev and Smirnov developed a mechanism based on the work of Wolfenstein in which neutrino oscillations are enhanced by passage through matter [27]. This is known as the MSW effect.

In the MSW scenario, the probability of having a flavor transition is increased by the passage of neutrinos through an electron density gradient. The neutrino is defined in Equation 1.14 as a superposition of two flavor eigenstates with time dependent coefficients.

$$| \rangle_t = c_e(t)| _e\rangle_t + c_\mu(t)| _\mu\rangle_t \qquad (1.14)$$

The time evolution of the system is described in Equation 1.15.

$$i\frac{d}{dt}\begin{matrix} c_e(t) \\ c_\mu(t) \end{matrix} = M \begin{matrix} c_e(t) \\ c_\mu(t) \end{matrix} \qquad (1.15)$$

In the case of two flavor mixing $M = \begin{matrix} + \\ - \end{matrix}\left| \frac{m^2}{2E} \right| \begin{matrix} -\cos2 _v & \sin2 _v \\ \sin2 _v & \cos2 _v \end{matrix}$. Assume a

perturbation to the mass matrix of the form $M = M_0 + M_{matter}$, where $M_{matter} = \sqrt{2}G_f n_e$. In this perturbation, G_f is the Fermi constant, and n_e is the electron number density. This contribution, shown in Figure 1.3, is the exchange of a W⁻ boson between a $_e$ and an electron. It is this additional interaction available to $_e$ neutrinos, and not $_\mu$ or $_t$, that increases the oscillation probability.
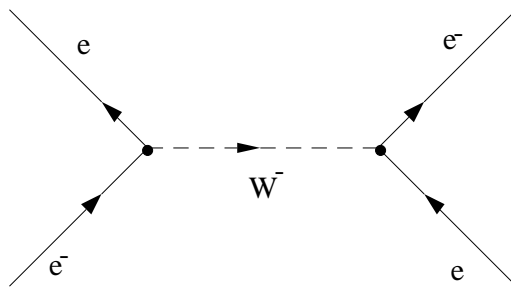
Figure 1.4: Feynman diagram of $_e$ – electron scattering. Note that time is on the vertical axis.

The system is now described in Equation 1.16 by an effective mass mixing angle θ_m.

$$i\frac{d}{dt}\begin{array}{c}c_e(t)\\c_\mu(t)\end{array} = \begin{array}{c}+\\-\end{array}\left|\frac{\Delta m^2}{2E}\right|\begin{array}{cc}-\cos2\theta_m & \sin2\theta_m\\\sin2\theta_m & \cos2\theta_m\end{array}\begin{array}{c}c_e(t)\\c_\mu(t)\end{array} \qquad (1.16)$$

Diagonalizing this matrix and solving for the eigenvalues yields a relation between the effective mass mixing angle θ_m, and the vacuum mixing angle θ_v. This relation is shown in Equation 1.17.

$$\tan2\theta_m = \frac{\tan2\theta_v}{1 \pm \frac{L_v}{L_e}\sec2\theta_v} \qquad (1.17)$$

Where $L_e = \frac{hc}{\sqrt{2}G_f n_e}$ and L_v is the vacuum oscillation length. There is a resonance when $\frac{L_v}{L_e} = \cos2\theta_v$. This maximizes the flavor transition probability as neutrinos pass through a "critical" electron density.
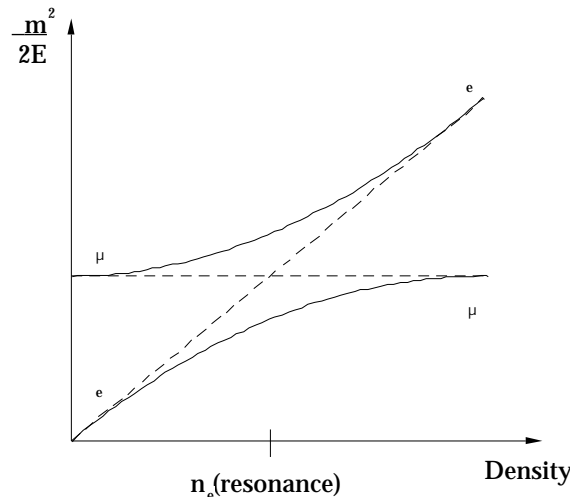
Figure 1.5 MSW level crossing diagram. Dashed lines are the diagonal matrix elements for the two flavor eigenstates from Equation 1.16. The solid lines are the particle trajectories for the heavy and light mass eigenstates.

18

In Figure 1.5, an electron neutrino traveling through matter from a region of higher electron density to a region of lower electron density (from right to left in the figure) has an enhanced probability of being converted into a muon flavor neutrino (for this two-flavor example) at the resonant condition where the critical density is given by Equation 1.18.

$$n_e \text{ (resonance)} = \frac{m^2 \cos 2\theta_v}{2\sqrt{2}G_f E} \qquad (1.18)$$

This solution is only slightly dependent on mixing-angle, and provides a simple mechanism by which neutrino oscillation can be enhanced. An electron flavor neutrino produced in the solar core will travel through regions of lower density as the neutrino leaves the Sun. The MSW Effect then predicts that there is a probability of the neutrino emerging as a flavor other than electron-type.

Section 1.4 Solar Neutrino Detectors

In order to look for neutrino oscillations, experiments must be sensitive to all flavors of neutrinos, or must be capable of inferring neutrino oscillations through careful understanding of the observed solar neutrino energy spectrum. In the following sections, the current status of solar neutrino experiments is described. These experiments have provided solar neutrino data over the majority of the solar neutrino energy spectrum. It is this combined information which has provided much needed insight into the SNP.

Since the initial results of the Homestake experiment were presented in 1968, several new solar neutrino observatories have come on-line. These experiments can be grouped into three categories based on neutrino target: chlorine detectors, water Čerenkov detectors, and gallium detectors. The following sections describe these detectors and their results.

1.4.1 The Chlorine Detector

The Homestake experiment consists of 615 metric tons (100,000 gallons) of the dry-cleaning solution perchloroethylene: C_2Cl_4. It has a threshold of 0.86 MeV, and is sensitive to neutrinos via the reaction shown in Equation 1.19.

$$\nu_e + {}^{37}Cl \rightarrow e^- + {}^{37}Ar \qquad (1.19)$$

The liquid target is contained in a steel tank 4,850 feet underground (4900 meter water equivalent (m.w.e.) of overburden) in the Homestake Gold Mine in Lead, South Dakota. Helium gas is bubbled through the target solution, agitating the mixture and releasing the ${}^{37}Ar$ atoms. The He - Ar gas is circulated through a liquid-nitrogen-cooled charcoal filter that traps the ${}^{37}Ar$ atoms. These atoms are then placed in a proportional counter which observes the 2.8 keV x-rays emitted after the electron capture decays of ${}^{37}Ar$. The number of extracted atoms is determined by counting the decays of the 35 day ${}^{37}Ar$ half-life. This procedure has been calibrated by introducing known amounts of ${}^{36}Ar$ and ${}^{38}Ar$ into the system, and has an extraction efficiency of 95%.

The Homestake experiment has essentially 25 years of solar neutrino data. During that time, statistical and systematic errors have been reduced, but the

overall capture rate has not changed significantly: 2.55 ± 0.17(stat.)± 0.18(syst.)

SNU [28]. The results continue to be about one-third of the expected $9.3^{+1.2}_{-1.4}$ SNU

signal [29].

1.4.2 Water Čerenkov Detectors

Water Čerenkov detectors observe the light emitted by the interaction of a

neutrino in a water target. This interaction, shown in Equation 1.20, gives rise to

an energetic electron which Čerenkov radiates.

$$\nu_x + e^- \rightarrow \nu_x + e^- \qquad\qquad (1.20)$$

Water Čerenkov detectors are sensitive to all three neutrino flavors ($\nu_x = \nu_e$ or ν_μ

or ν_τ) through this scattering reaction which is mediated by Z^0 boson exchange.

The scattering cross-section for ν_e is about 6 times greater than for ν_μ or ν_τ

however as a result of the additional scattering channel through the exchange of

the charged W$^-$ boson.

There is currently one operational solar neutrino observatory of this

variety – Super Kamiokande (SuperK) in Japan. The detector is located 1 km

underground (2700 m.w.e) in the Kamioka mine. It is the fourth revision of what

was originally a nucleon decay experiment (Kamioka Nucleon Decay

Experiment). The original Kamioka neutrino detector (Kamiokande II and

Kamiokande III) consisted of 3,000 tons of water surrounded in cylindrical

geometry by 948 photomultiplier tubes with 50 cm diameters. In its current

configuration, SuperK consists of 50,000 tons of water surrounded by 11,200 photomultiplier tubes also with 50 cm diameters.

In addition to monitoring the flux of neutrinos, SuperK has the ability to verify that the Sun is the source of the neutrinos by looking at the correlation between the direction of the recoil electron and the Sun. Owing to its extremely large size, SuperK has an event rate (~13.5 events/day > 7 MeV) which yields enough statistics to make it moderately sensitive to the MSW Effect by looking for distortions in the neutrino energy spectrum. Additionally, SuperK is capable of looking for neutrino oscillations in what is called the day-night effect. This is an enhanced probability of a neutrino oscillation caused by travelling through the Earth (higher electron density) prior to detection.

In its most recent published results [30], the SuperK collaboration cite a 7 MeV analysis threshold, and an observed flux of $2.51\,^{+0.14}_{-0.14}$ (stat.) $^{+0.18}_{-0.18}$ (syst.) $\times 10^6$ $_e$ cm^{-2}s^{-1}. This result is consistent with the published combined results for Kamiokande II and III of $2.95\,^{+0.22}_{-0.21}$ (stat.) $^{+0.36}_{-0.36}$ (syst.) $\times 10^6$ $_e$ cm^{-2}s^{-}1 [31]. Both results are about a third of the predicted $6.6\,^{+0.14}_{-0.17}\times10^6$ $_e$ cm^{-2}s^{-1} [29].

1.4.3 Gallium Detectors

There have been two solar neutrino detectors utilizing a gallium target to observe the reaction in Equation 1.21.

$$_e + {}^{71}\text{Ga} \quad e^- + {}^{71}\text{Ge} \tag{1.21}$$

These experiments, SAGE (Russian (Soviet) American Gallium Experiment) and GALLEX (GALLium EXperiment), have been of particular importance to the SNP since the threshold for their reaction is 0.23 MeV, making them sensitive to all the neutrino producing reactions in the Sun. Additionally, both experiments have used powerful neutrino sources to accurately determine their detection efficiencies.

The SAGE experiment is located in the Caucasus Mountains of Russia with a 4700 m.w.e. overburden. The detector consists of 60 metric tons of liquid gallium contained in eight reactor vessels. GALLEX is based in the Gran Sasso region of Italy, and consists of 30.3 metric tons of gallium in an acidic solution. Both experiments employ radiochemical extraction techniques to determine the number of ^{71}Ge atoms present in their detector volumes. The extraction techniques used by the two gallium experiments are systematically different however. The SAGE experiment has a typical extraction efficiency of 80%, while GALLEX reports an average extraction efficiency of 99%.

The predicted neutrino capture rate for both SAGE and GALLEX is 137^{+8}_{-7} SNU [29], while the observed rates are 74^{+13}_{-12} (stat.) $^{+5}_{-7}$ (syst.) SNU [32] and $77.1^{+8.5}_{-8.5}$ (stat.) $^{+4.4}_{-5.4}$ (syst) SNU [33] respectively. Both experiments have calibrated their detectors using ^{51}Cr sources (~1.5 MCi for GALLEX, 0.5 MCi for SAGE). The neutrino spectrum from this source is very similar to the solar ^{7}Be neutrino lines, providing a useful check on the functionality of the detectors. These calibrations

yielded results expressed as a ratio of observed to predicted events of $0.93\,^{+0.15}_{-0.17}$

for SAGE [34] and $0.97\,^{+0.11}_{-0.11}$ for GALLEX [35].

1.4.4 The Future of Solar Neutrino Experiments

Figure 1.6 summarizes the current results of solar neutrino experiments and their predicted rates. All classes of experiments observe only a fraction of the predicted rates. There is an additional problem, however, in that the observed deficit is not constant over the solar neutrino spectrum, seeming to indicate an energy dependence on the observed fluxes.
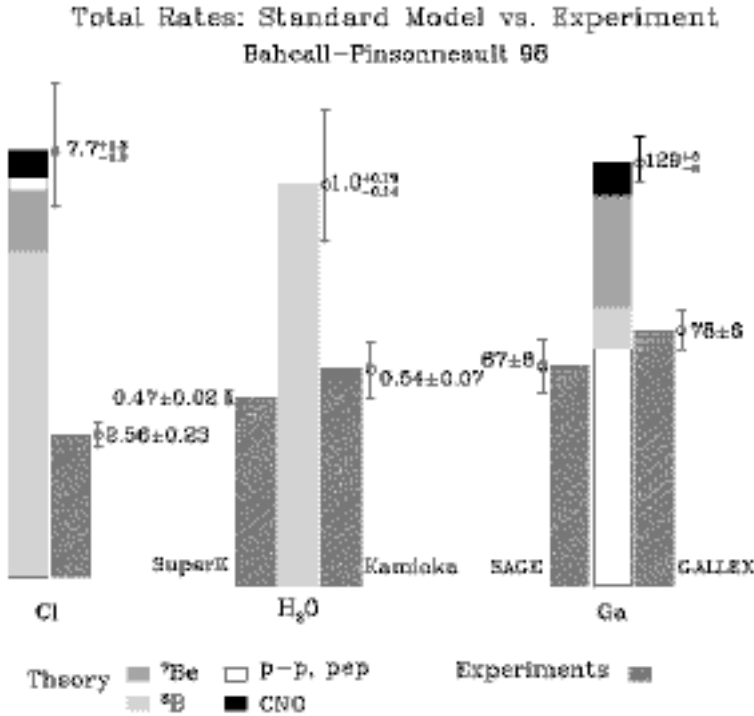
Figure 1.6: Comparison of the total predicted and observed rates for the four solar neutrino experiments [36].

24

There are clearly unresolved problems with respect to our understanding of the role solar neutrinos play in the stellar fusion process. SuperK is currently the only operational solar neutrino experiment sensitive to testing the favored MSW solution to the SNP. Another solar neutrino experiment is nearing completion, however, that is extremely sensitive to neutrino oscillations due to its use of D_2O as a target. This experiment, The Sudbury Neutrino Observatory, is currently poised to begin taking data, and should provide the most conclusive evidence for neutrino oscillations. Chapter 2 describes this experiment.

Chapter 2

2.1 Introduction to the Sudbury Neutrino Observatory

The possibility of using the neutral current disintegration of deuterium to measure the total solar neutrino flux was suggested by Herb Chen in 1985 [37]. A comparison of this flux to a measured ν_e charged current neutrino flux would provide model-independent confirmation of oscillations. In 1984, the SNO collaboration was formed when it became apparent that 1000 metric tons of D_2O could be obtained on loan from the Canadian government. Additionally, a deep mine was located which provided a suitably shielded site for construction of a low-background detector. Initial feasibility studies resulted in R&D funding, and exploratory mining work at the proposed experimental site. In 1988 the "Sudbury Neutrino Observatory Proposal" was presented to an International Scientific and Review Committee which strongly recommended that the experiment be funded.

By June 1992, the access drift and the cavity to house the detector had been excavated. Cavity preparation, steelwork assembly, and commissioning of the cleanroom took the next 3 years. In mid-1995 work had begun on assembling the acrylic vessel, and construction was completed early 1998. Currently, the SNO detector is being filled with the D_2O, and undergoing calibration tests.

The cavity housing the detector is located in an active nickel mine owned by the International Nickel Company (INCO), in the town of Walden, near

Sudbury Ontario. The cavity is at a depth of 2070 m (6800 feet) in norite rock, which provides a 5900 meter water equivalent (mwe) overburden. The cavity is barrel-shaped with a height of 30 m, and a maximum diameter of 21 m.

Figure 2.1 shows the major components of SNO. The detector consists of a 12-m-diameter acrylic vessel which contains 1000 metric tons of D_2O. The vessel is 5.5 cm thick, and was assembled from 122 thermoformed acrylic panels[1], which were sized to facilitate transport underground. The equator of the vessel consists of alternating 5.5 cm and 11.4-cm-thick panels. These 10 thicker equatorial panels were machined with U-shaped grooves through which Vectran[2] ropes are threaded to suspend the entire vessel.

Surrounding the vessel are 9456 Hamamatsu model R1408 photomultiplier tubes (PMTs) with 20-cm photocathode diameters. The PMT glass envelopes were constructed of borosilicate glass by Schott Glaswerke. This material was developed for SNO to provide low radioactivity glass capable of withstanding long term submersion in ultra-pure water. The PMTs are fitted with light concentrators to increase the total photocathode coverage to 64%, and are mounted on an 18-m-diameter geodesic support structure.

The entire detector assembly is immersed in 7000 metric tons of ultra-pure water to provide shielding from naturally occurring radioactivity in the cavity walls. The water is expected to be maintained at 7° C to keep biological cell counts to a few cells per ml. The average resistivity of the water is approximately 3 M . Additional shielding is provided by low radioactive cement lining the

---

[1] The acrylic panels were made by Reynolds Polymer Technologies (RPT). Construction of the acrylic vessel was supervised by RPT technicians.

cavity walls, and a special Urylon coating which limits radon emanation into the cavity.

The electronics to read-out the PMTs was designed to have sub-nanosecond timing resolution and virtually no deadtime. The system is capable of operating at a sustained rate of 1 kHz, and can handle bursts of up to 1 MHz. Individual event timing is accomplished with a 50MHz clock, and SNO is synchronized to Universal Time via a 10MHz oscillator which is updated by a Global Positioning System (GPS) clock.

The electronics system essentially operates as 10,000 independent asynchronous channels. Photon interactions in a PMT result in the generation of a current pulse. A 10,000 input analog sum compares the combined current pulses of all PMT channels to a programmable threshold. A summed pulse greater than threshold results in an energy trigger of the SNO detector. The system is additionally capable of triggering based on the number of PMTs which fired in a given time interval.

The Data Acquisition System (DAQ) for SNO is written in the object-oriented C++ programming language. It controls the general operating parameters of the detector and the readout of the 10,000 independent channels. The DAQ program runs on a Macintosh PPC-based platform, and interfaces with the front-end electronics through a VME-style architecture. PMT event data is shipped through an embedded CPU (eCPU) to a SUN Ultra Sparc computer where individual event information such as collected charge and PMT tube

---

[2] Vectran is the brand name of a high-strength multifilament liquid-crystal polyester (Hoechst Vectran Co.)

number are combined with event trigger and timing information before being written to tape.
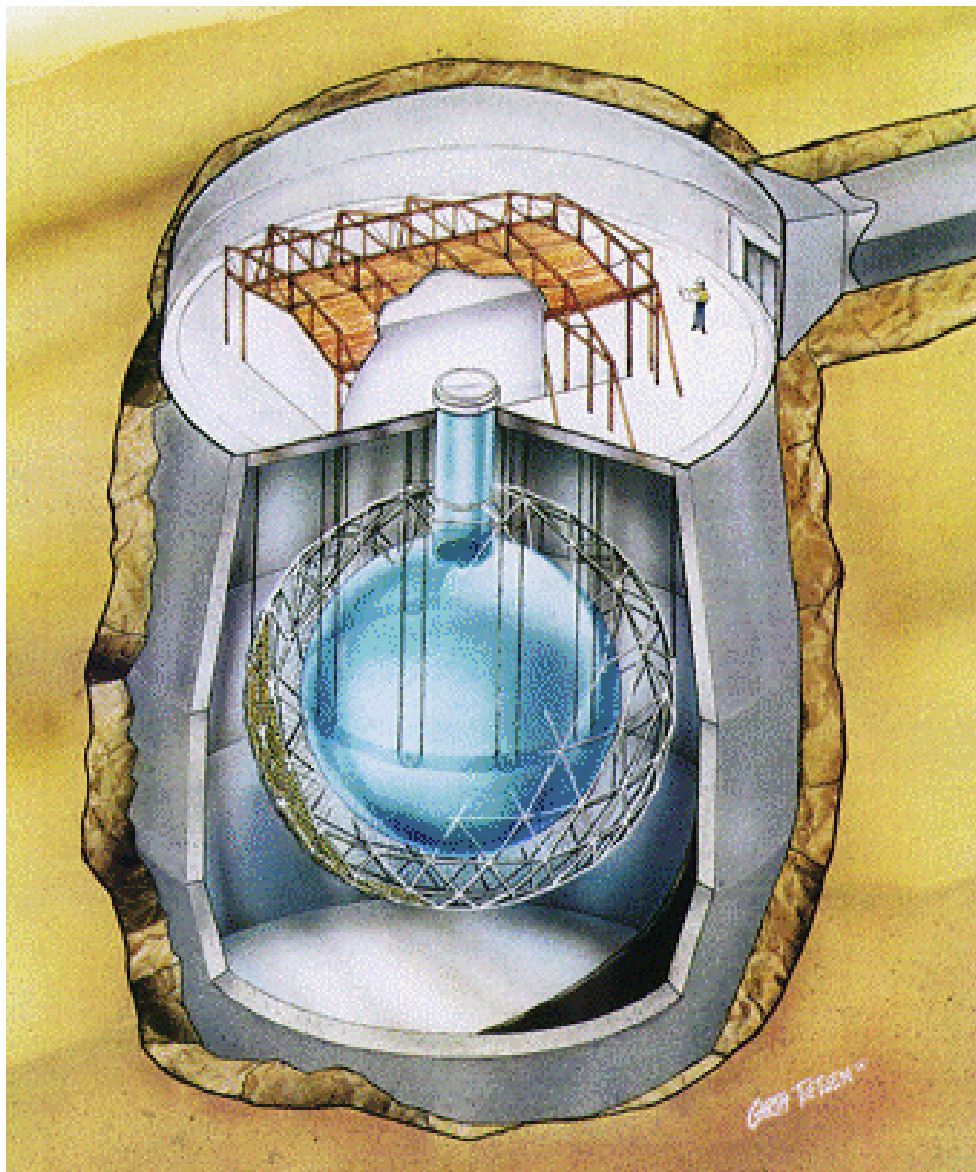
Figure 2.1: Artist's conception of the Sudbury Neutrino Observatory.

2.2 Neutrino Interactions in SNO

There are three primary neutrino interactions in heavy water: the charged current (CC), neutral current (NC), and electron scattering (ES) reactions. These reactions are listed below along with their anticipated event rates in SNO. These rates are the integrated flux from Figure 1.2 [13,14] multiplied by the interaction cross-sections assuming a 5 MeV detection threshold. Figure 2.2 shows the Feynman diagrams of the primary SNO reactions.
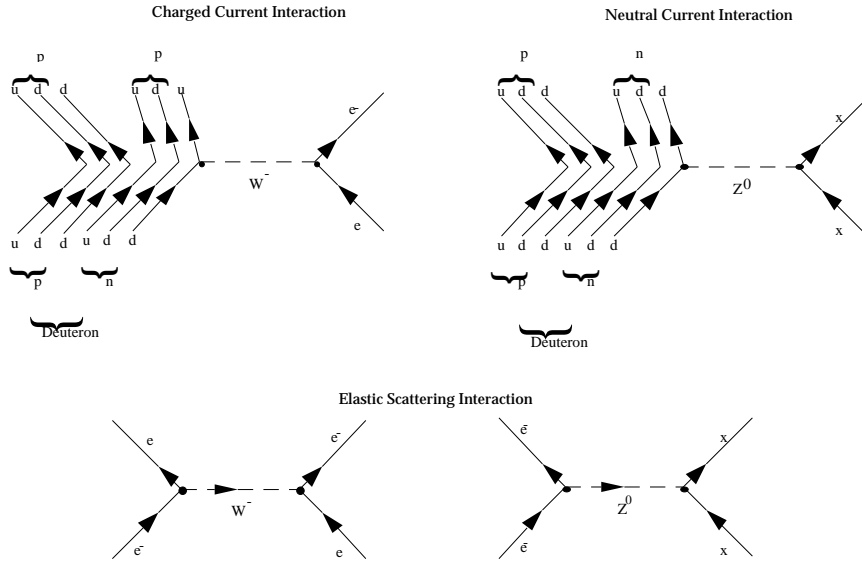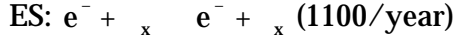
Figure 2.2: Feynman diagrams of primary SNO reactions.
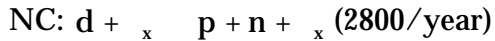
CC: $d + \nu_e \rightarrow p + p + e^-$ (9750/year)

In this reaction, the recoil electron is relativistic, and can be detected with the PMT array via its Čerenkov light signature. Electrons from this reaction have energies of approximately $E_\nu - 1.44\text{MeV}$ [38], thus enabling the determination of

the electron neutrino energy spectrum. Additionally, these electrons will have an angular distribution of $W(\theta_e) = 1 - 1/3\cos(\theta_e)$ [39] where θ_e is the angle between the incident neutrino and the recoiling electron. This distribution therefore contains information as to the location of the source of the interacting neutrino.

ES: $e^- + \nu_x \rightarrow e^- + \nu_x$ (1100/year)

The elastic scattering interaction is in priciple flavor independent. However, it is about 6 times more likely to occur for an electron neutrino due to the possible exchange of a W^- boson in addition to the Z^0 boson exchange available to all neutrino flavors. The recoil electron from this reaction is also detected via its Čerenkov signature in the PMT array. The separation of CC and ES events may be possible by examining the angular response of the PMTs on an event by event basis. The recoil electron is extremely forward biased, resulting in 90% of all electrons with energy greater than 5MeV travelling in a cone of half-angle 14.6° [39].

NC: $d + \nu_x \rightarrow p + n + \nu_x$ (2800/year)

This reaction involves the disintegration of the deuteron, and has a kinematic threshold of 2.2 MeV. Detecting the free neutrons liberated by the NC reaction enables SNO to determine the total neutrino flux since the reaction cross section is completely independent of neutrino flavor. This NC reaction also means that SNO is sensitive to neutrino oscillations by comparing the CC flux to the NC flux. A ν_e to ν_x flux ratio of less than one would indicate neutrino oscillations.

Due to the critical nature of the NC measurement, the SNO collaboration is developing two systematically independent techniques to detect these neutrons. In a pure D_2O run, 37% of the free neutrons would be captured by the deuterium [40], with each capture resulting in the emission of a 6.25 MeV gamma-ray. Detection of this photopeak with the PMT array would be difficult, however, assuming a 5 MeV analysis threshold. Both the neutron capture efficiency and the photopeak energy can be increased through the addition of a neutron absorber such as MgCl. In this method, neutron capture on ^{35}Cl produces up to 3 gammas with a total energy of 8.6 MeV as shown in Equation 2.1.

$$n + {}^{35}Cl \rightarrow {}^{36}Cl + \gamma's \qquad (2.1)$$

The neutron capture efficiency is increased to over 80%, and the total neutron detection efficiency becomes 50%. These events, however, may be virtually indistinguishable from CC events, and obtaining the NC flux using this method will require a spectral subtraction or a statistical separation.

An independent NC detection method is being developed by the University of Washington, Los Alamos National Laboratory, Lawrence Berkeley National Laboratory, and the University of Guelph. This method involves the deployment of an array of discrete ^3He proportional counters which detect the free neutron through the $n(^3He,p)^3H$ reaction. This method is described in detail in Chapter 3, and is the basis of this thesis work.

2.3 Calibration of SNO

Understanding the response of the SNO detector is crucial to extracting the neutrino fluxes and energies. This requires energy and optical calibration as well as a determination of neutron detection efficiency for SNO. Described below is the system of calibration sources which have been developed to ascertain the SNO detector's response to both optical and neutron events. Calibration sources are deployed in SNO with the "source manipulator." This is a system of ropes and pulleys affixed to the inside of the acrylic vessel which allows for placement of the sources in three dimensions.

Calibration of the PMT array requires an understanding of the mechanism by which a relativistic recoil electron generates the Čerenkov light, how that light is affected by passing through the D_2O and the acrylic vessel, and how the individual photomultiplier tubes respond to photon collection. In addition, the response of the electronics must be known in order for analysis routines to accurately reconstruct events in the detector. Finally, the response of the detector must be understood over the entire energy range of solar neutrinos to which SNO is sensitive (5-11 MeV), requiring the development of several calibration sources.

Relativistic charged particles travelling faster than the speed of light in a medium emit photons in a cone described by Equation 2.2 and shown in Figure 2.3. These photons are called Čerenkov radiation.

$$\cos(\ ) = 1/n \qquad\qquad (2.2)$$

The medium is characterized by an index of refraction n, and $\quad$ is the charged particle's speed relative to the speed of light. For the energies of the interaction particles in SNO, this angle is approximately 41°. The emitted photons have a frequency distribution which is essentially flat over the range of sensitivity of the PMTs (300 – 600 nm). In order to determine the attenuation and frequency response of the detector, two optical calibration sources will be used in SNO.

v > c(n)

Light Cone
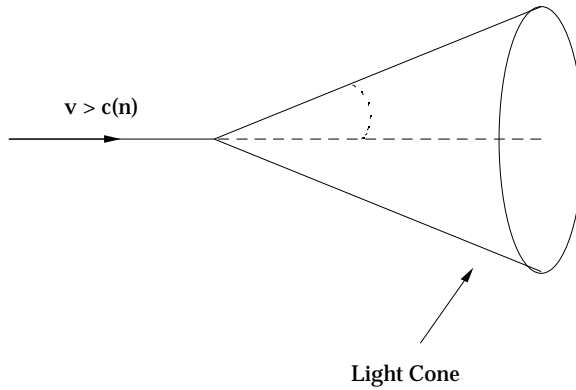
Figure 2.3: Čerenkov light emitted by particle travelling greater than the speed of light in an index of refraction n.

The first source employs a N_2 dye laser to provide four wavelengths between 337 and 386 nm. The laser light is transmitted through an optical fiber to a diffuser ball which can be deployed inside the detector with the source manipulator. This allows the detector's frequency response to be determined as a function of source position.

In order to achieve the sub-nanosecond-timing-resolution goal, a sonoluminesence source was developed. This source emits light pulses with widths less than 100 ps, and a spectral distribution similar to a Plank blackbody of temperature between 10,000° and 25,000° K. The short pulse width allows the

PMT timing response to be measured as a function of source position and intensity. Additionally, the source can be operated at a rate of 25 kHz, and serves to test the detectors response to high event rates.

The energy calibration of the detector will be accomplished using   and sources. These sources emit gamma rays with energies from 1.37 to 19.8 MeV, and beta particles with endpoints from 4.3 to 13.1 MeV. These sources are summarized in Table 2.1. In addition to calibrating the energy response of the detector, these sources provide a means to determine SNO's sensitivity to naturally occurring radioactivity – namely the U and Th decay chains. An understanding of the contribution of these chains to the backgrounds in SNO is very important and is described Section 2.4.

Table 2.1: Calibration sources for SNO.

Reaction	Energy
^{2}H(n,)^{3}H ^{3}He(n,)^{4}He ^{3}H(p,)^{4}He ^{35}Cl(n,)^{36}Cl ^{11}B(p,)^{12}C	E = 6.25 MeV E = 21 MeV E = 20 MeV E = 8.6 MeV E = 11.7, 4.4 MeV
Decay	End Point
^{16}N $\rightarrow$ ^{16}O $+ e^- + \bar{}_e$ ^{8}Li $\rightarrow$ ^{8}Be $+ e^- + \bar{}_e$	Q = 10.4 (29%) or Q = 4.3 (60%) MeV, E = 6.1 MeV Q = 13.1 MeV
Source	Neutron Energy
^{252}Cf	Maxwellian distribution of neutron energies

A ^{252}Cf source will be utilized to determine neutron efficiencies. The source will be encapsulated in an acrylic enclosure containing a plastic scintillator. In the spontaneous fission of ^{252}Cf, 4 neutrons and 20 gammas are emitted. The light produced by the interaction of the gamma-rays with the scintillator will be detected by the PMT array, and will serve as a trigger for the system. The neutron detection efficiencies for either neutral current detection option can therefore be determined by moving the source to various locations in the detector while monitoring triggers and neutron events.

2.4 Backgrounds in SNO

The primary contribution to SNO's backgrounds are - events due to the Th and U decay chains. Figure 2.4 shows the various contributions of these chains to background events in SNO (Appendix 1 contains the U and Th decay chains). Two of the daughters of U and Th are particularly problematic: ^{214}Bi and ^{208}Tl, each of which decay with one gamma-ray with an energy greater than the binding energy of the deuteron. Thus, these nuclei also represent a background to the neutral current detection via photodisintegration of the deuteron yielding a free neutron. For these reasons, limits have been placed on the U and Th content of construction materials. These limits are determined by where the materials are to be used in the detector, with the most stringent limits placed on materials in the D_2O. The D_2O limit is set to keep background neutron events below 10% of the expected annual NC signal, and equates to a limit of 3.7 μg of

Th or 45 µg of U. The U and Th limits for all regions of the detector are summarized in Table 2.2.
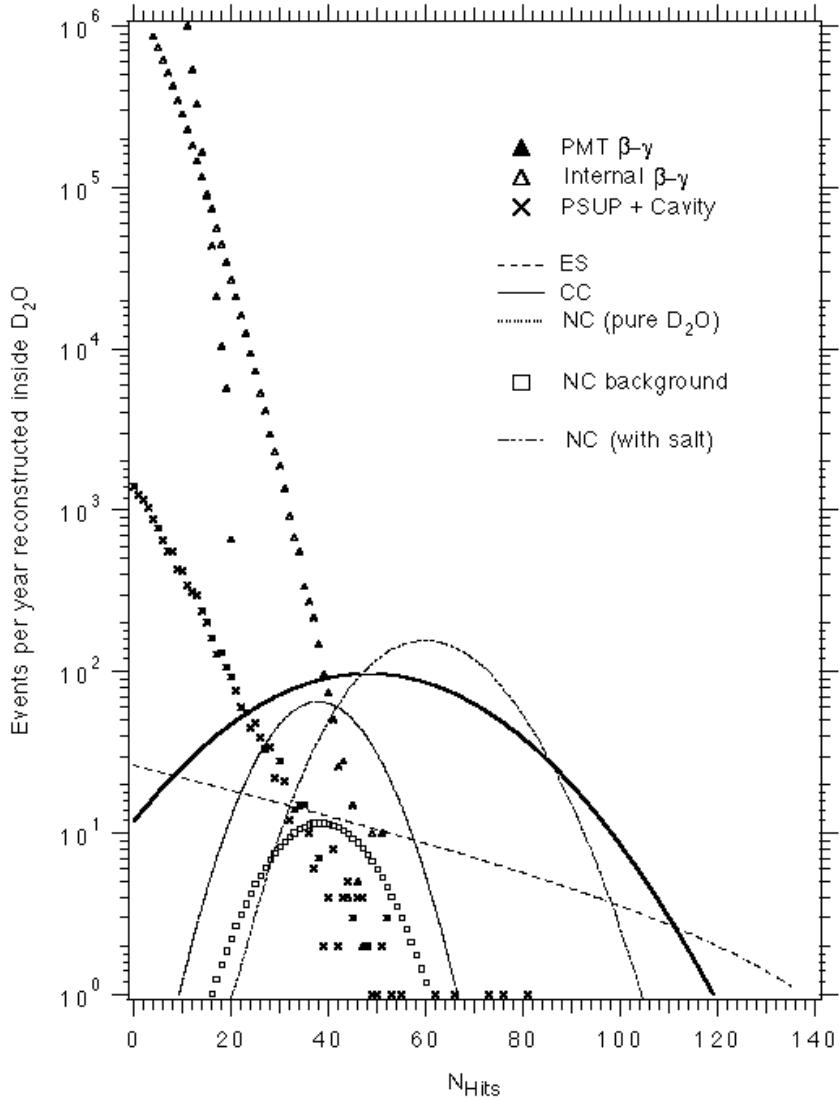
Figure 2.4: Anticipated energy distribution of events in SNO after one year of data. General background events are labeled as PMT β-γ, Internal β-γ, and PSUP+cavity. N_{Hits} refers to the number of PMTs which observed an event, and translates into energy (1 MeV = ~ 8 N_{Hits}) [41].

Table 2.2: Limits on the ^{238}U and ^{232}Th contamination in various parts of the SNO detector . Units are grams of contaminant per gram of material.

Region	^{232}Th	^{238}U
D$_2$O	3.7×10^{-15}	4.5×10^{-14}
H$_2$O	1×10^{-13}	1×10^{-12}
Acrylic	2×10^{-12}	4×10^{-12}

2.5 Physics Potential of SNO

The scientific objectives of SNO are to "measure the flux and energy of electron neutrinos reaching the earth, (and additionally) to measure the total flux of all neutrinos above 2.2 MeV." Through these measurements, SNO will be able to "1) show clearly if neutrino oscillations are occurring, and 2) independently test solar models by determining the production rate of high-energy electron neutrinos in the solar core" [42].

SNO will measure the energy spectrum of neutrinos coming from the ^{8}B reaction to lower energies than any previous experiment. Because of this sensitivity, SNO is well suited for examining the apparent energy dependence of the SNP.

Since SNO is a real-time experiment with excellent time resolution, it will also provide for the means to correlate neutrino flux with other solar observables such as sunspots, solar flares, and interior pressure waves.

SNO is also capable of providing previously-unavailable data in the event of a supernova since it can handle high burst rates with nanosecond timing resolution, is sensitive to all neutrino flavors, and has the ability to correlate the

time of events with other astrophysical detectors. The mechanism by which a star becomes a supernova is generally agreed upon however the dynamics of the event are still not well understood. Observation of the initial flux of neutrinos from a supernova could be used to aid in the modeling of stellar collapse. Additionally, by monitoring the time development of all flavors of neutrinos from a supernova event, SNO is capable of making a direct measurement of a mass difference between flavors.

The most interesting potential of SNO, however, is its ability to test for neutrino oscillations in a model-independent manner. The CC interaction in SNO will provide high-statistics for the flux of ν_e coming from the sun as determined by the angular correlation of the recoil electrons from the CC and ES reactions. The NC reaction then measures the total solar neutrino flux. By comparing the fluxes of CC to NC as a ratio, correlated uncertainties associated with the neutrino cross-sections cancel. A ratio less than 1 would indicate that neutrino oscillations do occur while a ratio of 1 would imply that neutrinos do not oscillate, or that they oscillate into a non-interacting, or "sterile" flavor.

The measurement of the NC signal is a key element of this search, and the use of an array of ^{3}He counters to make this measurement is described in Chapter 3.

Chapter 3

3.1 Neutral Current Detector (NCD) Array

The NCD array utilizes ^{3}He-filled proportional counters to detect the free neutron liberated by the NC interaction through the ^{3}He(n,p)^{3}H reaction. The decision to develop this array was based on a desire to implement a versatile method which provides for an unambiguous NC measurement:

1) NC and CC events are recorded separately and distinguished event by event.

2) Variation in the NC rate due to eccentricity of Earth's orbit would be observable at the 95% confidence level thus confirming the Sun as the source of the NC signal.

3) Time variations in the neutrino flux can be followed in both the CC and NC detection channels simultaneously and independently.

The array design consists of 300 counters with individual lengths of 2, 2.5, or 3 m welded together to form 96 strings for a total active length of 770 m. The strings will be located on a 1-m grid within SNO's acrylic vessel, and have lengths which vary from 4 to 11 meters. Figure 3.1 shows an artist's conception of the deployed array inside the acrylic vessel. Four of the NCD strings are filled with a ^{4}He:CF$_4$ mixture which is not sensitive to neutrons. These strings will be used for *in situ* background measurements. Monte Carlo calculations indicate a 45% neutron detection efficiency for the entire array [43], with only a small impact on

40

the optical properties of the SNO detector (estimated 15% loss of light after NCD

installation [44]).
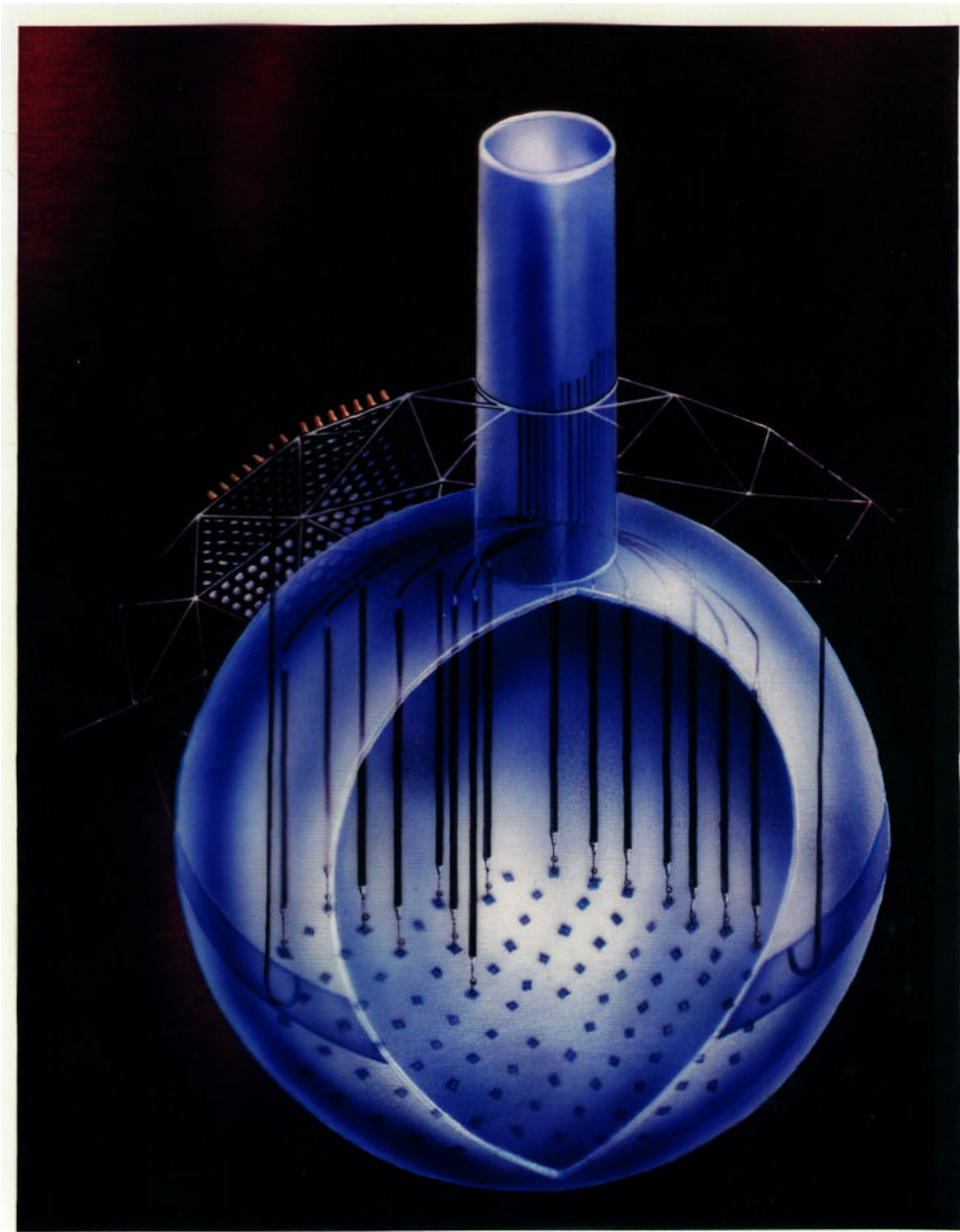
Figure 3.1: Artist's conception of the deployed NCD array. Note: the diameter of
the NCD strings is not to scale – if it were, the strings would not be discernable.

Free neutrons from the photodisintegration of deuterium represent a serious background to the NC measurement in SNO. Radionuclei such as U and Th give rise to such a background, and as a result stringent limits have been placed on the amounts of these isotopes allowed in the SNO construction materials (See Table 2.2). These limits were set so that the U and Th decays would give rise to no more than one neutron per day, or 10% of the expected NC signal. The NCD design goal however is to limit the added photodisintegration background to less than 1-2% percent of the expected NC signal. An additional constraint placed on the NCD construction material is that the array must be capable of sustained remote operation in the acrylic vessel on order of the projected lifetime of SNO (10 years).

These requirements precluded the use of commercially available proportional counters for the NCD array, thereby initiating the design of ultra low-background proportional counters.

3.2 General Proportional Counter Design

Proportional counters have been extensively used in nuclear and particle physics since their introduction in the late 1940's. Material and gas purification advancements have enhanced proportional counter performance, but the fundamental operational characteristics have remained the same. Figure 3.2 shows the basic elements of a proportional counter.
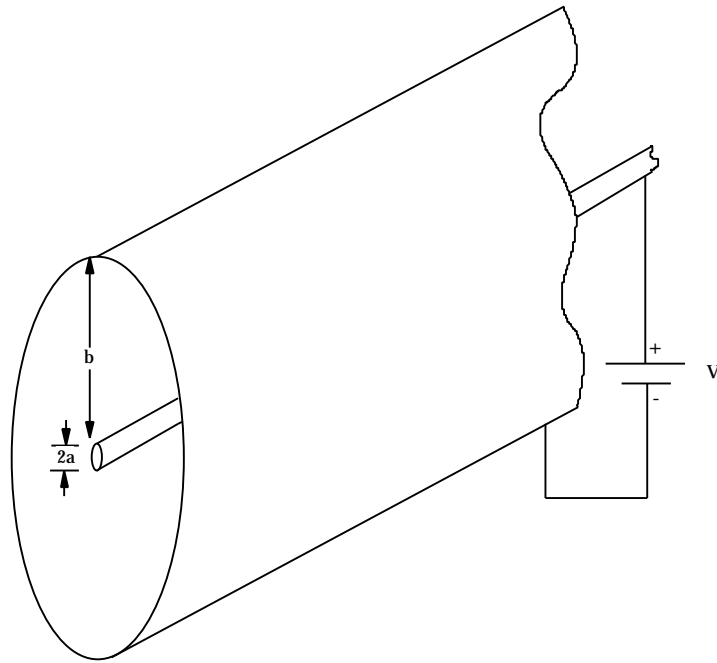
Figure 3.2: Basic elements of a proportional counter.

An energetic charged particle entering the detector ionizes the gas, resulting in the creation of a number of electron-ion pairs. The number of pairs produced is ultimately dependent upon the energy loss of the particle in the gas. Due to the mobility of the electrons, they are easily accelerated by application of a high voltage to the anode of the counter. The electrons can be accelerated to kinetic energies sufficient to produce secondary ionization, resulting in the production of additional electron-ion pairs in numbers which are proportional to the original number of pairs. The ratio of the number of secondary to primary pairs is effectively the gas multiplication factor of the counter for a given set of operating parameters such as voltage and pressure. The movement of the electron-ion pairs in the counter therefore induce an electrical signal on the

anode whose amplitude is dependent on the energy of the original ionizing particle.

Performance characteristics of a proportional counter are typically described by Diethorn parameters [45] which relate the gas multiplication factor (M) of a counter to physical characteristics such as counter dimensions and constants associated with the fill gas:

$$\ln M = \frac{V}{\ln(b/a)} \frac{\ln 2}{\Delta V} \ln \frac{V}{aP\ln(b/a)} - \ln K \tag{3.1}$$

Here V is the operating voltage of the counter, a and b are the counter's anode and cathode radii respectively, ΔV is the potential difference for an electron between ionization events, P is the gas pressure, and K is a gas constant associated with ion multiplication threshold.
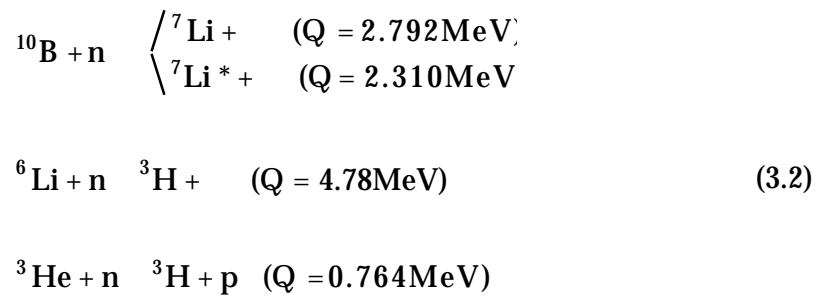
The choice of gas fill for a proportional counter design depends primarily on the ionizing particle of interest. Proportional counters typically are filled with a mixture of two gases. The primary gas is responsible for stopping the ionizing particle in the detector, while the secondary or quenching gas serves to minimize photon-induced events within the counter. In this latter case, an electron accelerating towards the anode may excite a neutral atom to a higher state as opposed to ionizing the atom. This atom may decay back to the ground state via photon emission resulting in either an ionization event in another part of the counter, or the release of a photoelectron from the counter wall. The quenching gas is typically polyatomic which allows for absorption of these photons through rotational or vibrational modes.

44

The operating voltage of a proportional counter is chosen to maximize the energy resolution by balancing the multiplication factor with space charge effects. These effects occur when electron-ion pairs which are created preferentially close to the anode wire shield the anode. This results in a lowering of the effective field as seen by electrons and ions at greater radii. Space charge effects can be reduced by running at lower operating voltages. Gas multiplication, and hence signal amplitude, scale linearly with operating voltage however. Thus an operating voltage which provides a sufficiently large pulse for analysis yet maintains acceptable energy resolution is usually chosen.

In the following section, the specific application of these parameters to the NCD design is discussed.

3.3 NCD Design

In experiments to detect slow neutrons, the three most widely used targets are ^{10}B, ^{6}Li, and ^{3}He. These atoms convert slow neutrons to detectable particles through the reactions shown in Equation 3.2.

$$^{10}B + n \quad \begin{cases} ^{7}Li + & (Q = 2.792 MeV) \\ ^{7}Li* + & (Q = 2.310 MeV) \end{cases}$$

$$^{6}Li + n \quad ^{3}H + \quad (Q = 4.78 MeV) \qquad\qquad (3.2)$$

$$^{3}He + n \quad ^{3}H + p \quad (Q = 0.764 MeV)$$

In all three reactions, the products are charged heavy particles which can be detected via proportional counter or scintillation detector. Of all three targets,

45

^{3}He has the highest thermal neutron absorption cross section at 5280 barns ((^{10}B)=3840 barns, (^{6}Li)=940 barns). Unfortunately, ^{3}He is also the most expensive of the three, costing nearly \$150/STP-l (For comparison, a standard counter gas, P-10 (Ar:CH$_4$), costs \$2/STP-l). Fortunately, however, a supply of ^{3}He gas was available at the time of the original NCD design work.

The choice of the second component of the fill-gas was made by considering of the desired gas gain, electron drift speed, and stopping power of the NCDs. A detailed treatment of these considerations can be found in Reference 46. Tetraflouromethane (CF$_4$) in a fraction of 15% by total pressure was determined to provide the best compromise of these quantities.

Because of the low atomic number of the primary component of the NCD gas mixture, the range of the products for the ^{3}He(n,p)^{3}H reaction is comparable to the counter dimensions. Conservation of momentum implies that the proton and triton (^{3}H) will be emitted back-to-back with 573 and 191-keV of energy respectively. This combined proton + triton track length is about 9 mm in 2.5-atm of ^{3}He:CF$_4$ (85:15) [47] whereas the counter diameter is 50.8 mm. As a result, about 20% of all neutron events will end with either the proton or triton hitting the wall of the counter, and not depositing the full 764-keV of energy in the gas. This is the so-called "wall effect." In an energy histogram, the wall effect creates a continuum from 191 to 764-keV as shown in Figure 3.3.
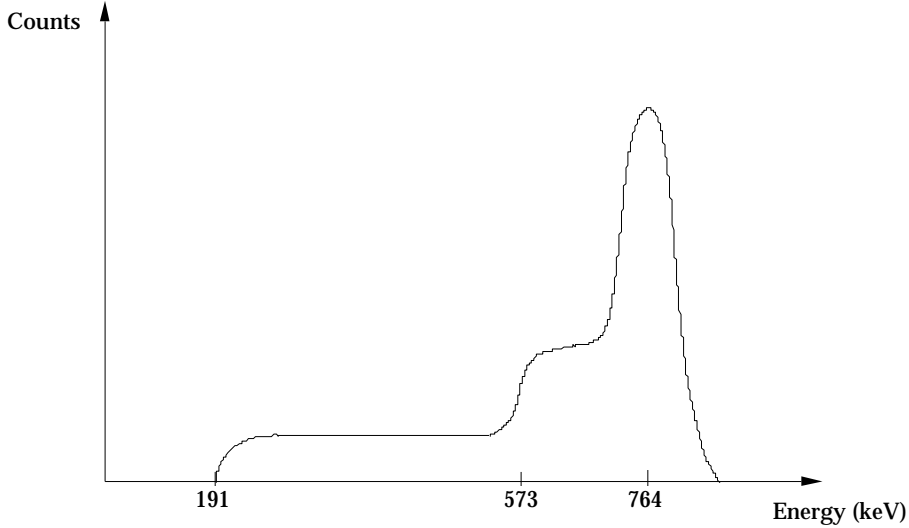
Figure 3.3: The "wall-effect." Expected pulse height spectrum in a ^{3}He proportional counter. The low-energy continuum is due to incomplete deposition of energy in the gas as a result of the proton hitting the wall of the counter (shoulder at 191 keV), and the triton hitting the wall (shoulder at 573 keV).

The diameter of the counter is a compromise between neutron detection efficiency for the array, total mass of material in the array, and impact on the PMT light collection. This dimension coupled with the counter gas pressure then confines the anode diameter. These parameters (a, b, and P from above) are the primary factors determining the gas gain as a function of operating voltage. The NCD values were chosen to obtain a reasonably high gas gain (M=100) at a relatively low operating voltage (V=1835 V), thus minimizing the potential for HV breakdown problems. One particular HV concern is microdischarge; events which are characterized by spontaneous, low-current breakdown, and could lead to an additional background in the NCDs.

47

Table 3.1: NCD operating parameters, gas-fill and resolution constants.

Gas-Mixture	^{3}He:CF$_4$ (85/15)
Total Pressure	1900 torr
Anode Wire Radius	.025 mm
Cathode Inner Radius	25.4 mm
Cathode Wall Thickness	0.36 mm
Operating Voltage (Gas Gain)	1835 V (M=100)
Diethorn Parameters K V	2.5 V mm^{-1} torr^{-1} 31.05 V
Resolution Parameters (typical gas values) F f W	0.05 – 0.2 0.4 – 0.7 20 - 30 eV/ion pair

The wall thickness of the counters is a compromise between assuring the physical integrity of the NCDs, and minimizing the potential radioactive contamination associated with the material. Since the bulk U and Th contamination increases linearly with mass, a thinner wall results in less radioactive material in the array. The ultimate limit on wall thickness, however, is set by the total differential pressure on the counter. The NCD tubes are weakest under compression, and so it is the differential compression pressure which dictates wall thickness. At the bottom of the acrylic vessel, the counters will be exposed to an external pressure of 988 torr from the depth of the mine plus an additional 1444 torr from the D$_2$O. The counters themselves are pressurized to 1900 torr, resulting in a 632 torr pressure differential. This is less

of a compression pressure than evacuating the tubes at sea-level. The wall thickness was therefore chosen to withstand a 764 torr (1 atm) compression pressure differential. Each tube is evacuated at UW to test for collapse.

A summary of the NCD physical and operational parameters as well as the ^{3}He:CF$_4$ gas constants (Diethorn Parameters) can be found in Table 3.1.

3.4 NCD Counter Construction

The body of each proportional counter is a 5.08 cm ID chemical-vapor-deposited (CVD) nickel tube. The CVD process involves the heating of a chemical composition, which includes nickel, to approximately 100° C at which temperature the nickel combines with CO to form the gaseous compound nickel carbonyl (Ni(CO)$_4$). At this temperature, only a few elements form carbonyls, resulting in a nickel vapor of higher purity than the original nickel stock. The vapor temperature is then increased to approximately 200° C at which point the nickel carbonyl cracks, allowing only nickel to plate onto an aluminum mandrel at an average rate of 0.75 mm/hr.

Prior to being constructed into a counter, the nickel tubes are cut into lengths of 50, 100, and 200 cm. The tubes are then flared to allow for the eventual joining of adjacent counters.

Each tube undergoes a series of electropolishing and etching steps to clean and prepare the surface. Though the CVD nickel itself is very pure (radioassay results indicate 1-2 ppt U and Th), the aluminum mandrels used in the

49

deposition process degrade over time and occasionally leave aluminum deposits (which have a relatively high U and Th content) on the interior surfaces of the tubes. Furthermore, the tubes are exposed to radon in the air, which may leave behind alpha-emitting daughters. The tubes are electropolished to remove ^{222}Rn daughters, specifically ^{210}Po, which has a 138-day half-life and decays via a 5.3-MeV alpha. The electropolish and a subsequent acid etch also remove aluminum. Etched and polished tubes are then rinsed and vacuum baked as the final preparation procedures.

The tubes are laser-welded together into the final counter lengths of 200, 250, and 300 cm. The welding process utilizes a 1054 nm Nd-YAG laser operating from 0.6 to 1.2 watts.

The endcaps of the counters are also made from CVD nickel. Centered in each endcap is a 5.3-cm-long, 0.5-cm-diameter Suprasil fused-silica high-voltage feedthrough tube. These tubes extend 2.54 cm into the counter volume to minimize gas multiplication in the endcap regions. These have been included in the NCD design because of concerns of possible abnormal ionization profiles as a result of alpha activity in the endcap region. Abnormal ionization profiles may lead to misidentification of events, resulting in a potential background. In addition to the quartz field tubes, one endcap of each counter is fitted with a copper fill tube through which the gas mix is introduced. The endcaps are laser-welded into the nickel tubes.

Each counter is strung with a 50 μm diameter copper wire which is pretensioned with a 30 g mass. Counters are then filled with the 85:15 ratio (by

pressure) of ^{3}He and CF_4 to a total pressure of 1900 torr. The construction of 300 counters required regular preparation of the gas-fill mixture. The preparation procedure as well as quality concerns and checks can be found in Section 3.4.

Readout cable

Cable endcap
with acrylic spacer

Pinch-off
fill tube

Counter body
(^{3}He-CF$_4$ gas mix)

Resistive coupler
(cable end only)

Fused-silica
insulator

Nickel endcap
body

Delay line
termination

Vectran braid
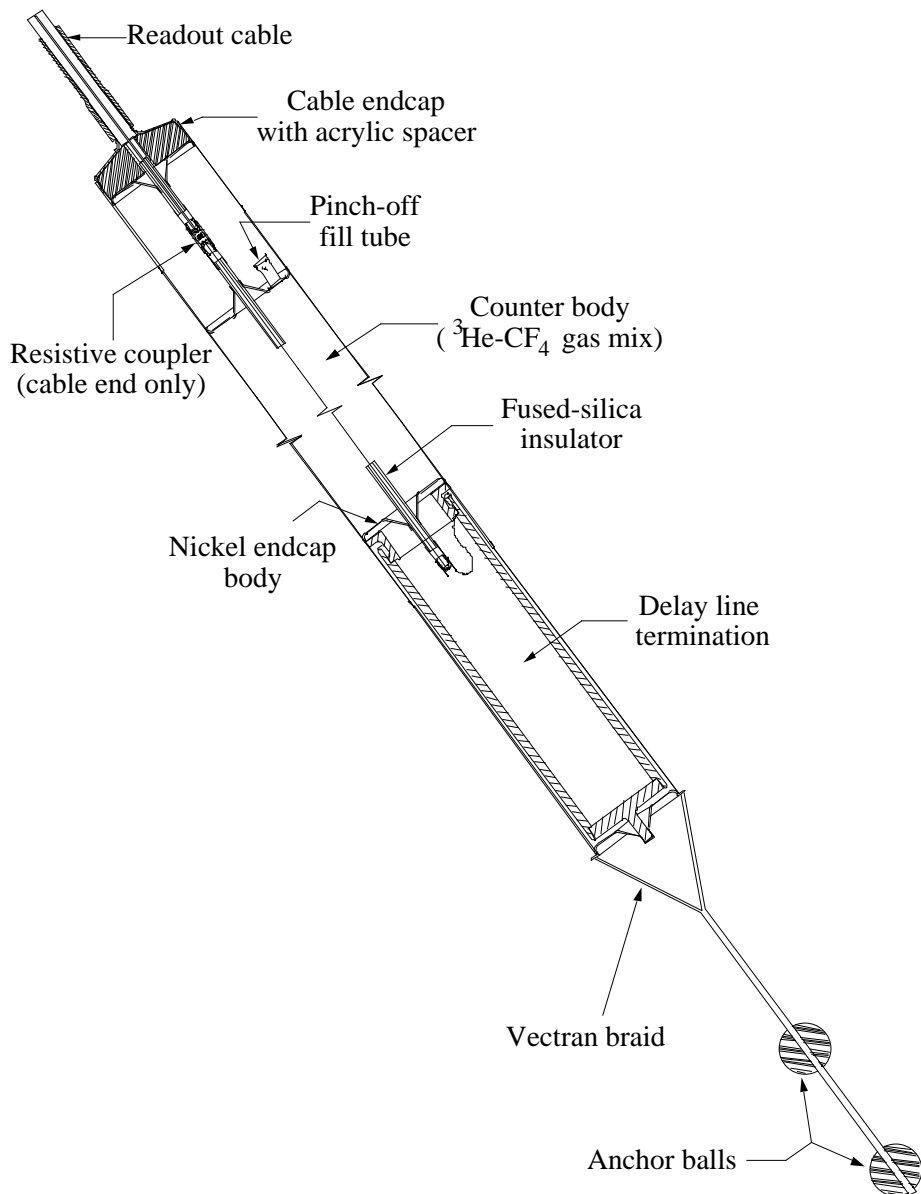
Anchor balls

Figure 3.4: Drawing of an NCD string showing the principle components.

51

Figure 3.4 shows the major components of an NCD string. At the bottom of the figure are shown the two acrylic balls that will be used to deploy and anchor the string to the bottom of the acrylic vessel. These balls are connected to the string by a Vectran[1] braid. Connected to the bottom of each string is a 60-ns delay-line termination that allows for position encoding by analyzing the pulse shape for reflections. Welded to the top of the main counter body is the cable "bell-end" connection. This is a waterproof endcap that mates the HV/signal cable to each NCD string. The electrical connection is made through a 415 coupling resistor to match the impedance of the counter to the 91 impedance of the cable.

The signal cables are constructed with a lightweight woven copper foil shield, and a low-density polyethylene jacket to provide buoyancy in the heavy water and also to meet the stringent radio-purity requirements. The array relies on counter buoyancy to maintain a vertical orientation, and the signal cables must float and conform to the interior shape of the vessel while providing adequate HV characteristics and RF noise shielding.

3.5 NCD Counter Gas-Fill

The ^{3}He:CF$_4$ gas mixture is prepared in many relatively small batches. Maintaining the consistency and purity of these batches over the months of production is a serious concern. Proportional counters rely on the mobility of

---

[1] Vectran is the brand name of a high-strength multifilament liquid-crystal polyester (Hoechst Vectran Co.)

electrons for the development of the signal. Electronegative impurities like air tend to have a high electron attachment coefficient, resulting in a loss of free electrons, and hence signal amplitude. Both constituent gases are filtered prior to mixture to remove such impurities. Figure 3.5 is a schematic representation of the gas purification, mixing, and filling system.

The ^{3}He is obtained from the -decay of ^{3}H which remains in the NCD supply at approximately 1mCi/STP-l. At this level, there would be 10^9 decays/s in an 11 m string, each depositing about 6 keV of energy in the gas. While this is energetically much different than a neutron event, pulse pile-up from ^{3}H would represent a serious background. Prior to mixture with the CF_4, the ^{3}He is circulated through a series of charcoal filters, cold traps, and getters, effectively lowering the ^{3}H content to a few tenths of a nCi/STP-l. At this level, the most sensitive instrument for determining the ^{3}H content is the counter itself. Before a counter is sealed, a low-energy spectrum is obtained and the ^{3}H content is calculated. A limit of 2.7 nCi/STP-l has been set based on a 1% probability of a ^{3}H beta-decay occurring in an assumed 10-μs integration time for neutron capture events.

The CF_4 is purified by circulating the gas through a SAES getter to remove impurities like air and water vapor. Once both constituent gases have been purified, they are mixed in a large volume chamber (22.5 l). The ^{3}He is admitted to a predetermined pressure which is dependent on the length of counter to be filled. The CF_4 is admitted second until the total pressure required to obtain the proper 85:15 (^{3}He:CF_4) mixture is reached. The mixing is done before filling

individual counters to allow the gas to reach equilibrium prior to being introduced to the counter volume.
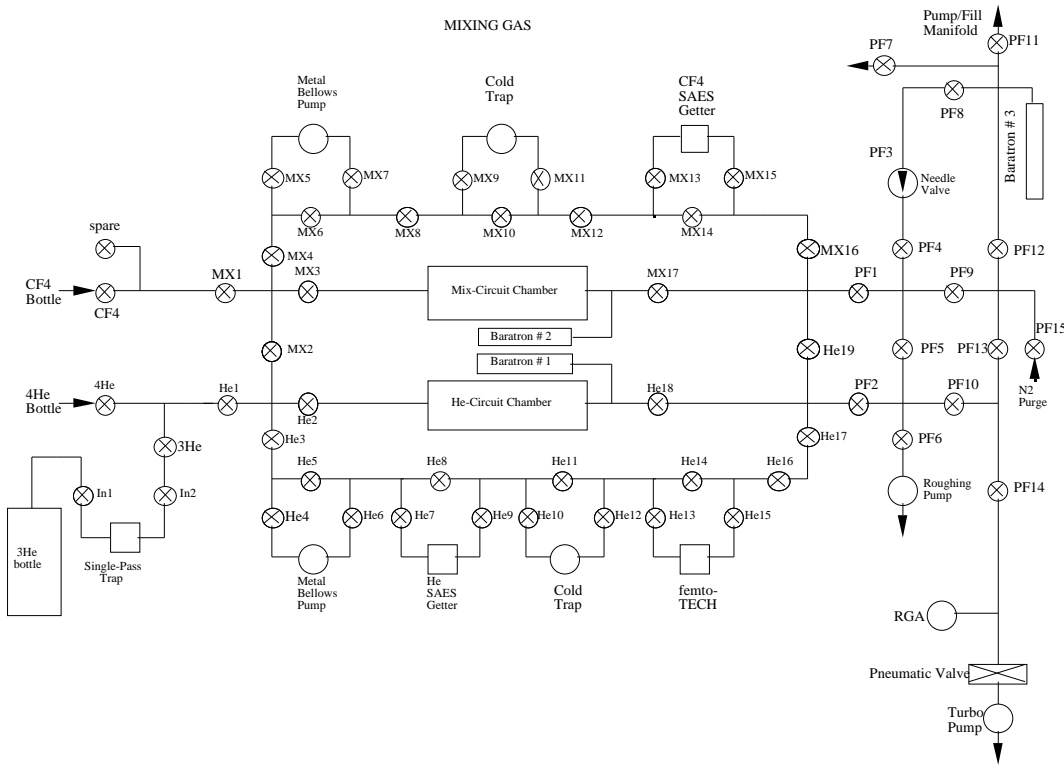
Figure 3.5: NCD gas-mix circuit

The counters to be filled are placed on a gas manifold, allowing up to seven counters to be filled in parallel. The gas mixture is then rapidly introduced to all counter volumes simultaneously until the total pressure reaches 1900 torr (2.5 atm – normalized to the current ambient temperature). This is done to prevent the possibility of gas fractionation which may occur due to the different sizes of the individual components in the gas mixture. Prior to being sealed,

counters are tested to determine the quality of the fill as well as the ^{3}H content. These tests are discussed in the following section.

3.6 NCD Characterization / Production-Phase Diagnostic Tests

There are three stages of diagnostic tests associated with the production and final underground acceptance of NCDs. These correspond to tests performed during detector fabrication, post-gas fill, and underground storage periods. The tests involve digitized waveforms, ADC energy histograms, or a combination of both. The tests are used to determine the quality of material preparation and production techniques. They are also designed to ensure consistency of counter gain and resolution over the production run of 300 counters. Finally, they attempt to ascertain the long-term stability and characteristics of the counters.

Tests performed during counter fabrication are used to identify potential high voltage problems due to cleanliness issues or general microdischarge problems. In either situation, application of HV can result in sporadic discharge. Separation of these spurious events from neutron events can be accomplished efficiently through pulse-shape analysis, but these events can lead to significant dead time. Prior to being welded into a nickel tube, endcaps undergo cleaning and microdischarge testing. The endcaps are placed in an RF-shielded box, and elevated to 2400 volts. Each endcap is monitored for HV breakdown, and any such event is digitized for later review. Endcaps which microdischarge more than 2 times in a 24-hour period are not used in the construction of counters.

Once a counter has been assembled, it is purged several times with N_2 to remove residual O_2. The counter is then pumped to a vacuum of order 10^{-5} torr, and operated at 2400 volts to look for undesirable HV characteristics. Once again, microdischarge is monitored by recording digitized waveforms of all events. A counter that exceeds 3 microdischarge pulses in a 12-hr period is disassembled and repaired.

Counters that pass microdischarge testing are placed on the gas manifold and filled as described in Section 3.4. The pressure inside these counters is monitored for several minutes after filling to maintain 1900 torr. Fill pressure is affected by both ambient temperature and the relaxation time of the gas inside the counters. These combined effects can lead to a several percent error in pressure. Once the system has stabilized, the operational characteristics of the counter are determined.

The measured gain and resolution of a counter are obtained by operating at a low gas gain of ~3. This equates to an applied voltage of approximately 1600 V. A moderated ^{252}Cf source is placed near the counter to provide a flux of thermal neutrons. A 5-minute run results in about 200 events in the 764 keV neutron peak. The energy histogram obtained from this run is used to ensure that the gains of the counters are equal to within +/-2%. This is verified by determining the location of the neutron peak in reference to two calibrated pulser peaks. Figure 3.6 shows a typical histogram. This method is accurate to the 1% level.

n Peak = 1570.0 +/- 0.2
n Res. = 3.6%
Low Pulse = 548.0
High Pulse = 1746.6
^{2}/DoF = 0.83
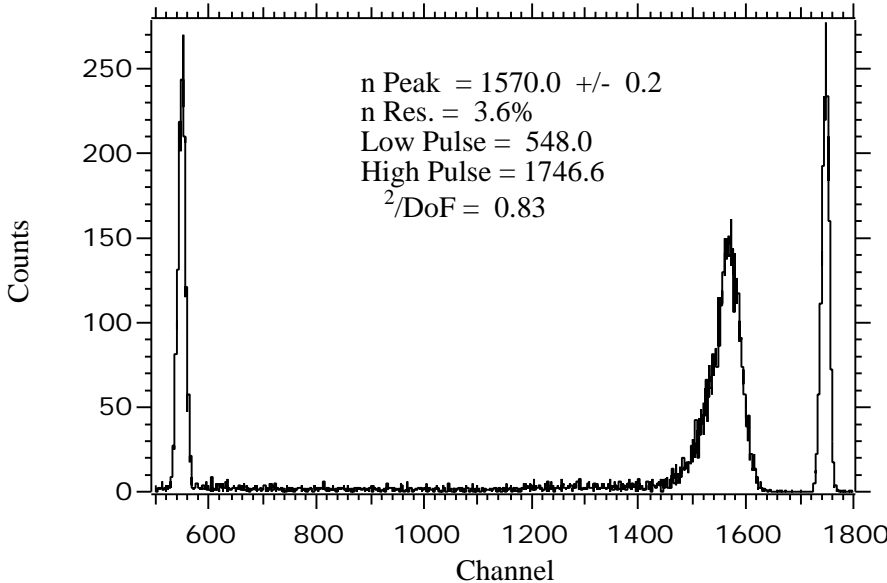
Figure 3.6: Post-gas-fill energy histogram showing the 764 keV neutron-capture peak.

The resolution of the counter is obtained from an analytical fit to the neutron peak. The functional form of the fit is a Gaussian with a low energy exponential tail and flat background [48]. For comparison, the overall statistical limit on the energy resolution of a proportional counter is given by Equation 3.3 [49].

$$\text{EnergyResolution} = 2.35 * \left[\frac{W(F + f)}{E} \right]^{1/2} \qquad (3.3)$$

Where W is the energy required to form one ion pair, F is the Fano factor, and f is ion collection efficiency. These values are constant for a proportional counter gas mixture at a given pressure and operating voltage. Typical ranges for these parameters are listed in Table 3.1. These values yield a calculated maximum statistical resolution of 0.9 – 1.3% at 764 keV. Typical measured values range

57

from 3 – 5%. Poor counter resolution is indicative of a problem with the gas fill and so any counter with a resolution > 5% is evacuated and re-filled.

A 24 hour low-gain histogram is taken after counters are filled and sealed to look for high-energy alpha activity. The primary source of these events is the 5.3-MeV α-decay of ^{210}Po. This radionuclei is a daughter of radon – a ubiquitous gas at room temperature. A more detailed discussion of the Po contamination can be found in Section 4.5.

The most serious concern associated with a large amount of ^{210}Po on the inside surfaces of the NCDs is the potential background resulting from incomplete energy deposition of the α-particle. Not all decays deposit the entire 5.3-MeV of energy in the gas. Alphas which travel a chord of the detector may deposit only a fraction of the full energy which results in a spectral shape exhibiting a continuum up to the total 5.3 MeV. These events can therefore represent a background to the neutron measurement itself. The effects of surface contamination in the NCDs is described in further detail in Section 4.2.3

The electropolish stage of tube preparation removes the majority of this contamination, and it is the 24 hour low gain study which provides information as to the success of this process. These runs show typical alpha activity on order 50-100 counts/m^2/day in the Po window. The accuracy of these surface studies are ultimately limited however by cosmic interactions in the counter. If a counter shows excessive alpha activity in the Po window, tube preparation is stopped, and the source of the contamination is determined.

Upon completion of the alpha tests, counters are placed in a "whole-body" leak checker to determine if there are any leaks at a level of 10^{-7} std cc/s. If no leaks are detected, counters are sealed in a protective nylon bag with a N_2 purge gas[2]. Sealed and bagged counters are boxed in preparation for shipment to SNO's underground experimental site. Figure 3.7 is a flowchart of the tests taken during NCD construction.

Measurements underground have the advantage of the SNO site's 5900 m.w.e of overburden. All but the most energetic of cosmic rays have been attenuated at this depth. Low-background measurements in a near final environment are therefore possible. Counters taken to site then enter what is referred to as the "cool-down phase." This period of time is described in Chapter 4.

---

[2] Tubes and counters are enclosed in a nylon sheath throughout the construction process. When not in use, the nylon is sealed.

Endcaps   Tubes

Endcap
Microdischarge Tests

   Nominal Value: 0-1/24hr
   Limit: 2/24hr

Surface Preparation

Counters Assembled

Tube Alpha Tests
(not every tube)

Nominal Value: 50-100 /m^2 /day
Limit: 300 /m^2 /day

Counter
Microdischarge Tests

   Nominal Value: 0-1/12hr
   Limit: 3/12hr

Gas Fill

Tritium Tests

   Nominal Value: 0.1-0.2 nCi/l
   Limit: 2.7 nCi/l

Counters Sealed

Counter
"Whole-Body" Leak Tests
  Nominal Value: ~10^{-8}
  Limit: 10^{-7} std cc/s

Alpha Tests

Nominal Value: 50-100 /m^2 /day
Limit: 300 /m^2 /day

Figure 3.7: NCD Construction Testing Flowchart

<center>**Chapter 4**</center>

4.1 NCD Cool-Down Phase

The NCD group has developed material preparation and construction techniques to produce counters with intrinsically low levels of ^{238}U and ^{232}Th. As previously described, the decay chains of these radioisotopes give rise to background neutrons through photodisintegration of deuterium. There is an additional problematic isotope, however, which is a spallation product of cosmic ray neutrons with nickel as shown in Equation 4.1 (The isotopic abundance of CVD Ni is the same as the natural isotopic abundances: 68% ^{58}Ni and 26% ^{60}Ni). By far, the majority of the NCD array by mass is nickel, and so the cosmogenic activation of the array must therefore be considered.

$$^{58}\text{Ni} + n \quad p + 2n + ^{56}\text{Co} \quad (Q = -8.6\text{MeV})$$

$$(4.1)$$

$$^{60}\text{Ni} + n \quad p + 4n + ^{56}\text{Co} \quad (Q = -20.5\text{MeV})$$

^{56}Co decays through electron capture and subsequent -emission with a relatively short 78 day half-life. The energies range from ~0.3 – 3.6 MeV, with approximately 31% of the emitted gammas having sufficient energy to photodisintegrate deuterium. This isotope therefore represents an additional source of background neutrons if the cosmogenically activated array is to be immediately placed in the D_2O. Material preparation will remove some surface ^{56}Co, but only underground storage can ensure this additional activity decays away.

<center>61</center>

In order to determine how many ^{56}Co atoms are produced, and how many photodisintegration neutrons the associated activity will produce in SNO, the total decay rate of ^{56}Co atoms ($dN_{^{56}Co}/dt$) in the NCD nickel must be calculated. In Equation 4.2, the linear production rate ($R_{^{56}Co}$) is combined with an exponential decay which is characterized by a decay constant ($\lambda_{^{56}Co}$).

$$dN_{^{56}Co} = R_{^{56}Co}dt - \lambda_{^{56}Co}N_{^{56}Co}dt \qquad (4.2)$$

The total ^{56}Co decay rate is therefore given in Equation 4.3 by solving and taking the time derivative of Equation 4.2.

$$dN_{^{56}Co}/dt = R(t) = R_0(1 - e^{-\lambda_{^{56}Co}t_e}) \qquad (4.3)$$

This rate, as a function of exposure time t_e and the saturation decay constant R_0, is shown in Figure 4.1 (assuming no initial ^{56}Co burden).

The nickel tubes used for the NCDs have a cosmic ray exposure time which indicates that they have essentially reached saturation. When the counters are taken underground, the ^{56}Co decay rate shown above decreases as a function of time (t_u) according to typical exponential decay as shown in Equation 4.4.

$$R(t) = R_0(1 - e^{-\lambda_{^{56}Co}t_e})e^{-\lambda_{^{56}Co}t_u} \qquad (4.4)$$

Equation 4.4 can then be used to determine the number of photodisintegration neutrons from the decay of ^{56}Co as a function of underground storage time. Monte Carlo studies show that one photodisintegration neutron will be produced for every 1140 ^{56}Co decays [50]. The number of neutrons is then given by R(t)/1140. There is a total of 450 kg of Ni used in the array, and the equilibrium decay rate of ^{56}Co (R_0) is 24.22 decays/day/kg [50]. Figure 4.2 shows

the calculated number of neutrons produced in SNO as a function of underground storage time (t_u).
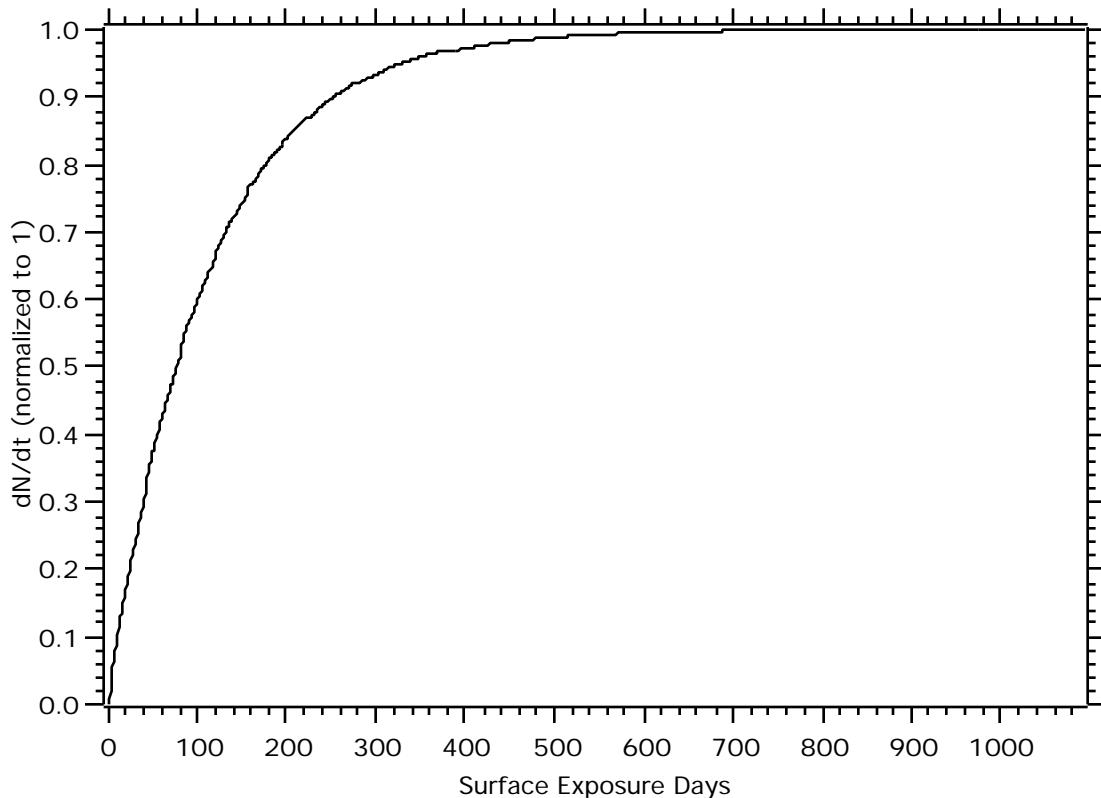
Figure 4.1: ^{56}Co decay rate in Ni as a function of days exposed to cosmic rays at sea level. This rate is shown approaching a maximum value known as saturation, and requires approximately 3 ^{56}Co half-lives to reach 90% saturated.

In order to keep the neutron background below a few percent of the expected NC signal, there must be fewer than 1 neutron/day from the decay of ^{56}Co. If the counters are saturated, Figure 4.2 indicates an underground storage period of nearly 200 days to allow the cosmogenically produced activity to decay away prior to NCD deployment. This storage period has been appropriately named the "cool-down phase."

63

This estimate assumes that the entire array has reached saturation, and that the array is taken underground all at once. Counter production at the University of Washington rarely exceeds 10 counters a week, and many weeks it is actually much less. As a result, counters are driven up to Sudbury in batches. As of February 1999 approximately 117 meters of counters have been delivered to site and taken underground (~15% of the array). These counters have been in the cool-down phase for almost 100 days. It is therefore most likely that the majority of the array will have been underground more than 200 days prior to the final components of the array arriving at site.
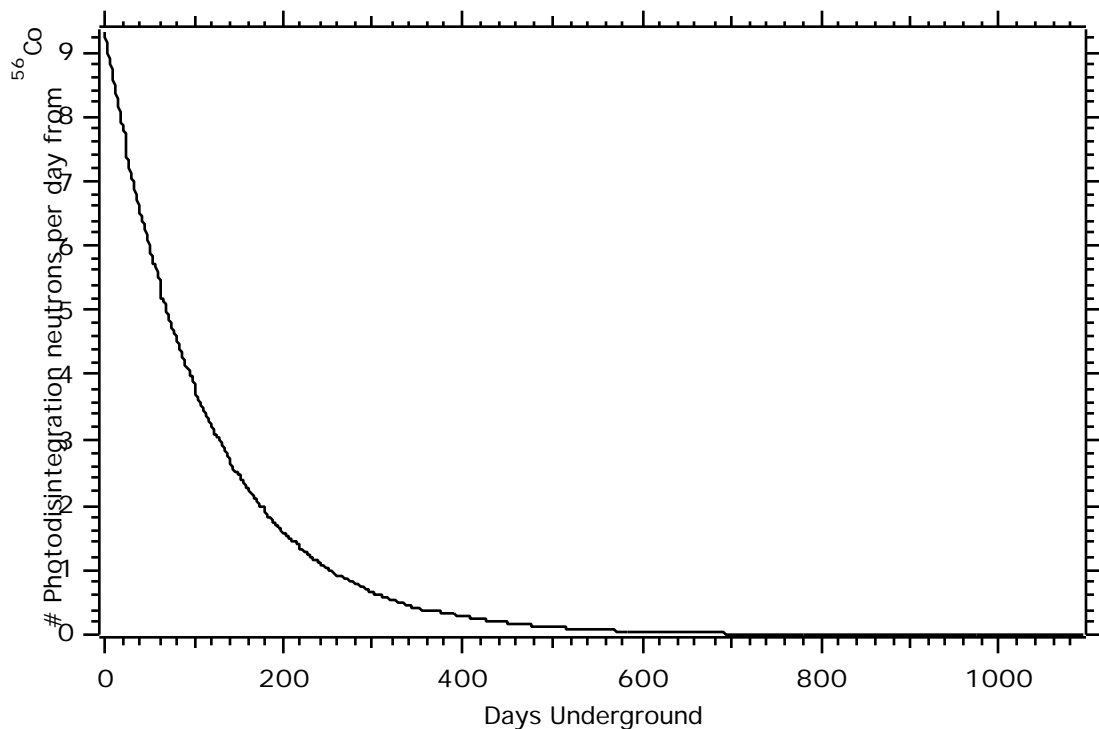
Figure 4.2: ^{56}Co induced photodisintegration neutrons per day as a function of underground storage time assuming saturation of the entire NCD array.

4.2 Cool-Down Phase Goals

The underground storage phase presents an excellent opportunity to run the counters in the underground environment. The initial production and testing of the counters are performed in a "controlled" lab environment at the University of Washington. An active underground mining environment is a much less hospitable setting for sensitive electronics and detectors. Operating and characterizing the counters underground therefore allows the NCD collaboration the opportunity to debug acquisition and analysis systems prior to actual deployment. Additionally, because the SNO facility is located over 2000 meters underground, the cool-down phase enables careful studies of potential backgrounds in the absence of cosmic rays. These backgrounds can be grouped into two categories: backgrounds due to the environment (thermal and fast neutrons, gammas from the U and Th chains), and intrinsic backgrounds to the counters (alpha particles from ^{238}U, ^{232}Th, and their daughters). One goal of the cool-down phase is therefore an attempt to quantify these backgrounds.

The primary goal of the cool-down phase however is to allow the cosmogenically activated ^{56}Co to decay away by storing the NCDs underground. Confirmation of the decay by direct observation of the -induced Compton events is difficult due to a large background (fission 's from the surrounding rock, 's from the U and Th decay chains). Principal tests during this storage period are therefore designed to characterize individual counters and monitor them for stability. Concurrent with these tests are measurements to ascertain the thermal neutron flux as well as the ^{210}Po, ^{238}U, and ^{232}Th contamination levels by

analyzing the   's emitted by the decay chains of these isotopes. This program of characterizing counters and measuring background levels is described below.

Data from the cool-down phase are recorded as ADC energy histograms and digitized waveforms. Figure 4.3 shows the schematic layout of the cool-down electronics and data acquisition (DAQ) system. This system is a combination of commercially available and custom designed and built electronics. The ADC and digitized waveform acquisition techniques maximize the information content for each proportional counter event under a range of potential situations. The array is essentially designed to detect an anticipated 15 NC neutrons per day in 1000 metric tons of D_2O against a background of   and events associated with the ^{210}Po, ^{232}Th, and ^{238}U found in the construction materials. By digitizing the current pulse of each counter event, the information contained in the structure of the pulse can be utilized, allowing for a more robust off-line separation of signal from background than that provided by a simple energy discrimination.

In certain high-rate situations however, digitizing every event is not possible due to inherent limits in the digitization and data-download processes. The cool-down phase uses a Tektronix 754A 4-channel digitizing oscilloscope to provide the digital waveform of each event. The scope has a limited (50k) amount of on-board memory, and therefore must be read-out on an event-by-event basis through a standard GPIB interface. Tests were performed to assess the dead time associated with the digitization and download of 5k record lengths on 4 channels operating simultaneously at 500 megasamples/sec (MS/s). Figure 4.4 shows the observed versus actual rate. A fit to Knoll's model of

66

nonparalyzable response [52] indicates a deadtime of 1.1 seconds for each triggered event. The DAQ code currently does not utilize the Direct Memory Access (DMA) capability of the system. When implemented, a factor of 10 improvement in speed is expected. Under high-rate testing situations, this large dead-time can create difficulties. In contrast, many tests simply require a pulse height spectrum to obtain the gain and resolution of the counters. In these cases, energy histograms can be obtained much quicker – a useful feature when characterizing a large set of counters.
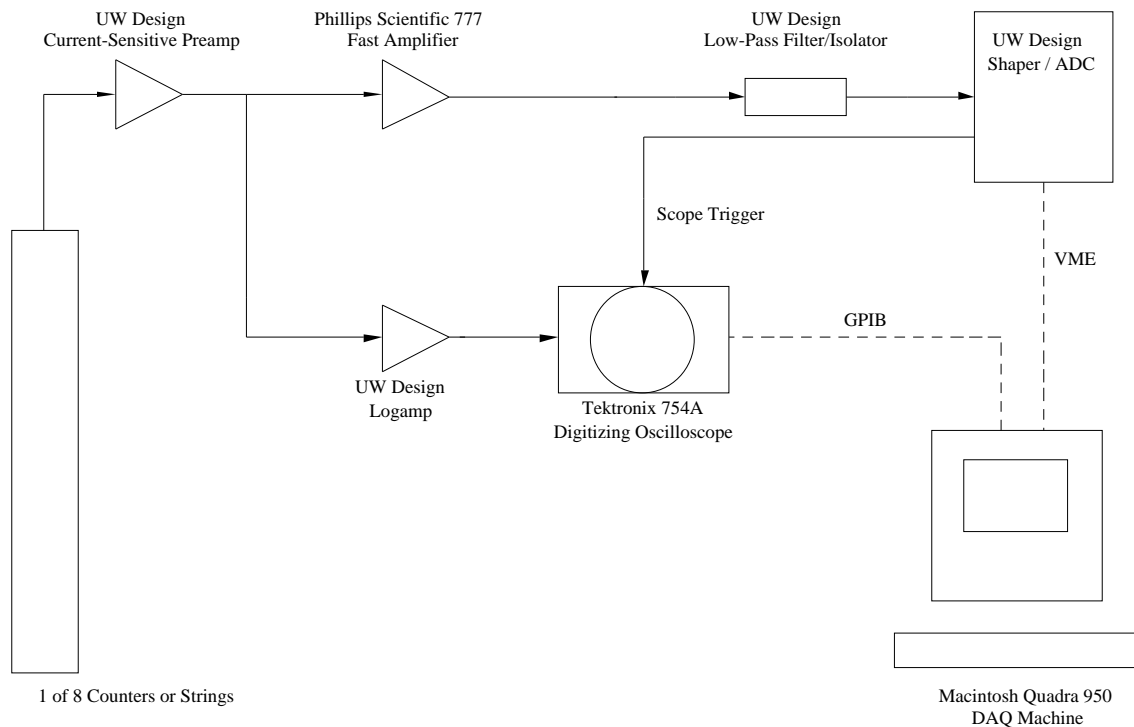
Figure 4.3: NCD cool-down electronics and data acquisition system. The low-pass filter/isolator and shaper/ADC are described in detail in Appendix 4.

67

The cool-down system is capable of simultaneously recording 8 ADC channels and four digitized channels, and can be run in any combination of both. Event triggers are generated by the shaper/ADC board which is described in Appendix 3. While both data format systems utilize the same trigger, the individual data streams are recorded separately.
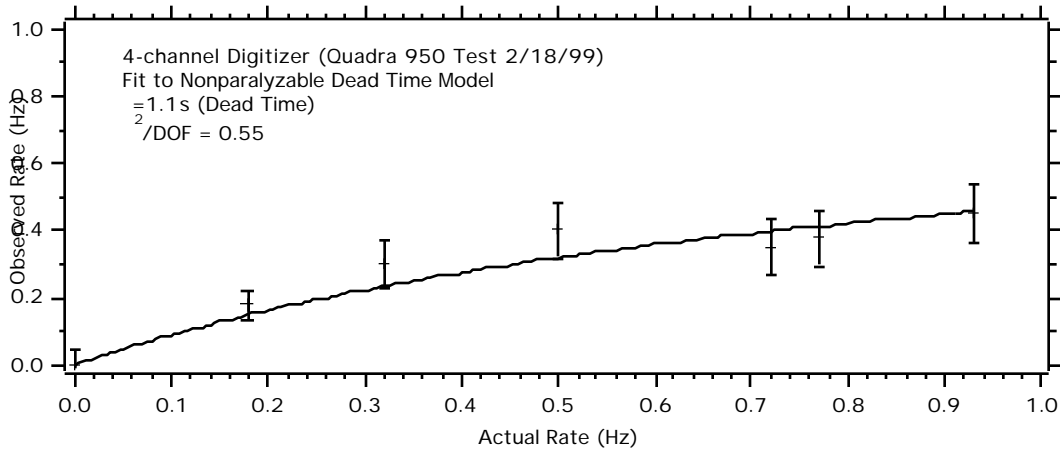
Figure 4.4: Comparison of observed to actual rate for digitization of NCD data. Tests performed on 4 channels simultaneously operating at 500MS/s and 5k record lengths. Included in the rate is the time required to read the data through the GPIB bus.

The preamps used during the cool-down phase are a custom, current-sensitive design. The gain is 25 mV/μA with a bandwidth of ~30 MHz. Preamp input impedance is 91 to match the impedance of the NCD cable. The remainder of the system has a nominal 50 input impedance.

The dynamic range of current signals from the preamp is approximately 190 [53]. The smallest current produced in an NCD (~130 nA) is the result of a

68

proton originating near the wall of the detector traveling towards the anode. By contrast, the largest current pulse (~25 µA) comes from alphas near the detector wall travelling parallel to the anode. If the 8-bit digitizer was scaled such that the 625 mV alpha pulses (25 µA × 25 mV/µA) correspond to the full 256 bits of the digitizer, the smallest signal would be equivalent to 1.5 bits, and thus have a resolution of only 50%. For this reason, the signal to be digitized is amplified according to the logarithmic relation shown in Equation 4.5, effectively making the digitization error constant while $V_{in} >> b$, and acceptably small (~4%) for smaller V_{in}.

$$V_{out} = a \times \log(1 + V_{in}/b) + c$$

(4.5)

The constants a, b, and c are periodically extracted by digitizing a half-sine wave at the input and output of the logamp. Code was written to plot the output as a function of the input, and determine a fit to the analytical form of Equation 4.5. The constants are determined from the fit parameters (See Appendix 2 for more details), and have typical values of a~150 mV, b~15 mV, and c~25 mV. Prior to analyzing digitized data, individual events must therefore first be "de-logged." A description of this process as it impacts the analysis of digitized waveforms is included below in Section 4.3

The current data acquisition machine is a Macintosh Quadra 950. The DAQ code to run the system is written in C++ by the University of Washington and Los Alamos National Laboratory within the same general framework as the overall SNODAQ system.

4.3 Digitized Waveform Analysis (UW_Analyst)

Recording data as digital waveforms required the development of a code to extract, de-log, and analyze events. UW_Analyst was written for small-to-medium sets (1000 events) of digitized waveforms from the cool-down phase. The code was written in the Igor Pro™ application – a data analysis and graphical interface package created by WaveMetrics Incorporated. The DAQ system records waveforms in a custom data structure format which was defined by the NCD collaboration. This format maintains manageable data file sizes for memory considerations. A typical waveform consists of 5000 bytes per channel, and often four channels are digitized per event – requiring 20k of memory per trigger. Prior to being analyzed, these events are extracted into an ASCII file which can then be read by the analysis routine. There are currently two custom extraction applications in use.

The UW_Analyst code loads the entire ASCII file prior to analysis. For a typical data file containing 300 events, the code requires a minimum of 6 Mb of RAM, and double this amount if both the linear and logged pulses are to be retained. As data file sizes increase, so does the required RAM to analyze the events. The drawback of this architecture is immediately obvious when attempting to analyze large (>1000 event) data files. This design, however, has the advantage of immediate access to each event on all recorded channels. If so desired, the analysis results of each event can be retained with the digital "snapshot" of the event topology.
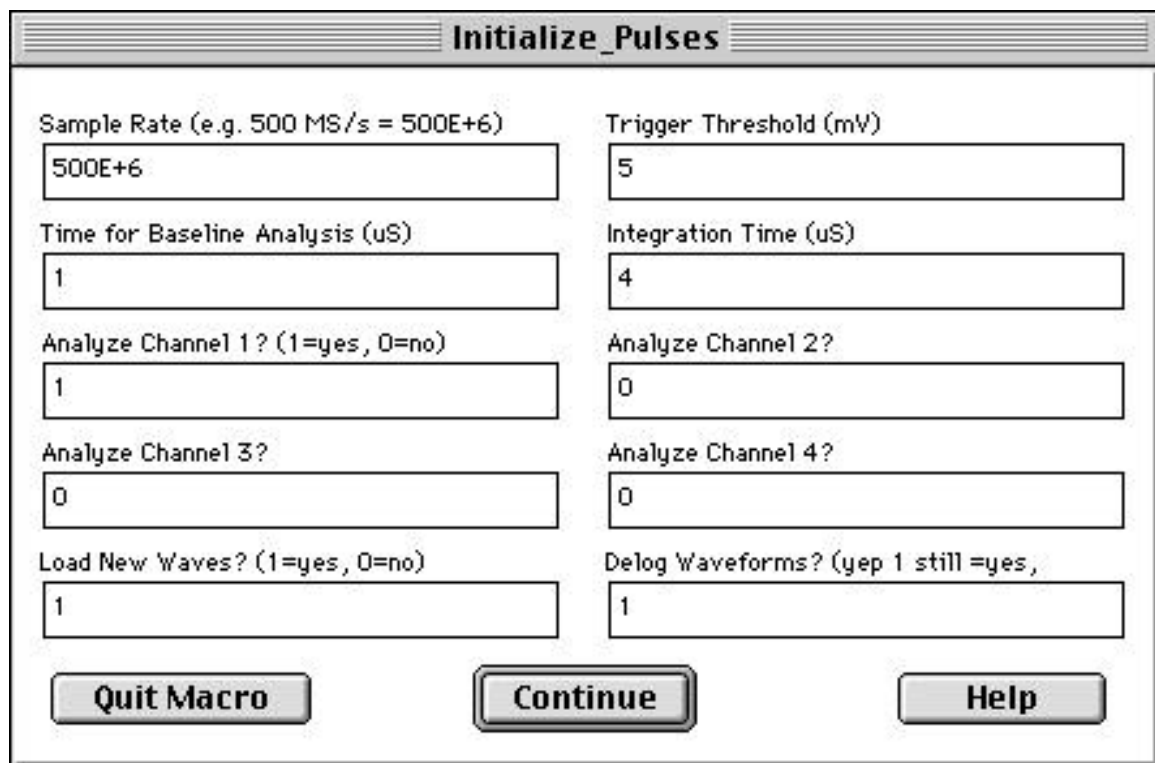
Figure 4.5: UW_Analyst user interface containing typical analysis values.

The graphical interface shown in Figure 4.5 prompts the user for the analysis parameters. This "Initialize_Pulses" dialog is used to pass information to the analysis code regarding the digitization speed (and hence time base), analysis threshold and pulse integration time, as well as giving the user the option of analyzing a subset of channels. If the logamp was used, this dialog also enables the routine to access the logarithmic constants to convert the events back to linear pulses.

Once the user has entered parameters into the fields of Figure 4.5, the code begins stepping through the analysis one event at a time. If the logamp was

used, the event is first de-logged according to the latest extracted constants. Figure 4.6 shows a logged and its associated linear event.
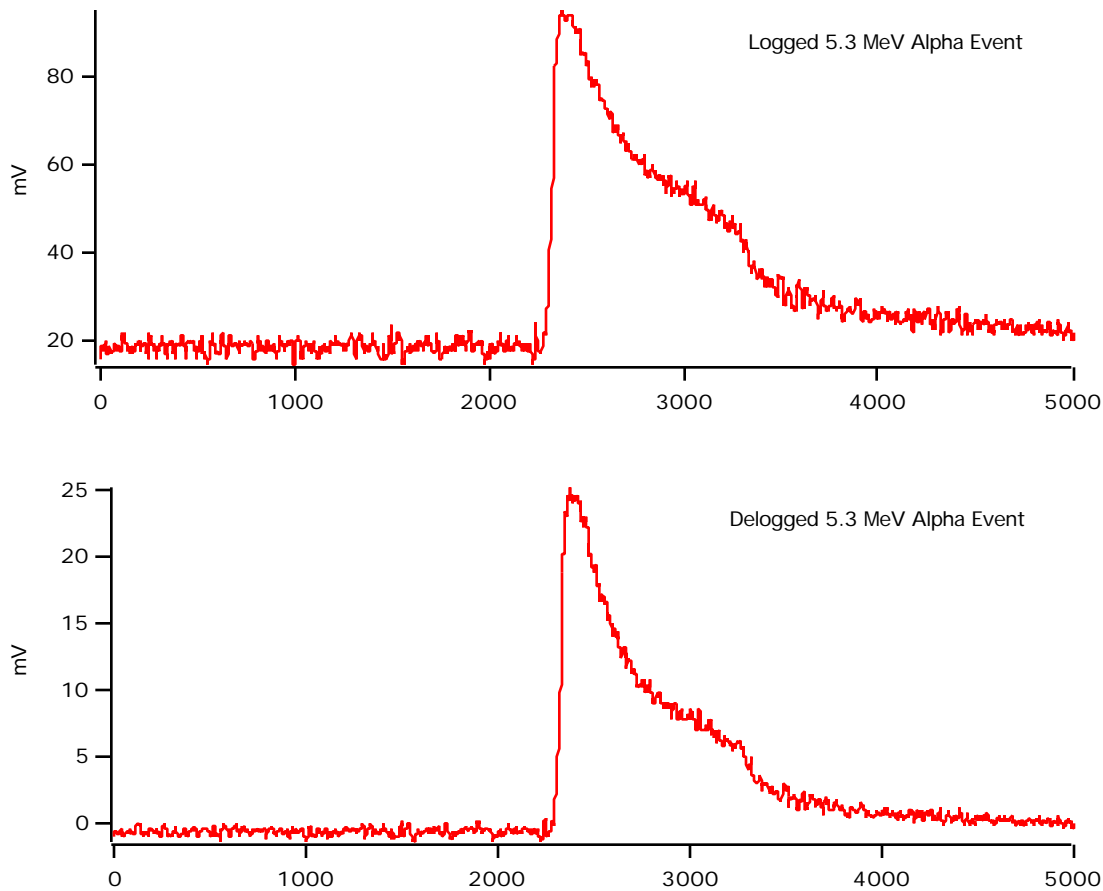
Figure 4.6: 5.3 MeV alpha event. The top waveform is the recorded logged event. The bottom waveform is the de-logged event which is analyzed by UW_Analyst.

Because all digitized channels in the cool-down setup share a common trigger, for each event on any given channel, the remaining channels digitize noise. Therefore, the next task of the analysis routine is to scan the event for a threshold crossing. This threshold is set by the user in the interface dialog shown

above. If such a crossing is found, the analysis proceeds, if no crossing is found, the routine increments to the next event.

Refer to Figure 4.7 throughout the following description of the analysis functions. Once a threshold crossing is found, the code steps backwards along the digitized waveform until the baseline noise of the channel is reached. The baseline is determined by averaging the pre-trigger of the waveform for a period of time as entered in the "Initialize_Pulses" dialog box. The start of the pulse, t_0, is defined as the point where the code has reached this baseline level. The pulse is then integrated from t_0 to t_{int} – the analysis integration time also entered in the "Initialize_Pulses" dialog box. The integrated charge of the event is then given by $Q_{int}= Q(t_{int})-Q(t_0)$ as shown in Figure 4.7. (Recall from Section 3.2 that the collected charge is proportional to the energy of the ionizing particle(s).)

The rise time of the pulse is also determined from the integrated waveform. It is defined as the time (t_f) taken for the event to reach $Q_{int}/2$. For each event, these parameters t_f and Q_{int} are recorded.

The code compares the extracted parameters (t_f and Q_{int}) for each event to a series of analysis regions. This tracks the number of events which fall into a particular region in the rise time versus energy phase-space. Once the event has been characterized, the routine analyzes the next event on that particular channel. The code proceeds until all events have been analyzed on all specified channels. The user can then view the results in tabular, scatter plot, or an energy histogram form. Figure 4.8 shows a typical rise time versus energy scatter plot of analyzed neutron events.
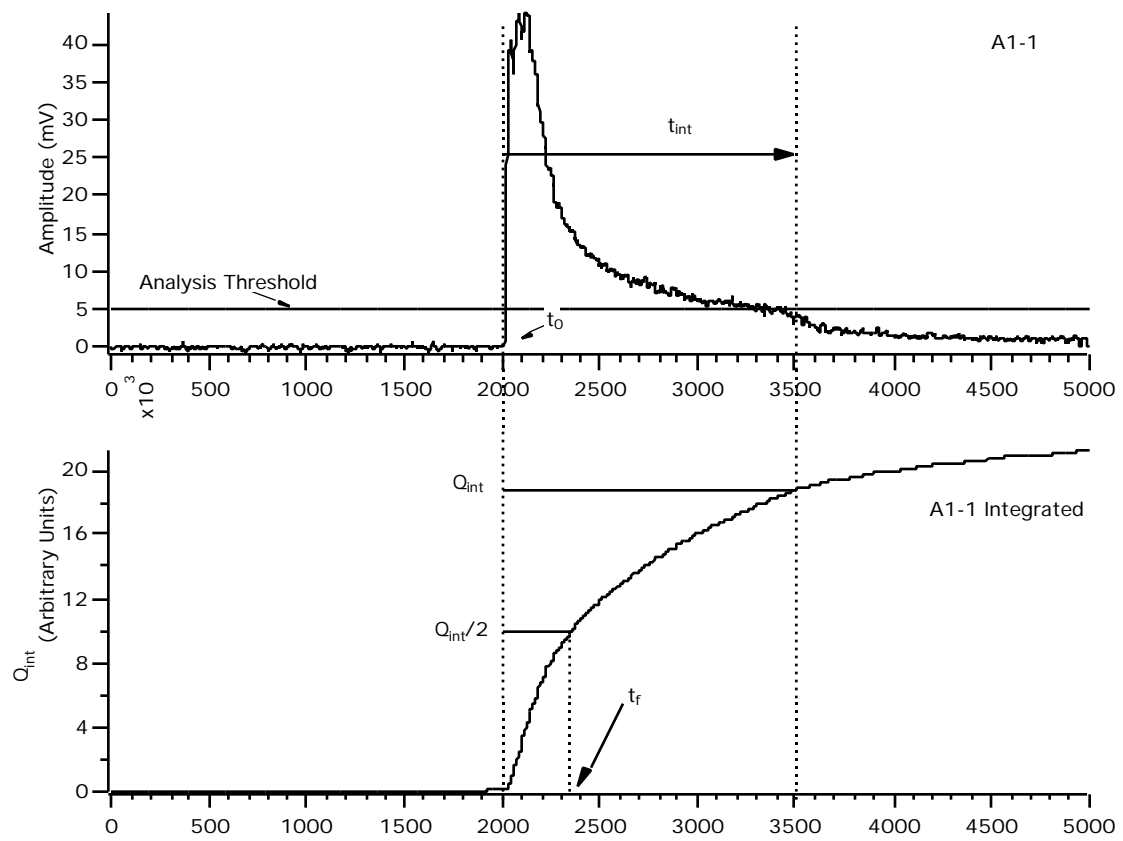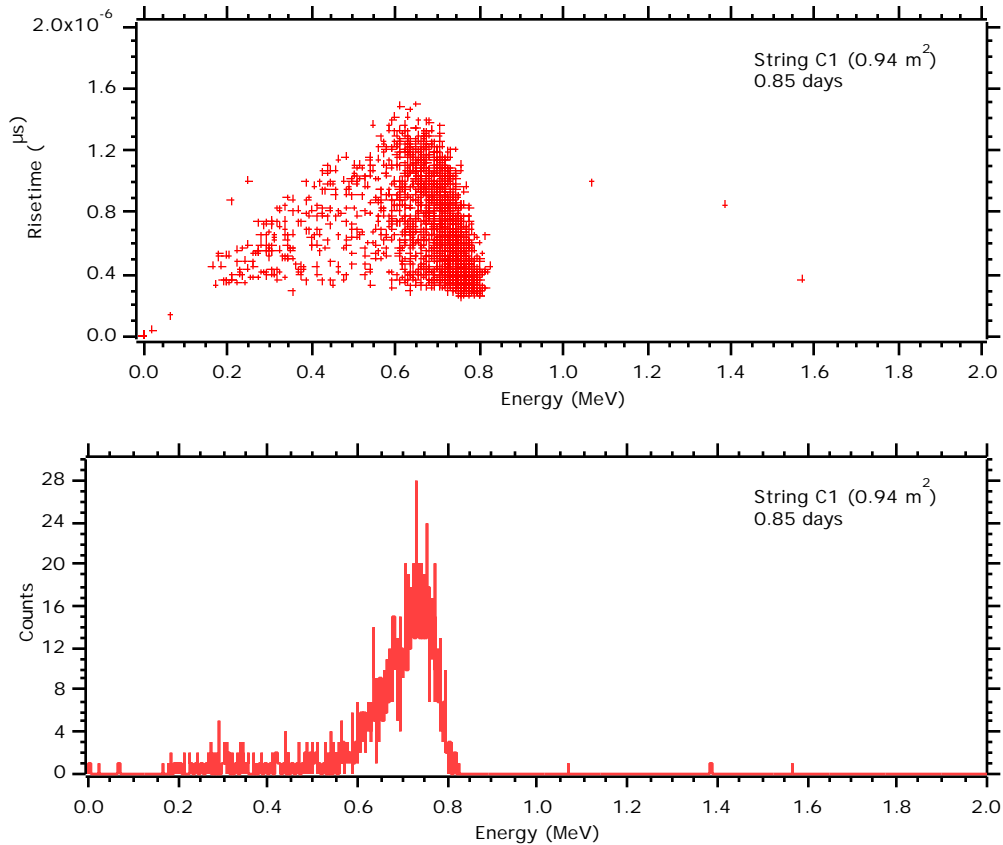
Figure 4.7: UW_Analyst analysis parameters.
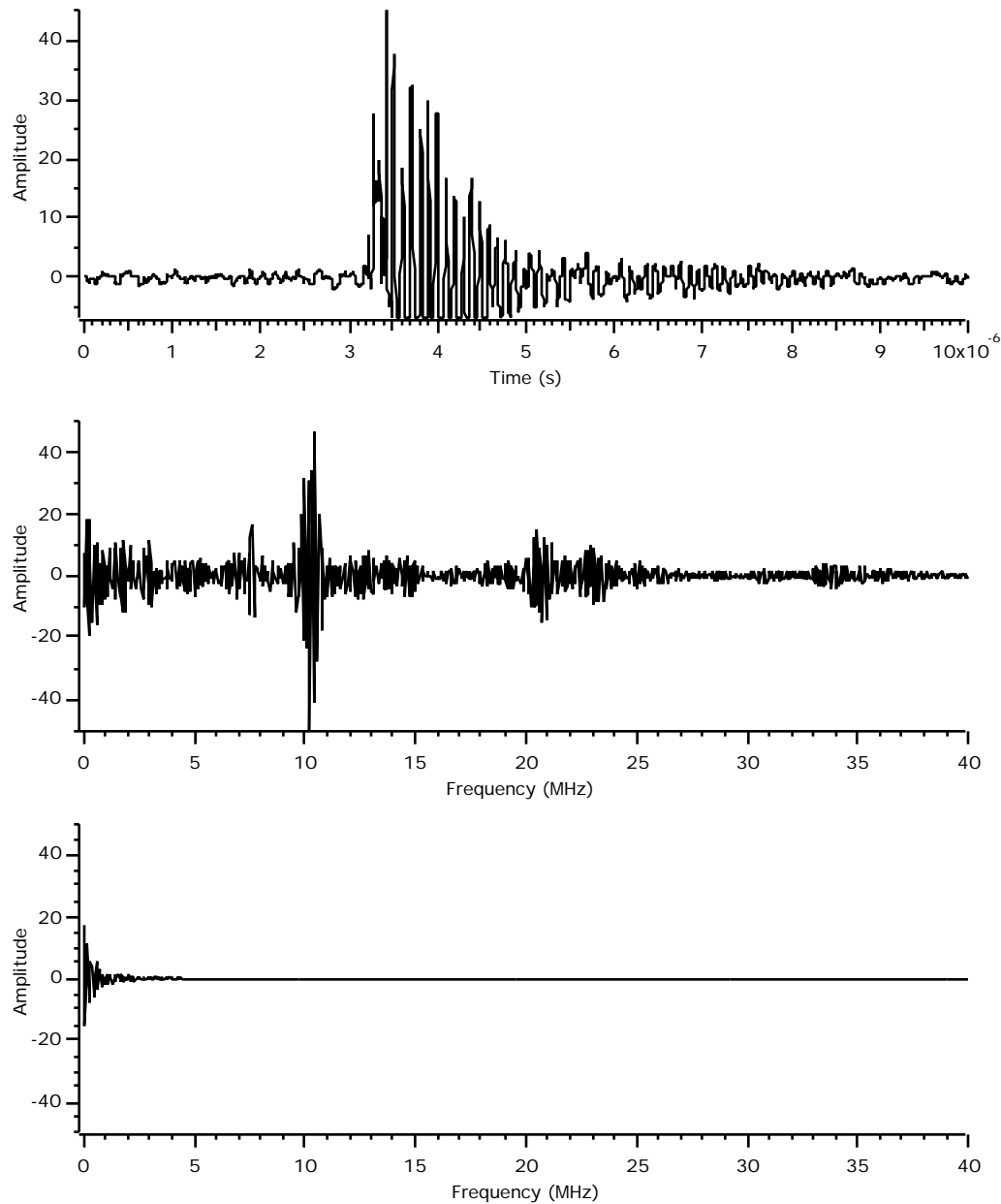
Figure 4.8: Risetime vs. energy (T vs. E) scatter plot of digitized neutron data (top). Histogram of the scatter plot data (bottom)

As previously mentioned, operating sensitive electronics and detectors in an active mining environment is quite different from laboratory based testing. It became apparent that the NCD storage rack was susceptible to induced noise through microphonic pickup. If the amplitude of the induced noise is sufficient to saturate the preamp, a high-frequency transience is observed at the preamp output. The problem would be quite noticeable if the detectors were operated without the coupling resistors for impedance matching. Figure 4.9 shows one such event.

The topology of these noise events is drastically different from a typical proportional counter gas event. Unfortunately, prior to digitization, the noise events become truncated and offset in amplitude due to the logamp. As a result, the originally bi-polar noise pulse is now largely uni-polar, and can integrate to a positive value in the analysis routine, thus contaminating a window of interest.

A software filter was added to the analysis code which looks for these types of events based on their appearance in the frequency domain. A FFT is applied to each event, and a cut is made based on the magnitude of the frequency components above 20 MHz. The values which define the cut were based on the visual inspection of the FFT's of real and noise events.

The middle graph of Figure 4.9 shows the FFT of the noise event at the top of the figure. A FFT of a typical proportional counter gas event is shown at bottom for comparison. On the scale of this figure, an event with a frequency component above 20 MHz and an amplitude greater than 2 would be filtered. Examination of analyzed data sets show that the filter is 100% efficient at removing these noise events. It was noticed however that 0.29% of the events that did not pass the filter were real gas events. Examination of these pulses showed that they were characterized by an extremely fast rise time (hence the high frequency component in the FFT) and very little integrated charge. For this reason, they tended to fall in a non-critical region of the T vs. E phase space. Regardless, a more robust filter should be developed.

Figure 4.9: UW_Analyst noise filter. Microphonic-induced noise event (top), FFT of noise (middle), and FFT of typical gas event (bottom)

4.4 Cool-Down Phase Tests: Counter Installation Underground / Initial Characterization

The first tests performed on the NCDs upon entering the cool-down phase are designed to ascertain the physical integrity of the counters. As discussed in Section 3.4, the NCD HV feedthrough/field shaping tubes are made of Suprasil quartz. The outside of the tube in the vicinity of the quartz-to-nickel interface is metalized with a layer of chromium and a layer of nickel via a radio-frequency (RF) sputtering method, thus enabling the quartz to be soldered into the nickel endcap. The different thermal coefficients of expansion for the quartz and the nickel make this joint susceptible to temperature extremes. This joint is additionally susceptible to physical jarring or impact. For these reasons, successfully transporting operational counters to site has proven extremely difficult. Commercial shipping methods have demonstrated a 100% failure rate, resulting in the partial destruction of every counter shipped using these means. Individual counter components, specifically those parts made from CVD nickel, are in short supply. Certain parts are reusable, but in general, the supply is finite and small.

As a result, all counters are now delivered to site by an individual(s) driving small batches (10-50 counters) in a University of Washington vehicle (2000 miles one-way). This allows a constant control over the temperatures to which the counters are exposed, and virtually ensures careful handling[1].

Upon arrival at site, the counters must be loaded into steel box-cars for transport underground. These railcars are used for moving all SNO materials

---

[1] Careful handling of the counters is insured if the graduate student doing the driving expects to obtain his/her degree in a reasonable period of time.

from the surface building to the INCO collarhouse[2]. The two hazards associated with this process are physical jarring by the railcar transport underground, and the possibility of the railcar being left outside between the SNO building and the collarhouse. In the latter case, there is no environmental control inside the box-cars, and winter temperatures in Sudbury can reach well below −30° C. In general, these problems are avoidable, and so the goals of the first tests were simply to verify the survival and functionality of each counter.

Theses test primarily involved a visual inspection of the counters, ensuring that the endcaps were intact, and measuring the resistance of the anodes to look for electrical shorts. Counters that passed visual and resistance tests were placed in the cool-down storage rack shown in Figure 4.10. Counters that failed these tests were returned to surface for eventual shipment to the University of Washington and repair.

---

[2] The collarhouse is the building enclosing the mine shaft. It is used as a staging area for the organization of personnel and materials to be shipped underground.

Figure 4.10: Underground NCD cool-down storage rack designed and built by the LBNL NCD collaborators. The counters shown have been temporarily assembled to be operated as strings ranging in length from 4 to 11 meters.

The operational characteristics of the counters are then determined. The gain and resolution of each individual counter is recorded and monitored periodically to assess counter stability. Equation 3.1 shows that the gain (M) of a proportional counter is dependent on 1/pressure (M p^{-1}). A gas leak will

80

therefore manifest itself over time as a slow increase in gain. Additionally, a leak will result in a contamination of the fill-gas, adversely affecting the resolution of the counter.

In order to accurately determine the relative gain of a large number of counters in a reasonable time scale, a simple yet robust test was required. The gain and resolution of the counters are obtained from an energy histogram generated by the data acquisition system and the 8-channel shaper/ADC board shown in Figure 4.3. The shaper/ADC essentially integrates an input pulse with a 4 μs time constant, and determines the amplitude of the shaped pulse via a peak-detect ADC. In order to separate the gain of a counter from the individual electronics channel gain, two pulser amplitudes are injected. The amplitudes and widths of the pulser waveforms are set such that their integrated values frame the neutron peak. Additionally, the integrated amplitude of the second pulse is twice the integrated amplitude of the first. Figure 4.11 shows the resultant spectrum.

The gain of a given counter can then be described by the location of its peak in relation to the two pulser peaks. This is done by plotting the ADC channel location of the pulser peaks versus the integrated value of the pulser waveform (in arbitrary units). The gain factor of a counter is then defined by the intersection of the ADC channel value of the neutron peak with the pulser gain line as shown in Figure 4.12.
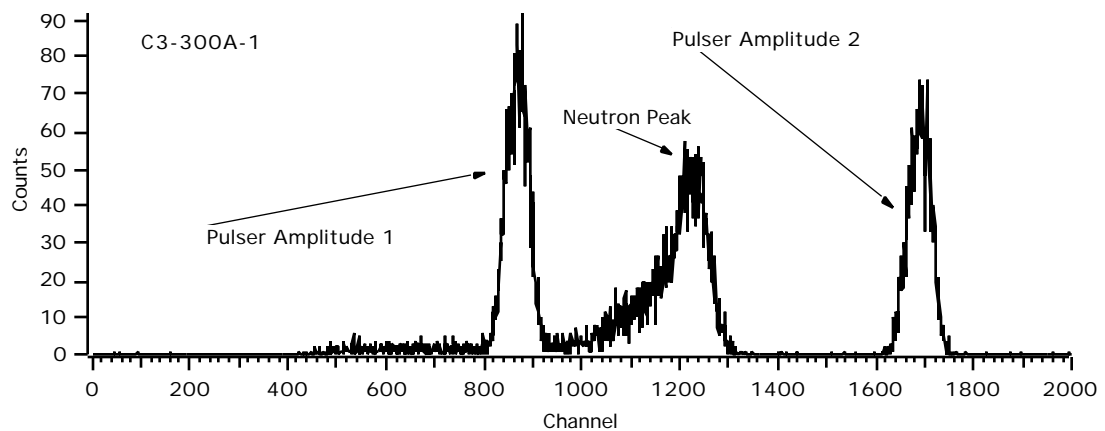
Figure 4.11: Counter characterization energy histogram.
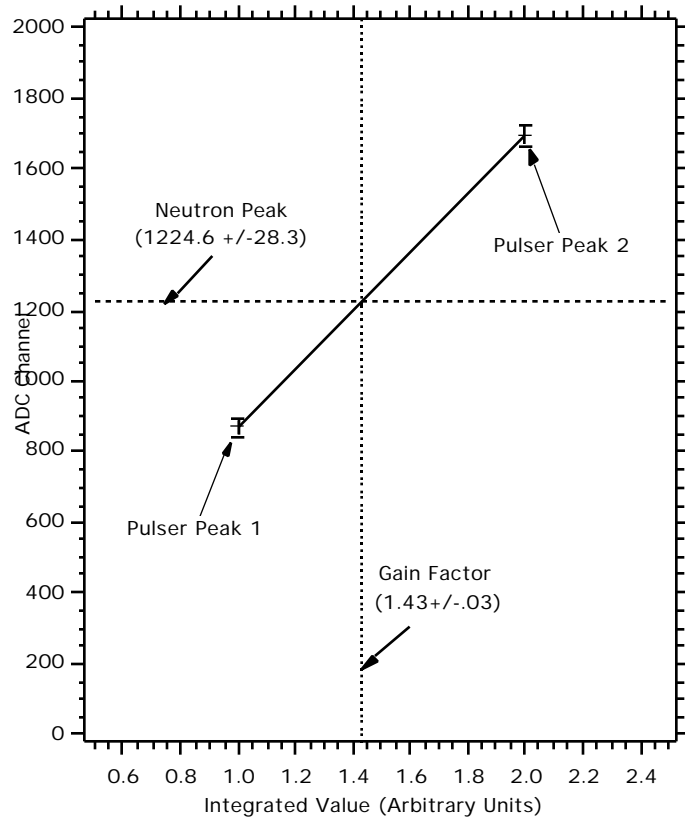
Figure 4.12: Gain factor determination for the spectrum of Figure 4.11.

Using this method, up to 8 counters can be characterized in approximately 5 minutes, independent of electronic gain. The counter gain parameters and neutron peak resolution are entered into a database to track potential deviations. Counters that demonstrate problems are returned to the University of Washington for repair.

4.5 Cool-Down Phase Tests: Assessment of Surface ^{210}Po Contamination

In Section 3.4, the surface preparation techniques for the CVD nickel was discussed. One aim of the electropolishing step is the removal of ^{210}Po, a radionuclide that decays with a 138-day half life via 5.3-MeV alpha emission. A 5.5 MeV alpha has a range of 23.1 mm in the NCD gas mix [54], while the diameter of an NCD is 50.8 mm. Most of these alphas will therefore deposit all of their energy in the gas, allowing for a separation of these events from the much less energetic p-t tracks following neutron capture. Approximately 20% of decays will result in the alpha striking the wall of the counter however [49], resulting in a distribution of events which can underlie the neutron spectrum. Since the neutron energy window represents 14% of this alpha distribution, about 2.6% of the ^{210}Po alphas are expected to contaminate the neutron window.

In the early stages of the NCD production process, tests on the nickel tubes to look for activity around the 5.3 MeV ^{210}Po alpha line showed about 30 to 40 counts $/m^2/$day. This translates to approximately 1.5 /day in the neutron window in an 11 m string. When the nickel tube supply rate exceeded the

83

counter production rate, the decision was made to store the inventory of tubes at a local mine to minimize the cosmogenic activation of ^{58}Ni and ^{60}Ni to ^{56}Co. The tubes were stored at the mine for various periods of time prior to being retrieved for counter production. Tests on the stored tubes showed activity on the order of 80,000 to 120,000 counts /m²/day. This activity would result in a background of over 4500 /day in the neutron window of an 11 m string!

Subsequent radon tests at the storage mine showed a level of 900 pCi/l. Because ^{210}Po is a daughter of ^{226}Rn the NCD nickel tubes acquired a serious burden of polonium. As a result, the electropolishing of the tubes was added to the preparation techniques in the NCD production process. In order to ascertain the amount of activity removed during construction, polished tubes are periodically placed in a specially-constructed test counter to look for high alpha rates in the 4-6 MeV window prior to being incorporated into NCDs. If the activity is deemed acceptable, counter production continues. Completed counters undergo a similar test to ascertain the final alpha activity levels. These measured values currently range between 20 and 40 counts /m²/day.

It is difficult to obtain an accurate value for this measurement at the University of Washington, however, due to hadronic interactions in the counters from cosmic rays. These events contaminate both the energy and topological phase spaces typically used for identification of surface ^{210}Po contamination. In the absence of cosmic interactions, the cool-down phase enables a statistically significant measurement to be made on an NCD string in about a day. Furthermore, the t_f vs E phase space used to identify ^{210}Po contamination can be

monitored over several ^{210}Po half-lives to verify the source and decay of the events.

Figure 4.13 shows a t_f vs E plot of a Monte Carlo simulation of the alpha spectrum from the decay of ^{210}Po on the inside surface of an NCD, and Figure 4.14 shows a plot containing 2.1 m^2 days of analyzed underground data taken on a ^{4}He-filled counter known to contain a large amount of ^{210}Po surface contamination. The spectrum of Figure 4.14 was divided into 4 regions based on the observed phase space occupied by the 5.3 MeV ^{210}Po .
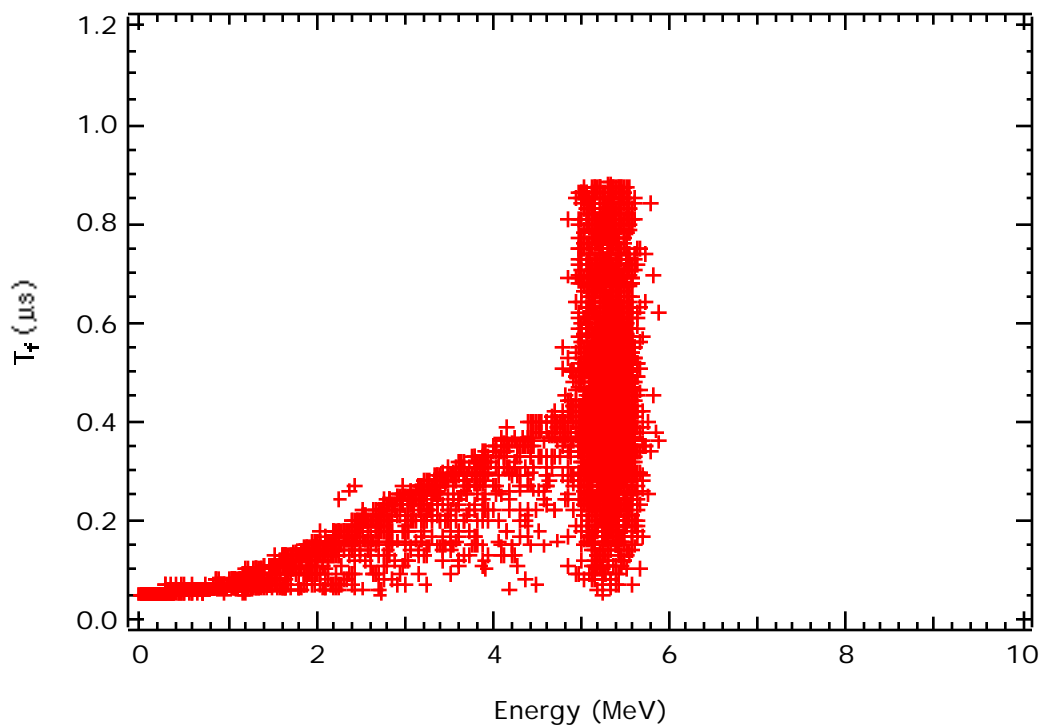
The areas of interest for surface contamination are regions 2 and 3. Region 3 contains the full energy peak from the 5.3 MeV ranging out in the gas, and Region 2 is the tail structure containing a Monte Carlo-estimated 20% of the ^{210}Po alpha events. These characteristics enable identifying the surface contamination by counts recorded in these regions.

Table 4.1 contains a summary of the recorded events in regions 2 and 3 taken during the cool-down phase. The average count rate in the ^{210}Po peak is 8.28 ± 1.17 counts /m^2/day. This equates to fewer than 0.4 background events in the neutron window per day in an 11 m string. Note that the counts in region 2 are higher than anticipated for the 20% population estimate mentioned above. There appears to be a significant fast neutron flux component which populates regions 1 and 2. This component is further addressed in Section 4.6.1. Additionally, the U and Th decay chains each contain several -emitters which contaminate these windows. An estimation of the U and Th contamination can be found in Section 4.6. Using the counts recorded in regions 2 and 3 therefore
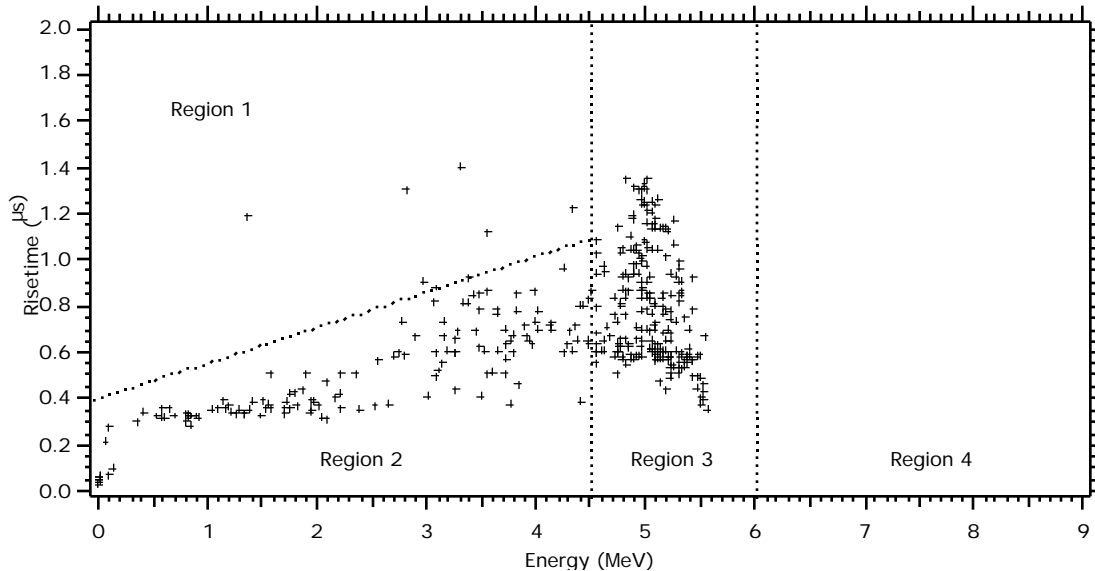
represents an upper limit on the ^{210}Po surface contamination, and is considered

acceptable.

Table 4.1: Summary of ^{210}Po rates recorded in regions 2 and 3. Units are counts m^{-2}day^{-1}. Errors in () are statistical. The m^2 days column is a measure of the run time normalized to counter surface area.

String	m^2*days	Region 2	Region 3	Summary Date
D8	3.13	10.22(1.8)	11.5(1.9)	2/18/99
N4	3.53	7.08(1.4)	8.2(1.5)	2/18/99
C1	4.2	7.62(1.3)	9.05(1.5)	2/18/99
C4	4.2	11.92(1.7)	9.28(1.5)	2/18/99
B2	7.8	5(0.8)	7.9(1.0)	2/18/99
B1	7.8	6.4(0.91)	9.1(1.1)	2/18/99
B4	7.8	5.3(0.83)	9.0(1.1)	2/18/99
B7	7.8	4.1(0.72)	9.7(1.1)	2/18/99
A1	9.05	5.4(0.77)	7.0(0.88)	2/18/99
A4	9.05	5.4(0.77)	5.8(0.8)	2/18/99
A5	9.05	8.3(0.96)	7.8(0.93)	2/18/99
A8	9.05	4.6(0.71)	5.1(0.75)	2/18/99
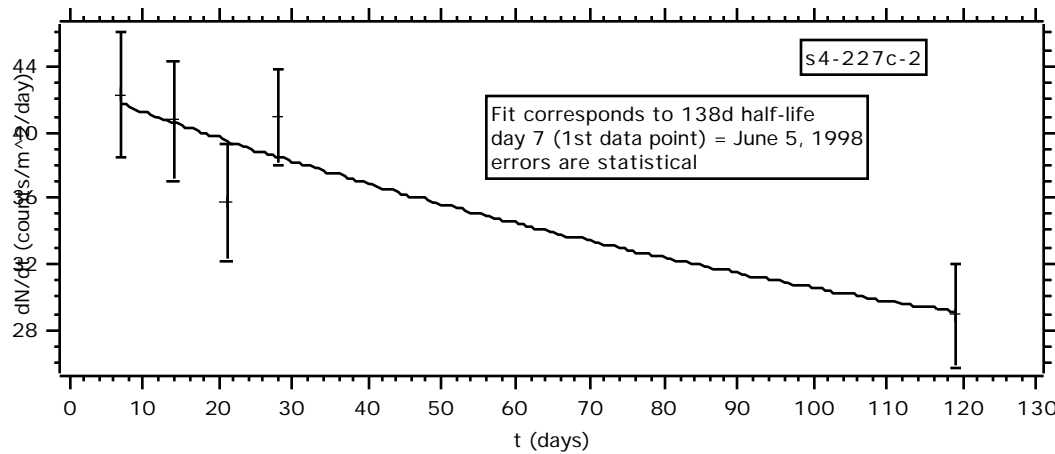
Figure 4.13: Rise time versus energy plot of a Monte Carlo simulation of the alpha particle spectrum from the decay of ^{210}Po [50].

Figure 4.14: Rise time versus energy plot of counter D1-200C-3. This counter was constructed from a tube known to be heavily contaminated with ^{210}Po.

In order to determine if the ^{210}Po activity is decaying away, counters taken underground in April 1998 were monitored for approximately one half-life. Figure 4.15 shows the counts recorded in region 3 from June to October. The data can be fit to a 138-day half life with a χ^2/DOF of 1.08. This implies that the ^{210}Po is not in equilibrium with its parent ^{210}Pb, and appears to be a good indication of the success of the surface preparation techniques.

Figure 4.15: Counts recorded in region 3 over a period of approximately one ^{210}Po half life.

There is an additional problem associated with the decay of surface ^{210}Po. Alphas with tracks that fall partially within the active region of the counter and partially within the region defined by the field tubes where there is no ion-pair multiplication can result in an abnormal ionization profile. Analysis of these events show that they potentially fall in a region of the t_f vs. E phase space referred to as the neutron background-free window. This window encloses 45% of all ^{3}He(n,p)t events, and is free of typical alpha and Compton background events due to pulse topology. The window is shown in Figure 4.16. The potential contamination of the background free window due to these "end effects" is an obvious concern considering the limited statistics from the NC measurement. The quartz field tubes were incorporated into the NCD design to minimize the potential of this occurrence, but alpha activity from the surface region near the active volume interface can lead to this effect.
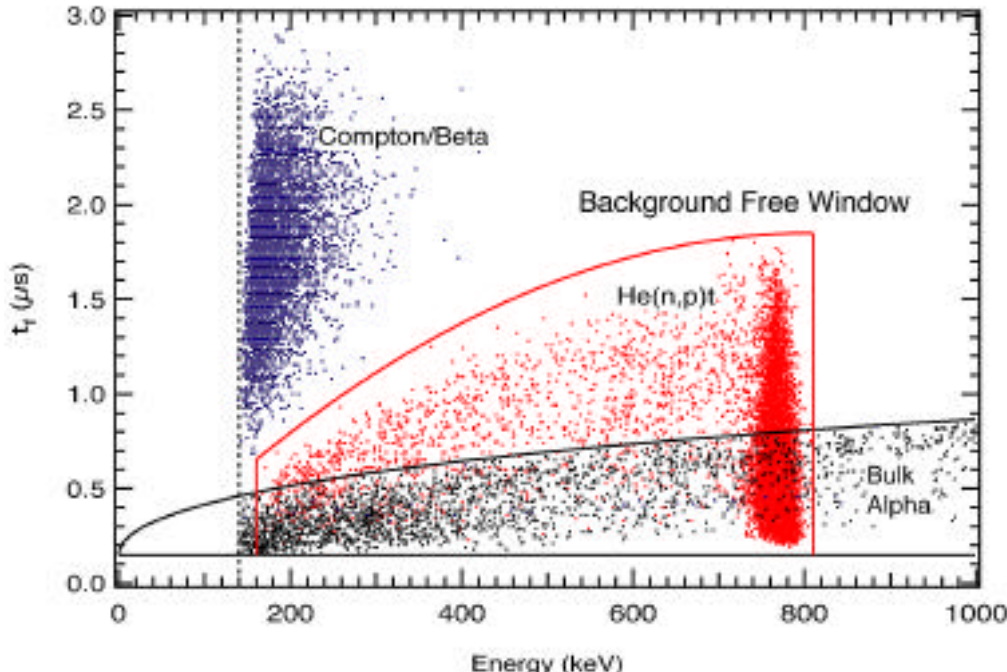
Figure 4.16: T vs. E plot of analyzed data demonstrating the "background free window" – a region of phase space occupied only by the ^{3}He(n,p)t events [51]. This region contains 45% of all neutron events, and is bounded by lower risetime (t$_f$) bulk alpha activity, and higher risetime Compton events.

A Monte Carlo simulation was written to determine the percentage of the measured surface contamination that could potentially give rise to an abnormal ionization profile as discussed above. The details of this code are described in Appendix 4. The simulation predicts that 12.2% of the alphas that deposit the full 5.3 MeV of energy in the gas will have tracks which cross the boundary defined by the end of the field tubes. The average measured surface activity for these events is 8.28 $\pm$ 1.17 counts /m^2/day, and the affected surface area is 7.4$\times$10^{-3} m^2 per end-cap. This implies 0.74$\times$10^{-3} events per end-cap per day, or 4.4 events per day for the entire array.

This exercise assumes that each of these events will somehow contaminate the background-free window. Whether or not this is indeed the case is currently undetermined. Furthermore, this surface activity is observed to be decaying away with the 138-day ^{210}Po half-life, and will have only a small contribution by the time NCDs are installed in SNO. While it is unlikely that this surface contamination will result in a serious end-effect contamination of the background-free window, ^{210}Po is not the only alpha-emitter present in the NCDs. Both the ^{238}U and ^{232}Th decay chains contain many alpha-emitters which can also give rise to end-effects via abnormal ionization profiles depending on the location of the contamination.

The extent to which the NCDs are prone to this end-effect contamination of the background-free window is not currently well characterized. Additional work is under way to both model and measure these events so as to understand the magnitude of the problem, and enable the use of event topology to recognize and remove this potential contribution off-line.

4.6 Cool-Down Phase Tests: Assessment of ^{238}U and ^{232}Th Contamination

Free neutrons liberated by the photodisintegration of deuterium represent a serious background to an accurate measurement of the NC signal in SNO. It was previously stated that ^{238}U and ^{232}Th are two radionuclei which can give rise to this background, and are present at some level in the construction materials used in the NCD array. In Table 2.2 the contamination limit on these isotopes in the D$_2$O volume was listed as 3.7×10^{-15} g/g and 4.5×10^{-14} g/g Th and U respectively.

This translates directly to a limit of 3.7 μg of Th, or 45 μg of U in the D_2O in order to keep photodisintegration neutrons to about 10% of the expected NC signal.

The NCD design goal is to limit the background budget to a few percent of the anticipated signal. In order to achieve this goal, the desired limit on the Th content would need to be less than 1 μg in the 450 kg of CVD nickel. An equivalent photodisintegration background from U contamination would limit the U content to less than about 12 μg. This equates to less than 2.0×10^{-12} grams of Th per gram of nickel (< 2ppt – parts per trillion), and less than 24 ppt of U. The remainder of the construction materials represent significantly less mass, and hence their radioactive burden is less critical. Nonetheless, samples of all materials used in the construction of the array are radioassayed by Radiochemical Neutron Activation Analysis (RNAA) or by direct gamma counting. The results of these assays indicate that the Th contamination in the nickel is 1 $\pm$ 1 ppt [55]. Measurement of the alpha activity from the U and Th chains during the cool-down phase is desired to provide an independent confirmation of the RNAA results.

Measurement of the intrinsic U and Th content is not possible at the University of Washington due to the cosmic interactions in the counters and the required counting time to achieve statistical accuracy. It is because of the counting time and the importance of this measurement that the majority of the cool-down phase is dedicated to determining the U and Th contamination. This determination involves the application of the same analytical routine used to analyze the digital waveforms for the surface polonium contamination

measurement. Now however, the [210]Po alphas must be separated from the U and Th alphas.

Figure 4.17 shows a Monte Carlo simulation of the anticipated alpha activity from the decay of U distributed in the bulk of the nickel. Comparison of this figure with Figure 4.13 shows that there are regions in the T_f vs E phase space available to the alphas from the bulk contamination that are not accessible to the surface contamination alphas. In Figure 4.14 these regions are labeled as regions 1 and 4. Recording the number of events that fall in these windows therefore enables the identification and separation of bulk alpha activity from surface activity.
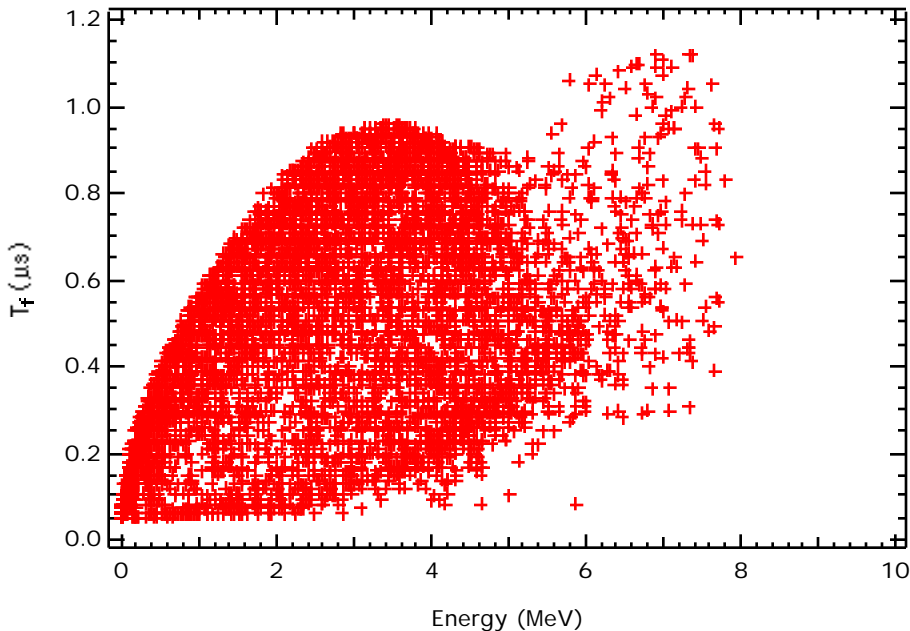
Figure 4.17: Monte Carlo simulation of the alpha activity as a result of uranium deposited uniformly in the bulk of the nickel [50].

Determination of the bulk U and Th contamination is accomplished by recording events in Regions 1 and 4, and calculating a ppt level contamination based on Monte Carlo results. These studies predict that a U contamination of 10 ppt will give rise to an observed 2.0 alpha events /m^2/day, and a Th contamination of 10 ppt will yield 0.5 alpha events/m^2/day. The detection efficiency for the U and Th alphas is the same in Region 1 (~ 50%), but drops dramatically in Region 4 due to the low number of alphas whose energies are greater than 6 MeV. In Region 4, the U alpha detection efficiency is 5%, while the Th alpha detection efficiency is 8%.

Table 4.2 contains a summary of the events recorded in Regions 1 and 4 for the counters in the cool-down phase. These counters were operated as strings to maximize the area-time product, m^2 days, of data.

Table 4.2: Summary of events recorded in regions 1 and 4 for counters in the cool-down phase. Errors in () are statistical.

String	Gas	Run Time(days)	m^2	m^2*days	Region 1	Region 4
D8	3He	4.42	0.71	3.13	0.96(0.55)	0.31(0.31)
N4	3He	2.5	1.41	3.53	0.28(0.28)	0.28(0.28)
C1	3He	4.42	0.94	4.2	1.9(0.67)	0
C4	3He	4.42	0.94	4.2	0.67(0.38)	0
B2	3He	12.1	0.86	10.4	0.86(0.28)	0
B1	3He	12.1	0.86	10.4	0.96(0.30)	0
B4	3He	12.1	0.86	10.4	1.4(0.42)	0.12(0.12)
B7	3He	12.1	0.86	10.4	0.48(0.21)	0
A1	4He	14.6	0.62	9.05	1.66(0.4)	0.33(0.19)
A4	4He	14.6	0.62	9.05	0.99(0.3)	0.33(0.19)
A5	4He	14.6	0.62	9.05	2.2(0.5)	0.11(0.11)
A8	4He	14.6	0.62	9.05	0.55(0.2)	0.11(0.11)

The average rates recorded in Regions 1 and 4 were 1.28 ± 0.12 and 0.12 $^{+0.04}_{-0.03}$ counts/m^2/day respectively. U and Th contamination levels were derived from these numbers by assuming that the observed counts were a linear combination of the U and Th decay alphas. A plot of the U ppt level contamination vs. Th ppt level contamination therefore yields a straight line describing the relationship. The data and associated errors define a band from Region 1 and a band from Region 4, with the best combined estimate occurring where these bands overlap. Figure 4.18 shows this plot.
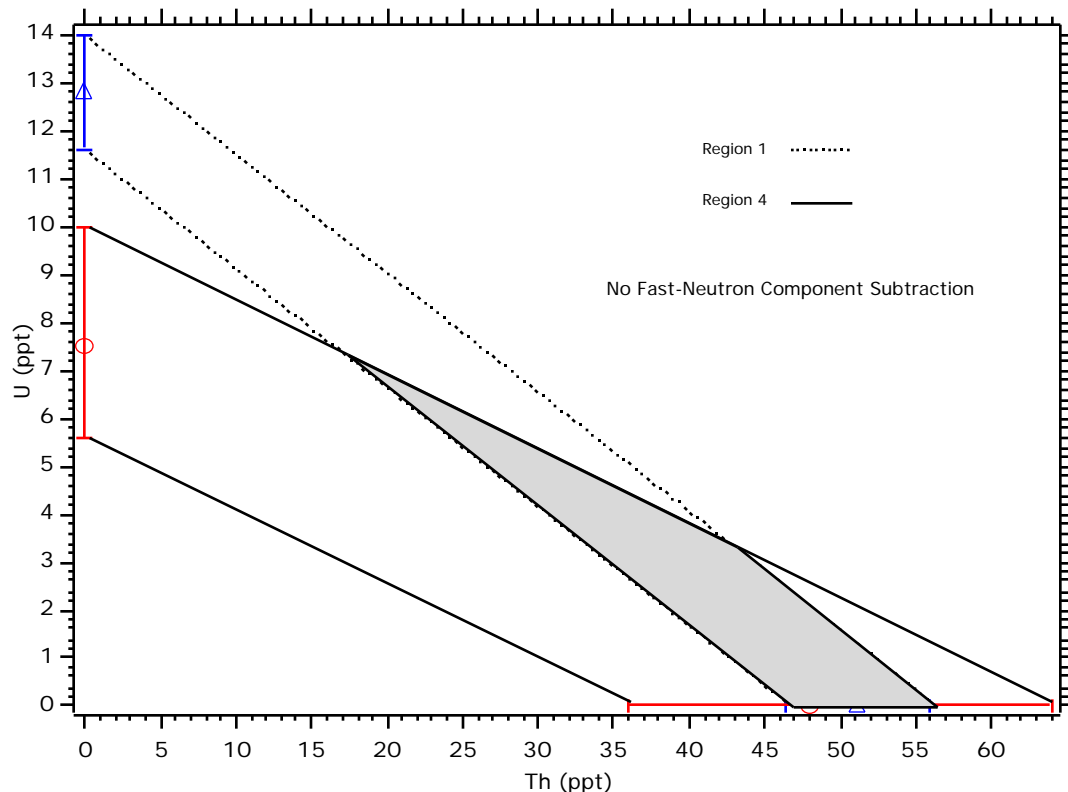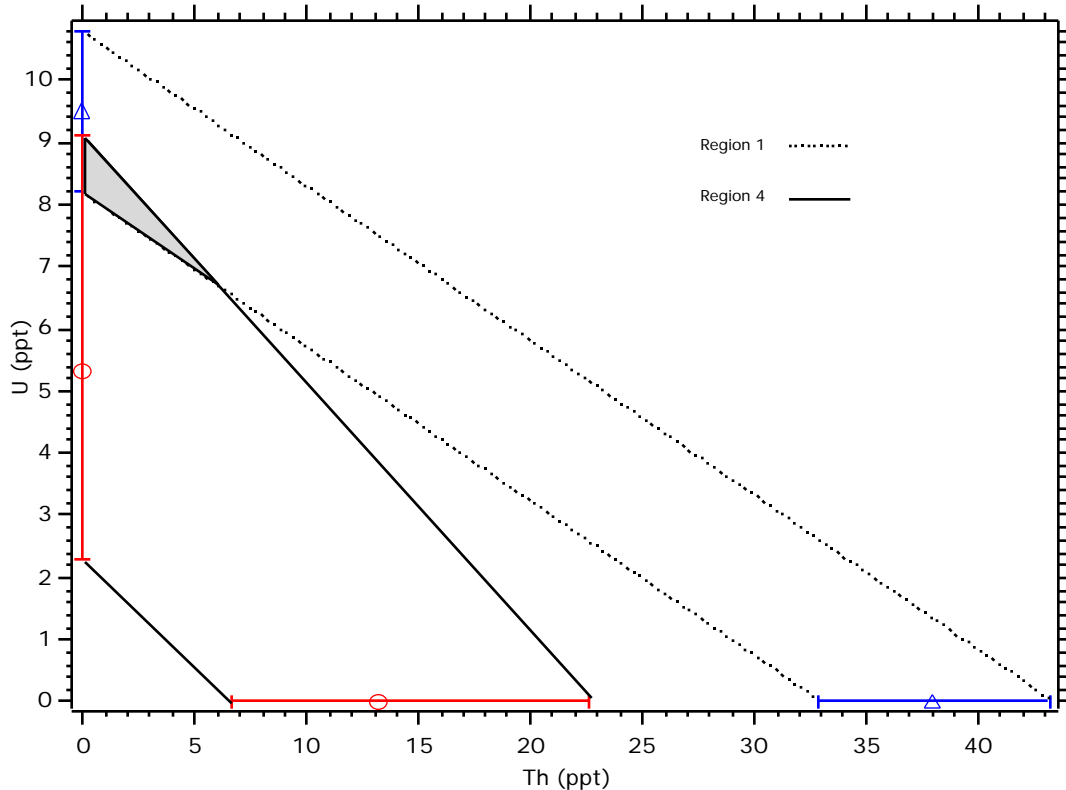
Figure 4.18: Plot of U ppt level contamination vs. Th ppt level contamination from the combined data taken in Regions 1 and 4 during the cool-down phase (Error bars correspond to the 68% CL.).

Figure 4.18 implies a best-estimate Th ppt level contamination much greater than the 1 ± 1 ppt indicated by the RNAA measurements. Strings were analyzed independently in an attempt to identify whether an individual string or set of strings was driving this measurement. The A-strings were isolated as having a known high "splotch" density - imperfections on the nickel tube of the counter body from the CVD process. These splotches may contain large amounts of aluminum as a result of mandrel degradation during tube fabrication. Aluminum tends to contain large amounts of U and Th, and thus these splotches may represent isolated pockets of contamination. Additionally, the A-strings were constructed prior to the final NCD tube surface preparation procedures, and thus may be unrepresentative of the majority of the array.

Re-analysis of the data, exempting the A-strings, yielded an average event rate of 0.95 ± 0.13 counts/m^2/day from Region 1, and $0.05 \; ^{+0.036}_{-0.025}$ counts/m^2/day from Region 4. Figure 4.19 shows a plot of the recalculated U ppt level contamination versus Th ppt level contamination. The area of overlap between the two measurement regions is now in better agreement with the results of the RNAA, but still not in very good agreement with each other.

Contamination of Regions 1 and 4 by events other than U and Th decays could result in the calculation of an artificially elevated ppt level. Additionally, if this contamination had an energy dependence, Regions 1 and 4 would contain differing levels of background to the   measurements. One possible contamination is fast neutron interactions.

95

Figure 4.19: Plot of U ppt level contamination vs. Th ppt level contamination from the combined data, excluding the A-strings, taken in Regions 1 and 4 during the cool-down phase (Error bars correspond to the 68% CL.).

4.6.1 Fast Neutron Contamination of Regions 1 and 4

Confirmation that Regions 1 and 4 can be populated by fast-neutron interactions would indicate that the above U and Th ppt level measurement represents an upper limit. Figure 4.20 shows a T_f vs. E plot for 1000 digitized events taken at the University of Washington using a moderated AmBe neutron source. The neutron capture phase space below 1 MeV is evident, as well as 2 events that fall in Region 1. Figure 4.21 is also a T_f vs E plot of the same counter operated under the same conditions using the AmBe source without any

96

moderator present. There are now many events that fall in Region 1. Both data sets were recorded in a relatively short period of time (approximately 30 minutes); cosmic interactions in the counter are therefore considered to contribute negligibly.
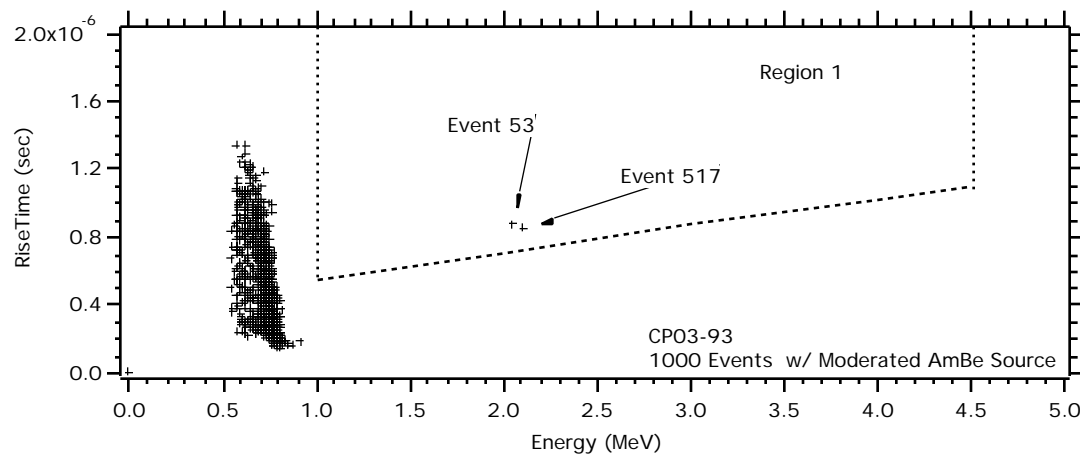
Figure 4.20: T vs E plot of 1000 events using moderated AmBe source.
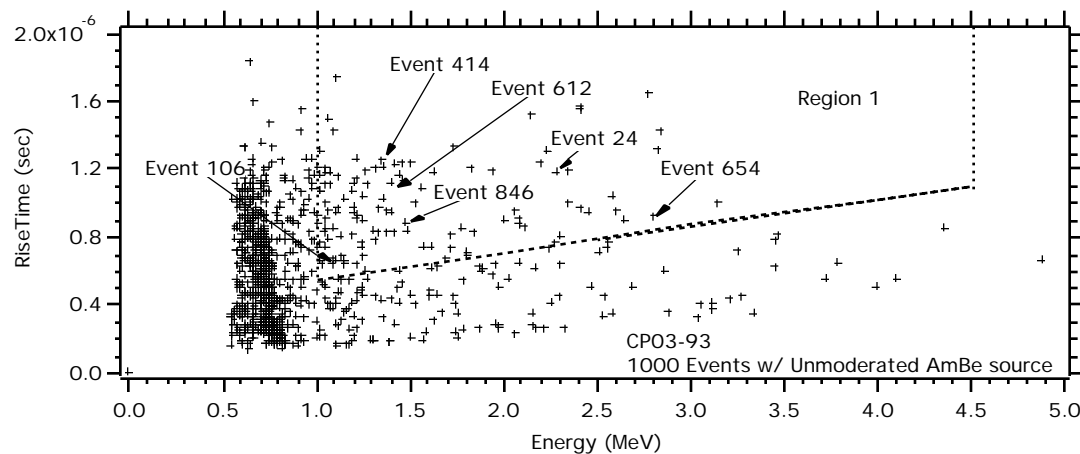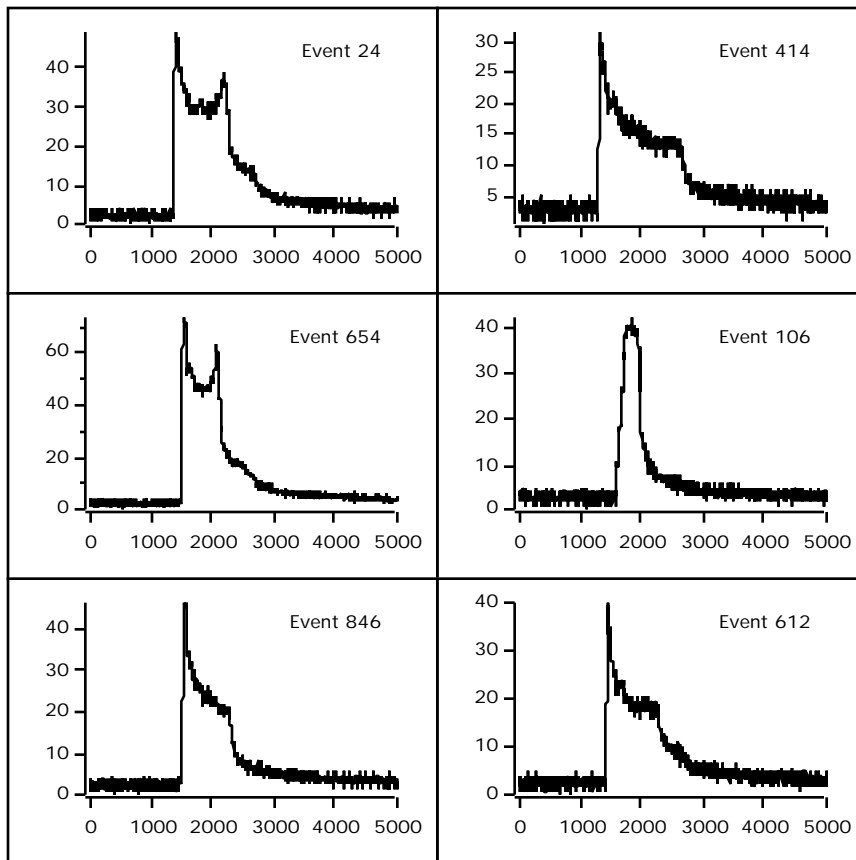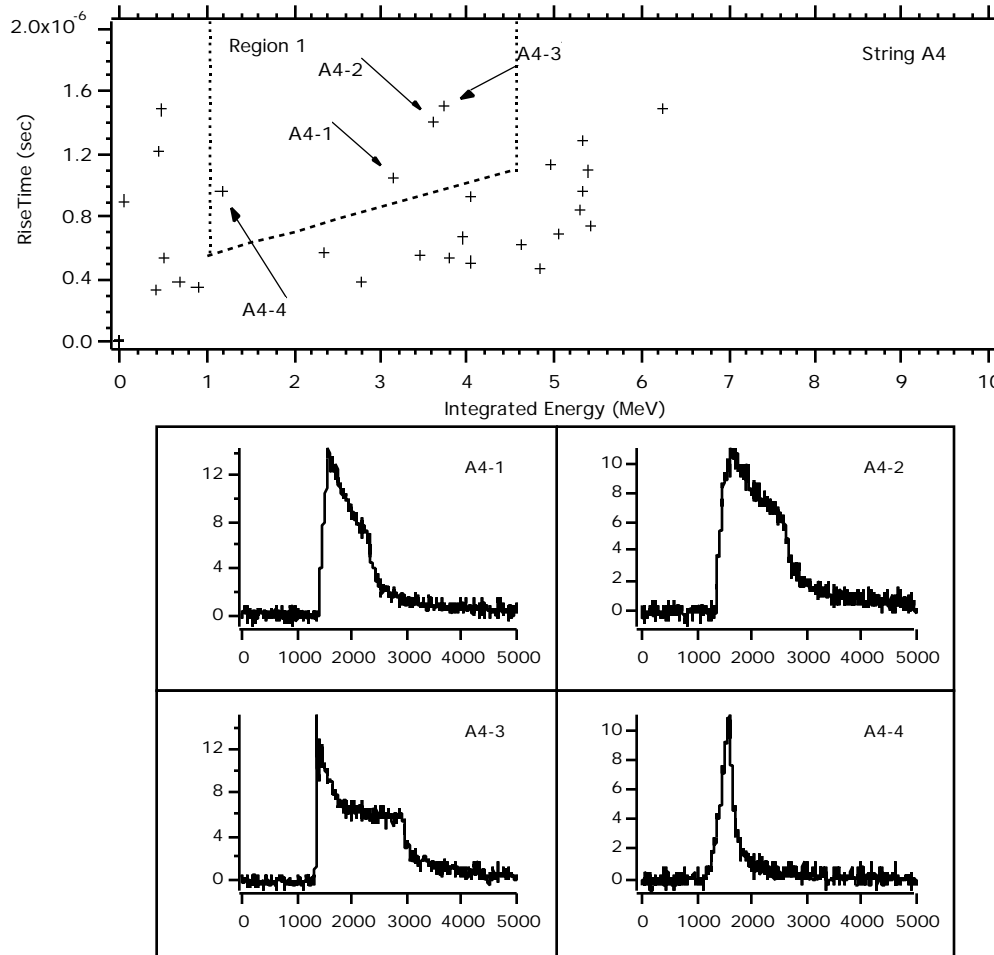
Figure 4.21: T vs E plot of 1000 events using unmoderated AmBe source.

Figure 4.22: Events which fall in region 1 of Figure 4.18.

The waveforms of the events which fall in Region 1 of Figure 4.21 are shown in Figure 4.22. For comparison, a T_f vs. E plot of data taken during the cool-down phase is shown in Figure 4.23 along with the waveforms of the events that fall in Region 1.
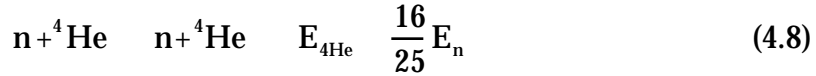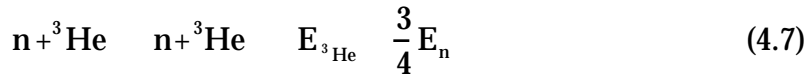
Figure 4.23: T_f vs. E plot of underground data and the associated events which populate region 1. Shown is ^{4}He counter data with a 1 MeV threshold.

There are similar topologies noticeable between the events taken underground and the events taken with the unmoderated AmBe source. Beyond noting these similarities, no reliable conclusion can be drawn that would allow for removal of fast neutron events from the underground data.

Any attempt to estimate the rate of the fast-neutron interactions requires a knowledge of the underground neutron spectrum, reaction cross sections, and the detection efficiency. For simplicity, the fast-neutron-induced reactions can be

grouped into two categories: fast-neutron reactions in the Ni counter bodies, and neutron elastic scattering with the gas in the counters (both ^{3}He:CF$_4$ and ^{4}He:CF$_4$). Calculations of the underground neutron spectrum indicate that the neutron energies extend to about 10 MeV [56]. At these energies, the neutron-induced reactions that need to be considered are listed in Equations 4.6 - 4.14.

$$n + {}^3\text{He} \rightarrow {}^3\text{H} + p + 0.764\text{MeV} \tag{4.6}$$

$$n + {}^3\text{He} \rightarrow n + {}^3\text{He} \quad E_{{}^3\text{He}} \approx \frac{3}{4}E_n \tag{4.7}$$

$$n + {}^4\text{He} \rightarrow n + {}^4\text{He} \quad E_{4\text{He}} \approx \frac{16}{25}E_n \tag{4.8}$$

$$n + {}^{58}\text{Ni} \rightarrow {}^{55}\text{Fe} + \alpha + 3.5\text{MeV} \tag{4.9}$$

$$n + {}^{60}\text{Ni} \rightarrow {}^{57}\text{Fe} + \alpha + 1.35\text{MeV} \tag{4.10}$$

$$n + {}^{61}\text{Ni} \rightarrow {}^{58}\text{Fe} + \alpha + 3.6\text{MeV} \tag{4.11}$$

$$n + {}^{62}\text{Ni} \rightarrow {}^{59}\text{Fe} + \alpha - 0.44\text{MeV} \tag{4.12}$$

$$n + {}^{58}\text{Ni} \rightarrow {}^{58}\text{Co} + p + 0.4\text{MeV} \tag{4.13}$$

$$n + {}^{60}\text{Ni} \rightarrow {}^{59}\text{Co} + p - 2.0\text{MeV} \tag{4.14}$$

The relative abundances of Ni isotopes in the CVD Ni tubes is the same as the natural isotopic abundances. The majority of the NCD counter body is therefore comprised of ^{58}Ni (68%) and ^{60}Ni (26%), and so the ^{61}Ni(n, α) and ^{62}Ni(n, α) reactions are not included in the following discussion. Figure 4.24 shows the cross sections for the remainder of the (n,p) and (n, α) reactions in the

energy range 1-10 MeV. Not included is the ^{60}Ni(n,) reaction cross section, that has a measured value of 82 mb at 15 MeV [57].
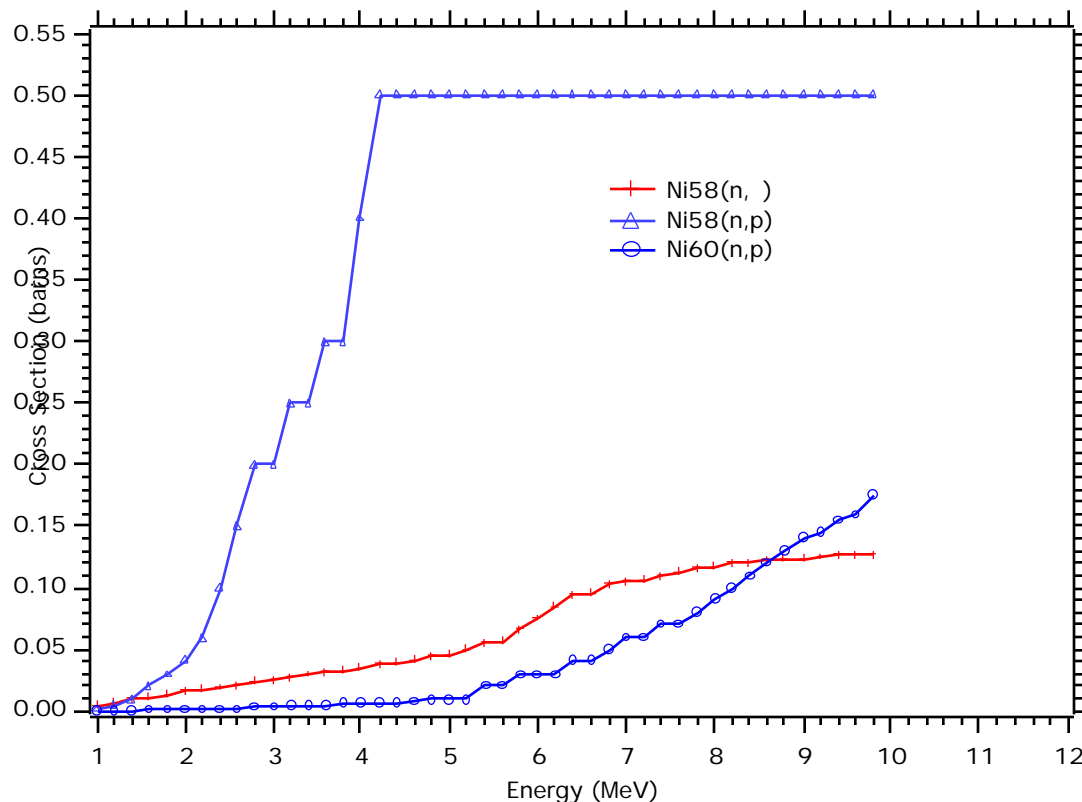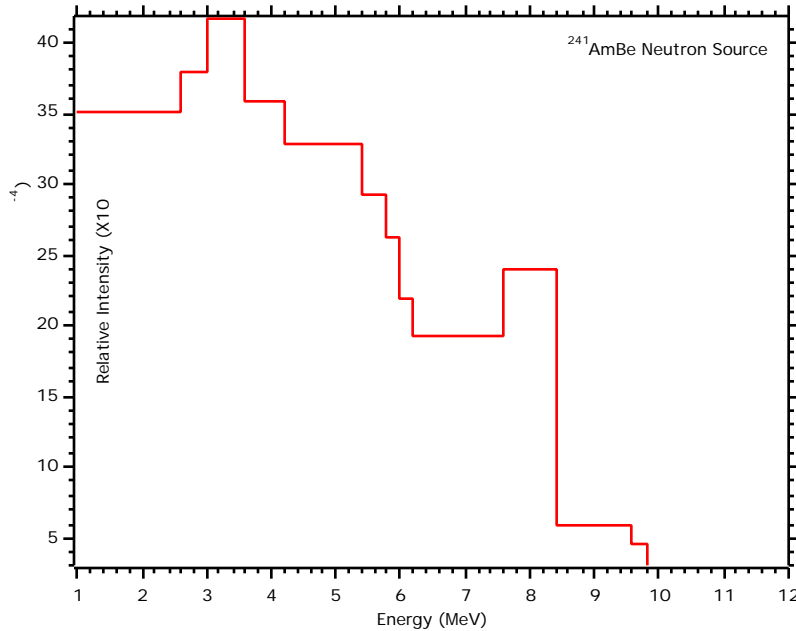
Figure 4.24: (n,p) and (n,) reaction cross sections for various isotopes of Ni [56].

An estimate of the contribution of these reactions to the events recorded in Region 1 can be made by calculating the number of interactions from a beam of neutrons incident on a nickel target. The rate of interactions is given simply by Equation 4.17.

$$ = _0 - _0 e^{-n x} \qquad _0 n x \qquad (4.17)$$

101

The number of interactions is the product of the total incident flux (Φ_0) with the target density (n), reaction cross section (σ), and counter thickness (x). An assumption must be made as to the shape of the neutron spectrum, which to first order was approximated by the neutron spectrum from an AmBe source shown in Figure 4.25. This spectrum was normalized to a total flux based on measurements of the underground thermal, epithermal, and fast neutron fluxes at Gran Sasso [58]. These measurements indicate that 15 ± 5 % of the total underground neutron flux has energy between 1 and 10 MeV. It is expected that the Gran Sasso, and any other deep-underground facility, should have similar neutron spectral shapes. The total integrated neutron flux underground at the SNO facility is calculated to be around 9000 neutrons/m^2/day [55], thus indicating 1350 ± 450 neutrons/m^2/day with energies between 1 and 10 MeV.

The estimated fast-neutron-Ni reaction rate was calculated to be approximately 1.3 events/m^2/day. The energy of these events will approximate the overall shape of the underground neutron spectrum, and will therefore preferentially populate Region 1 in the analysis. The detection efficiency for Region 1 is no greater than 50% for the observed alpha events, and should be the same for fast-neutron interaction products. This implies a contamination on order of 0.65 events/m^2/day to the Region 1 data.

Figure 4.25: Unmoderated AmBe neutron source spectrum. An estimated 77% of the flux is emitted between 1 and 10 MeV [59].

A similar estimate was performed to determine the rate of fast-neutron elastic scattering reactions. Figure 4.26 shows the total neutron cross sections (which are dominated by the neutron elastic scattering cross-section) for the components of the NCD fill-gas.

The NCD efficiency for detecting recoil nuclei was calculated for neutron energies between 1 and 10 MeV. The analytical form of this efficiency was taken from Knoll [60], and is shown in Equation 4.18.

$$\epsilon = \frac{N_{He}\sigma_{He}}{N_{He}\sigma_{He} + N_{C}\sigma_{C} + N_{F_4}\sigma_{F_4}}\left(1 - e^{-(N_{He}\sigma_{He} + N_{C}\sigma_{C} + N_{F_4}\sigma_{F_4})d}\right) \qquad (4.18)$$

This efficiency depends on the average path length (d) of the neutron in an NCD, the number density (N_{He}, N_C, N_{F_4}) of ^{3}He:CF$_4$ molecules, and the individual

neutron elastic scattering cross sections (σ_{He}, σ_C, σ_{F_4}). The integrated efficiency was calculated to be 2.8×10^{-4}.
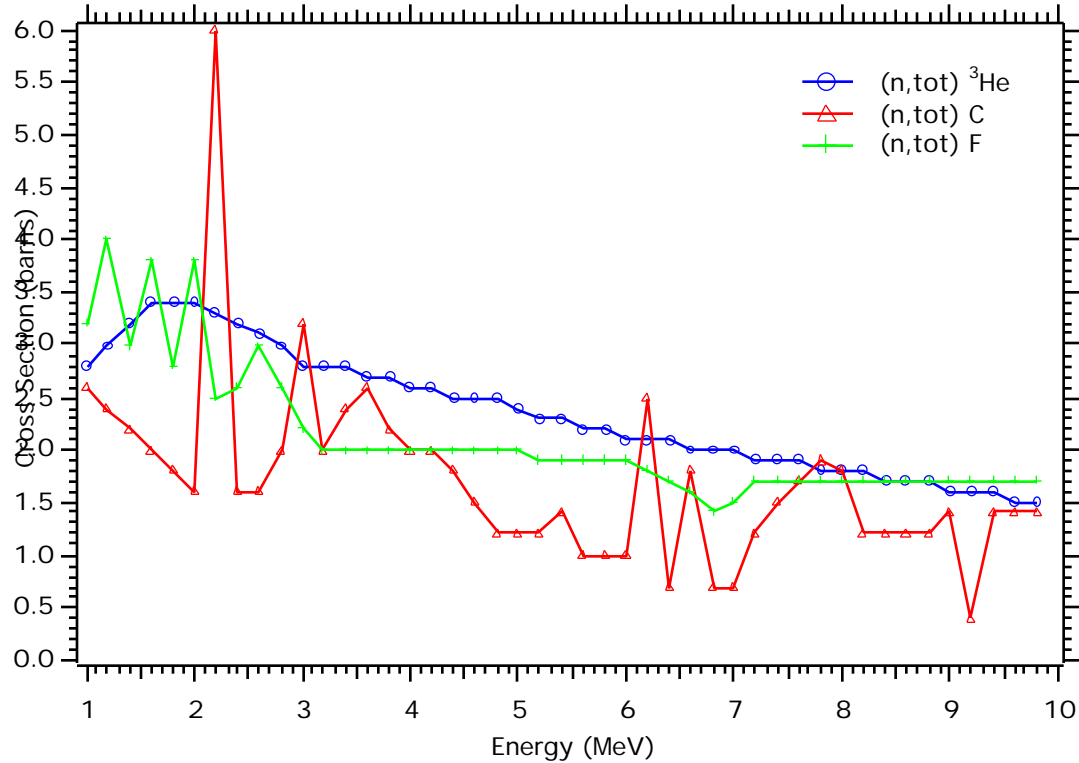
Figure 4.26: Neutron cross sections for the components of the NCD fill-gas [57].

To provide a check on the calculation, a measurement of the fast-neutron detection efficiency was performed at the University of Washington. The tests were conducted on a stainless steel prototype counter with dimensions nearly identical to an NCD, and the appropriate 85:15 ^{3}He:CF$_4$ gas fill. Taking into account the known strength of the unmoderated AmBe source used in Figure 4.18, the energy distribution of the emitted neutrons, and the solid angle

subtended by the detector, the measured detection efficiency was $(2.8 \pm 0.3) \times 10^{-4}$, which is in good agreement with the calculated value.

Applying this efficiency to the estimated fast-neutron flux of 1350 neutrons/m²/day yields 0.38 elastic scattering events/m²/day. Once again applying a 50% efficiency to estimate the contamination to Region 1, the end result is a contribution of 0.19 events/m²/day. If the two estimated contamination contributions are added, the result is 0.84 events/m²/day, or nearly 90% of the measured event rate in Region 1 (excluding A-strings).

The magnitude of the fast-neutron contribution to Regions 1 and 4 remains unmeasured, but has been shown to be non-zero. An apparent solution would be to shield the underground counters from the fast-neutron flux. This is impractical for the entire array during the cool-down phase, but the fast-neutron component could be derived by operating one string in a shielded enclosure. A Monte Carlo was written to determine the thickness of water required to supply adequate shielding. A description of this code can be found in Appendix 4. The code indicates that approximately 90% of 5 MeV neutrons will be attenuated to thermal or epithermal energies by 0.25 m of water. Operating a 5-m string surrounded by such an moderator for two weeks would enable determination of the fast-neutron flux with an estimated 50% uncertainty.

4.6.2 Assessment of ^{238}U and ^{232}Th Contamination via Coincidence Analysis

In the absence of a fast-neutron measurement, a different analysis approach was employed to better quantify the bulk U and Th contamination. This technique involved identifying specific alpha decays of both the U and Th chains via timing

information. This approach of looking for the alphas emitted by the short half-life daughters of ^{238}U and ^{232}Th should be less sensitive to a fast-neutron background by virtue of a relatively short coincidence-acceptance window.

In the ^{232}Th decay chain, there are two short-lived alpha emitting daughters (see Appendix 1): ^{220}Rn($t_{1/2}$=55.6 s, E =6.3 MeV) and ^{216}Po ($t_{1/2}$=0.15s, E =6.8 MeV). Identification of the Th chain requires observation of either of these alphas in coincidence with the ^{224}Ra alpha. The mean lifetime ( ) of a radionuclide with a $t_{1/2}$ half-life is given by Equation 4.19.

$$1/\ =\ =0.693/t_{1/2} \tag{4.19}$$

The mean lifetime for the ^{220}Rn daughter is therefore 1.5 minutes, and so the time window for the coincidence analysis was set to 2 minutes. Due to the deadtime of the digitizer, a measurement of the ^{216}Po alpha in coincidence with the ^{220}Rn alpha was not possible.

In the ^{238}U decay chain, there is only one short-lived alpha emitter: ^{218}Po ($t_{1/2}$=3.05 m, E =6.0 MeV). The choice to set an analysis window shorter than the mean lifetime of this isotope is twofold. First, the number of accidental coincidences scales with the size of the analysis window as is discussed below. Second, The previous U and Th analysis using the phase space of Regions 1 and 4 has already demonstrated that the ^{238}U contamination is acceptable. The primary goal of the coincidence analysis is an attempt to further decrease the uncertainties on the ^{232}Th measurement.

The DAQ system records the time of each trigger, thus providing a   t parameter - the time between successive events. The coincidence analysis of this data is therefore dependent on the shape of a spectrum where the number of

occurrences are plotted versus Δt in two minute bin sizes. For random events, the probability of observing an event in a window Δt after no events occurred for some time t is the product of the individual probabilities P_0 and P_1. P_0 is the probability that no events will be observed between t=0 and t=t. P_1 is the probability that an event will be observed in some window Δt, where Δt is small compared to the rate of random events. The first of these probabilities is described by the Poisson distribution shown in Equation 4.20.
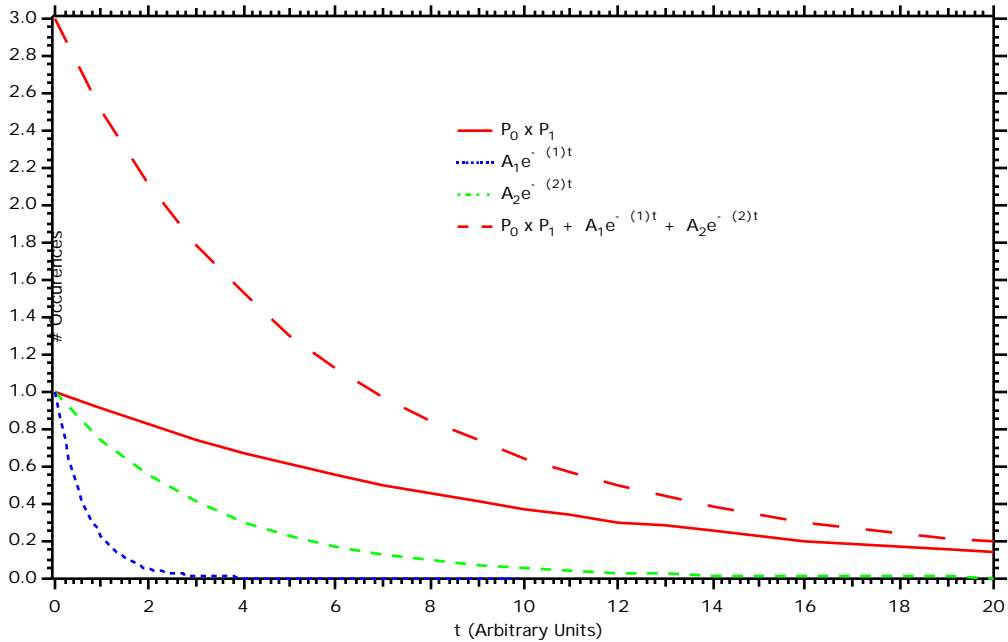
$$P(x) = \frac{(\bar{x})^x e^{-\bar{x}}}{x!} \qquad (4.20)$$

The random events are characterized by an overall rate r. The average value is therefore given by the rate time product $\bar{x} = rt$. The second probability is simply the product of the rate with the time interval ($r\Delta t$). The probabilities P_0 and P_1 are shown in Equation 4.21.

$$P_0 = \frac{(rt)^0 e^{-rt}}{0!}$$
$$P_1 = r\Delta t \qquad (4.21)$$
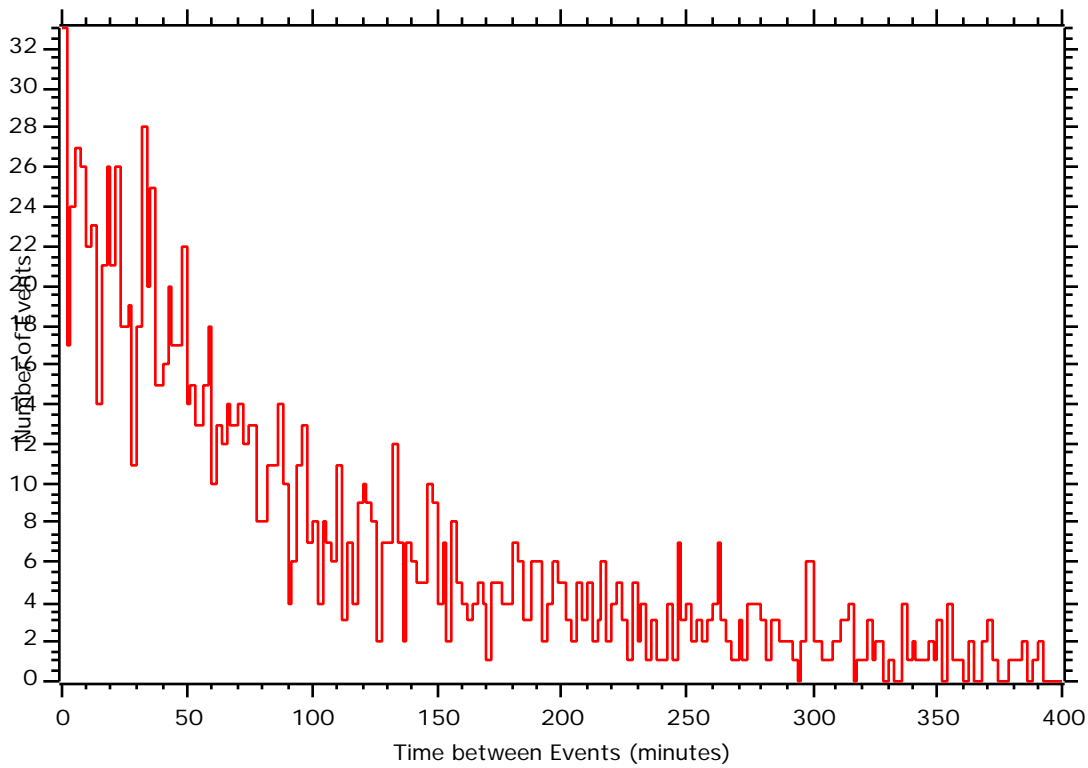
In addition to this distribution describing random events, there will be contributions associated with the U and Th decay alphas. These distributions are given by the exponential radioactive decay law. The total combined distribution is given in Equation 4.22 and shown in Figure 4.27.

$$P(t) = r\Delta t\, e^{-rt} + A_1 e^{-\lambda_1 t} + A_2 e^{-\lambda_2 t} \qquad (4.22)$$

Figure 4.27: Anticipated spectral shape from coincidence analysis.

The total combined 92.9 m^2 days of data was analyzed for timing information. Figure 4.28 shows a histogram of this analysis. There were three different analysis techniques applied in an attempt to extract the U and Th contamination levels. The first extraction technique performed a fit to the combined data of the form of Equation 4.21. The best fit coefficients corresponding to the U and Th half-lives were used to estimate a ppt level contamination. The fit to the data is shown in Figure 4.29.

Figure 4.28: Combined 92.9 m^2 days of data plotted as number of occurrences versus time between events.
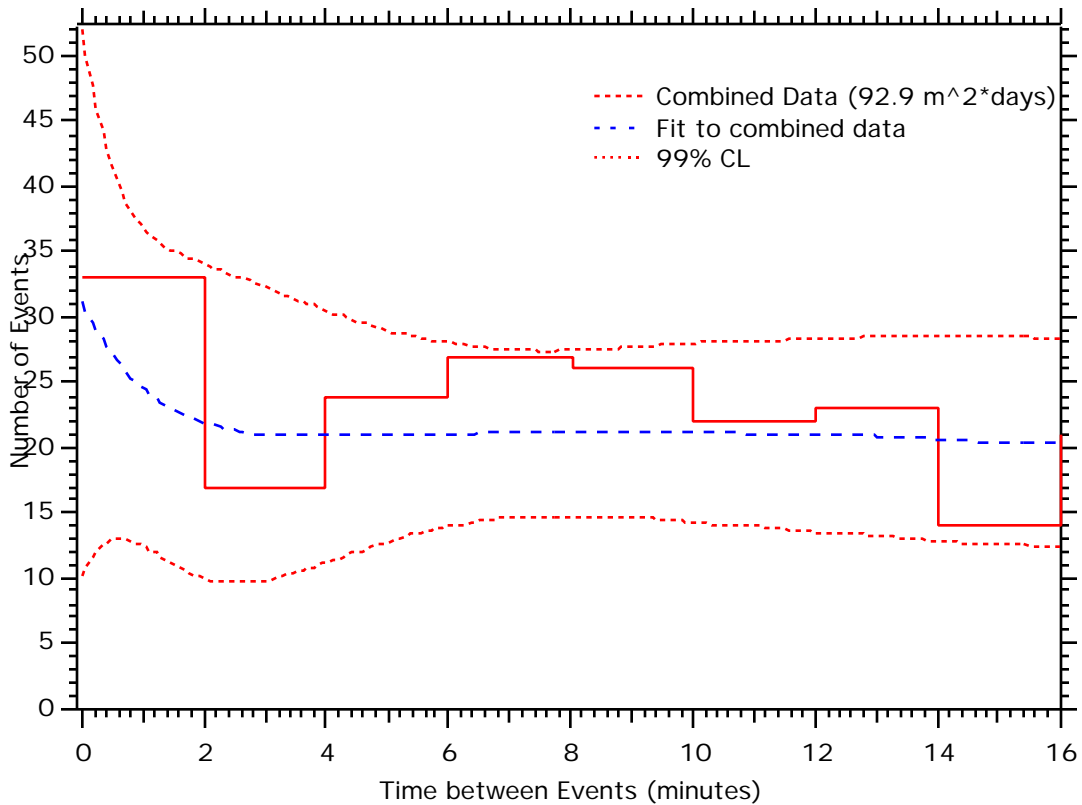
Figure 4.29: Analytical fit of the combined data to the form of Equation 4.22.

The uncertainties on the U and Th fitting parameters were large, resulting in a Th estimate of 96 ± 78 ppt. These uncertainties were largely driven by the limited counting statistics.

The second extraction technique applied to this data was to calculate the rate of accidental coincidences in the first 2-minute bin, and subtract this component, thus leaving only the contributions from the U and Th chains. The number of accidental coincidences was determined from the distribution P_1 that was given above in Equation 4.21. Now, the rate is the average observed event rate, and t is 2 minutes. Since the event rate in general varies from string to

string due to the different Po contamination rates, accidental coincidences were calculated for each string individually.

It was once again noted that the A-strings demonstrated a higher rate in comparison to the other strings. For the reasons mentioned previously, they were not included in the remainder of the analysis. The extraction efficiency using this technique is different for U and Th due to the different probabilities of observing these decays in a 2-minute window. The probability of observing the Th chain is further enhanced in relation to the U chain by the presence of ^{216}Po. If after observing the ^{224}Ra alpha decay, the ^{220}Rn is not observed, there is still a probability of seeing the ^{216}Po alpha. The method of applying the efficiencies and converting the number of events recorded in the first 2-minute bin to a ppt level contamination is outlined in Figure 4.30.

The results of this analysis are shown in Figure 4.31. The calculated values and uncertainties are now in much better agreement with the results of the Regions 1 and 4 analysis.

Converting # of Events Recorded into Th ppt level

Events Recorded = Total Events x 1/6 x 1/2 x 3/4

Probability of seeing the short-lived Th decay in a 2-minute window

Probability of seeing ^{224}Ra or ^{216}Po

Probability of seeing ^{224}Ra

Th contamination (ppt) = Total Events * 10 ppt ∕ 0.5 Event

Converting # of Events Recorded into U ppt level

Events Recorded = Total Events x 1/8 x 1/4 x 0.36

Probability of seeing the short-lived U decay in a 2-minute window

Probability of seeing ^{218}Po

Probability of seeing ^{222}Rn

U contamination (ppt) = Total Events * 10 ppt ∕ 2.0 Event

Figure 4.30: Coincidence analysis detection efficiencies and ppt conversion formulas.
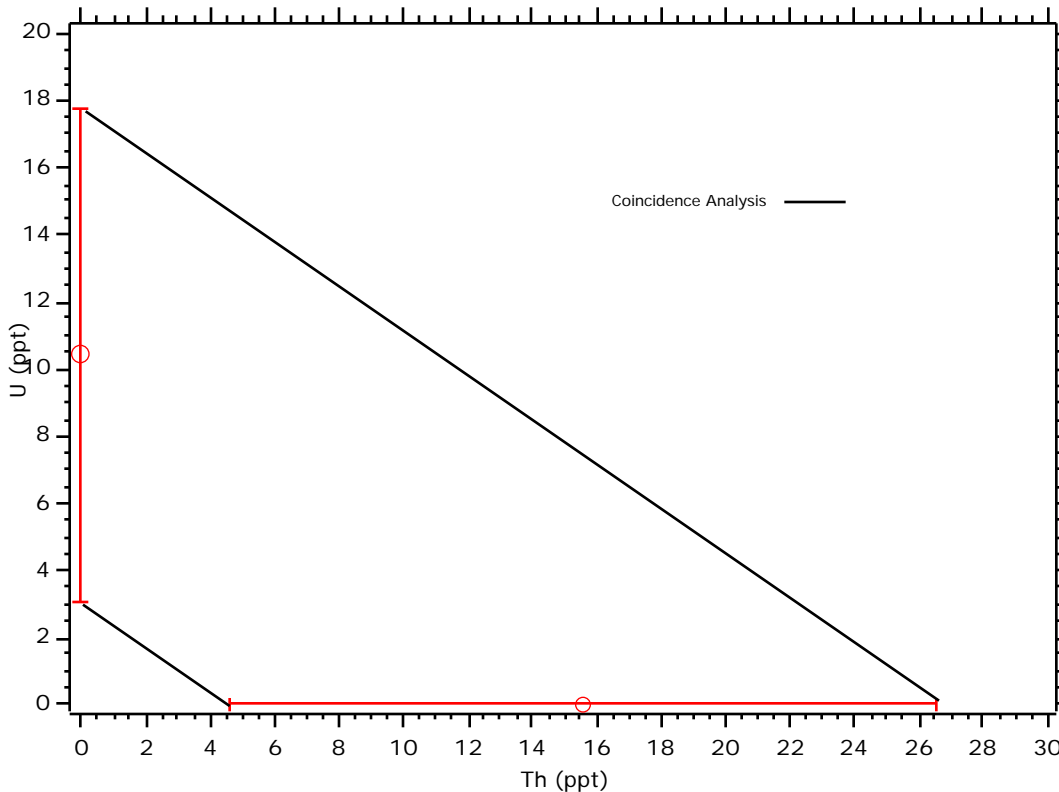
Figure 4.31: U vs. Th ppt plot for the second analysis cut of the coincidence data (Error bars correspond to the 68% CL.).

The final analysis of the data involved an additional constraint on the 2-minute coincidence events. This cut required at least one of the coincidence events to fall in Region 1. The efficiency for such events is now only 50% of the previous analysis method, but has the advantage of discriminating against accidental coincidences from the ^{210}Po decays which populate Regions 2 and 3 exclusively. Accidentals are now calculated from Equation 4.23. This number is simply the previous accidentals attenuated by a factor corresponding to the total number of events (r * run time) multiplied by the probability of a short coincidence event falling in Region 1 ($2\tau_{Region\ 1}$).

$$\text{Accidentals} = r\ t * (2\tau_{Region1}) * r * run\ time \qquad (4.23)$$

113

Analysis of the data (once again excluding the A-strings), yielded 2 events and a calculated background of 3.03 events.

In dealing with the Poisson statistics of low counting situations with known backgrounds, the unified approach of Reference 61 between classical and Bayesian statistics was taken. For a signal of 2 and a background of 3, the prescribed measurement is consistent with a null result, and an upper limit of 1.41 events at the 68% CL. Converting to U and Th ppt equivalents, the results of this analysis are listed in Equation 4.24.

$$U = 0 \text{ppt} (\quad 29.3 \text{ppt@68\%CL})$$
$$Th = 0 \text{ppt} (\quad 21.1 \text{ppt@68\%CL})$$

(4.24)

This result was plotted with the results of the analysis from Regions 1 and 4, and is shown in Figure 4.32. The hatched area demonstrates the region of overlap for all three measurements. The different analyses and associated uncertainties are independent enough to calculate a ^{2}-minimized best fit to the three measurements. The reduced ^{2} best-fit contour is shown in Figure 4.33 along with the 90% CL contour[3]. The shaded region corresponds to a shallow minimum, and represents the resolving limit of the best-fit minimum value for the calculation.

---

[3] The 68% CL was determined following the method cited in Reference 62, and corresponds to the ellipse that contains 68% of the normally distributed data.
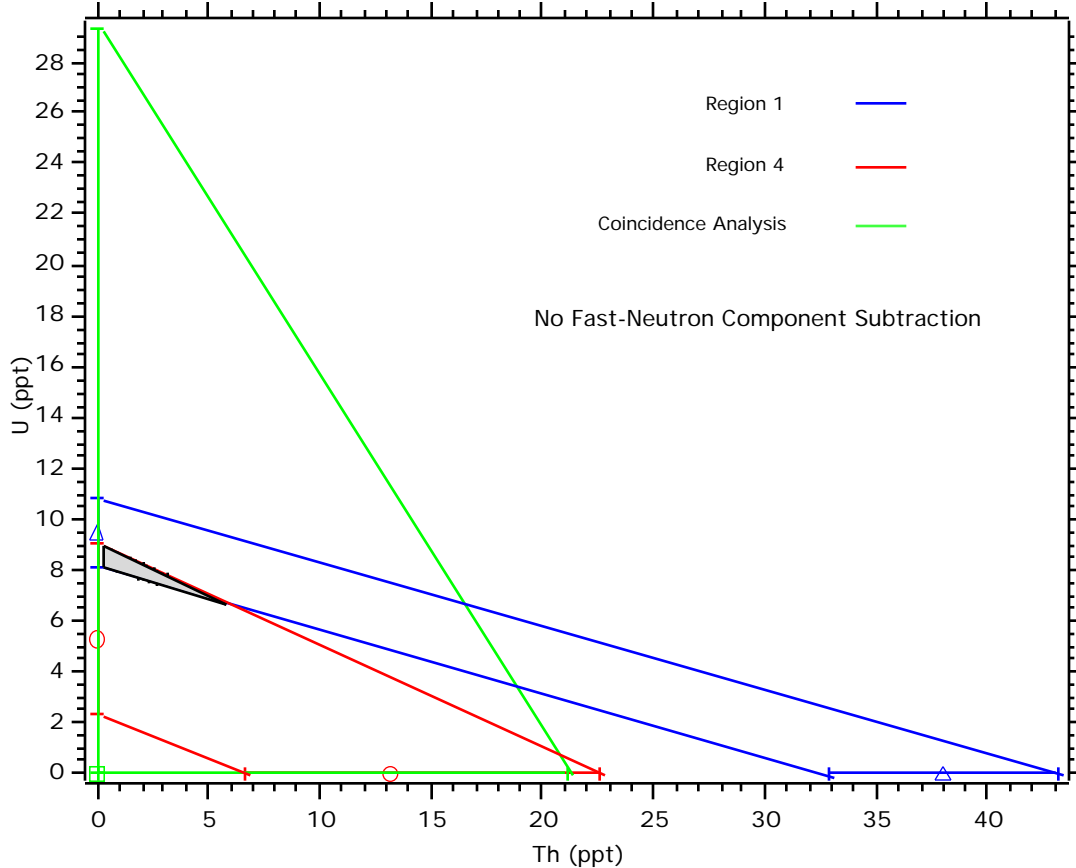
Figure 4.32: Combined results of the three U and Th contamination measurements (Error bars correspond to the 68% CL.).
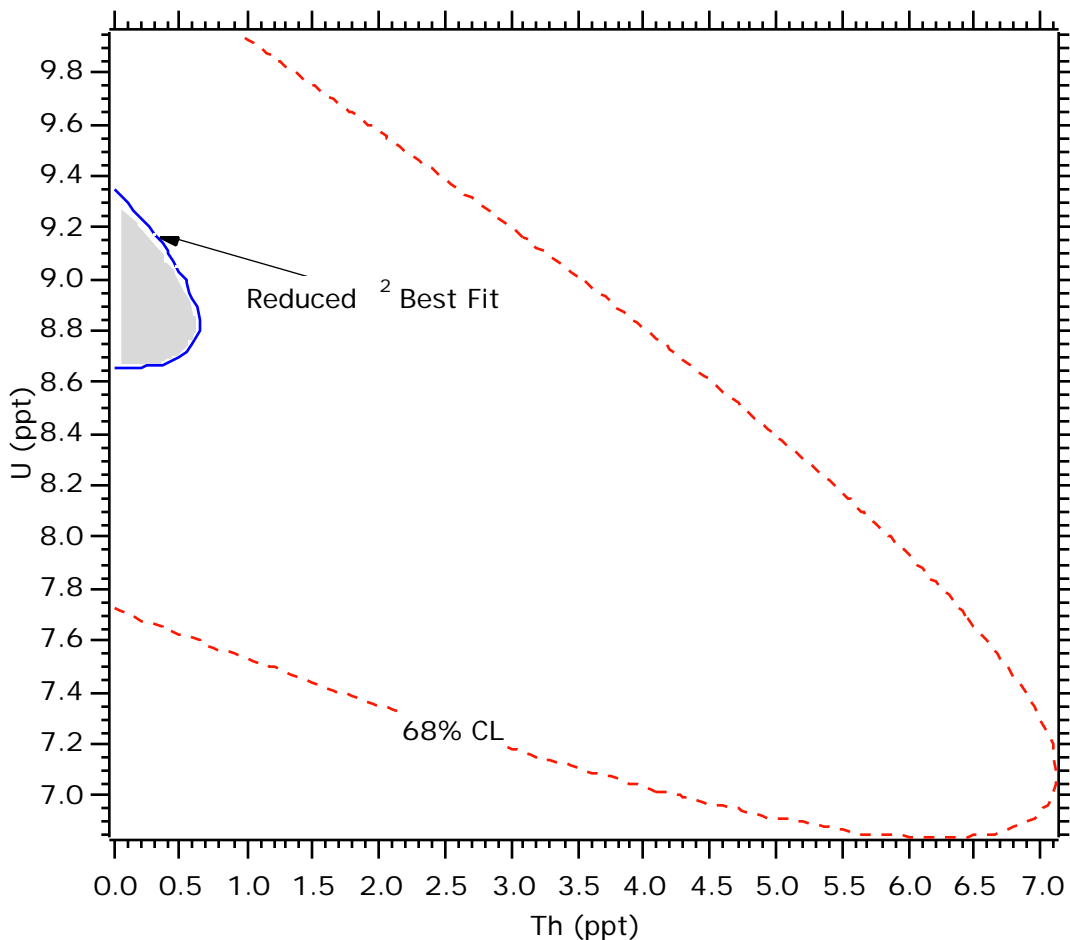
Figure 4.33: Reduced χ^2 best fit contour.

It should be noted that the best-fit χ^2/DOF was 1.4. This (lack of) goodness-of-fit is driven by the relatively small region of agreement in Figure 4.32. The fast-neutron contamination of Region 1 has the effect of shifting this measurement band upwards on the U vs Th ppt plots, thus effectively making the agreement with the other two measurements smaller. Removal of the fast-neutron component would result in an improved goodness-of-fit value as result of a larger region of measurement overlap (also implying a potentially larger Th

116

ppt value). If the estimated fast-neutron contamination from Section 4.6.2 is subtracted from the Region 1 measurement, the best-fit χ^2/DOF becomes unrealistically small. This may be attributed to the large uncertainties associated with the limited counting statistics, or the assumption that the three measurements are independent. In fact, two of the measurements rely on the same data, and only the data reduction methods are independent – hence, there may exist a correlated uncertainty.

The combined best fit value of the U and Th contamination shown in Figure 4.33 is consistent with the desired goal of a U level less than 24 ppt, and a Th level less than 2 ppt.

4.7 Cool-Down Phase Tests: Underground Neutron Flux Measurements

The primary source of underground neutrons come from (α,n) reactions on the aluminum, silicon, and sodium found in the norite rock [56]. The alphas are predominantly the result of the ^{238}U and ^{232}Th decay chains (see Appendix 1). A smaller (~10%) contribution of neutrons come from the spontaneous fission of ^{238}U. Through multiple scattering in the rock, most of the neutrons become thermalized, resulting in a moderated spectrum similar in shape to a moderated nuclear reactor spectrum. Integration of the calculated underground neutron spectrum at SNO indicates a total flux of approximately 9000 $m^{-2}d^{-1}$.

Typical underground neutron flux measurements [58, 63, 64] employ large BF_3 or ^{3}He detectors with varying degrees of moderator to ascertain the energy dependence on the flux. These measurements require long counting

periods owing to physical limitations on the size of the detectors, and the relatively low rates of a few hundred to a few thousand neutrons m^{-2}d^{-1}. The cool-down phase is well suited for this type of measurement as there are currently 115 m of counters underground (18.35 m^2), and several months of counting time available.

Measurement of the thermal neutron flux utilized both digitized and ADC data techniques. Figure 4.34 shows a typical energy histogram of this measurement. At the low end of the spectrum, a combination of the noise level of the system and Compton scattering inside the detector can be seen. The Compton events are a result of U and Th in the rock wall giving rise to gammas which produce recoil electrons in the NCDs. In general, a single electron deposits very little energy in the gas, and thus the Compton scattering component tails off by 300 keV. It was shown in Figure 3.3 that the neutron spectrum extends from 191 keV up to about 800 keV. In the region between 191 and 300 keV, these Compton electrons dominate the spectrum. Therefore, in order to determine the thermal neutron flux, the Compton component must first be removed, or an estimate of the underlying number of neutron events determined.
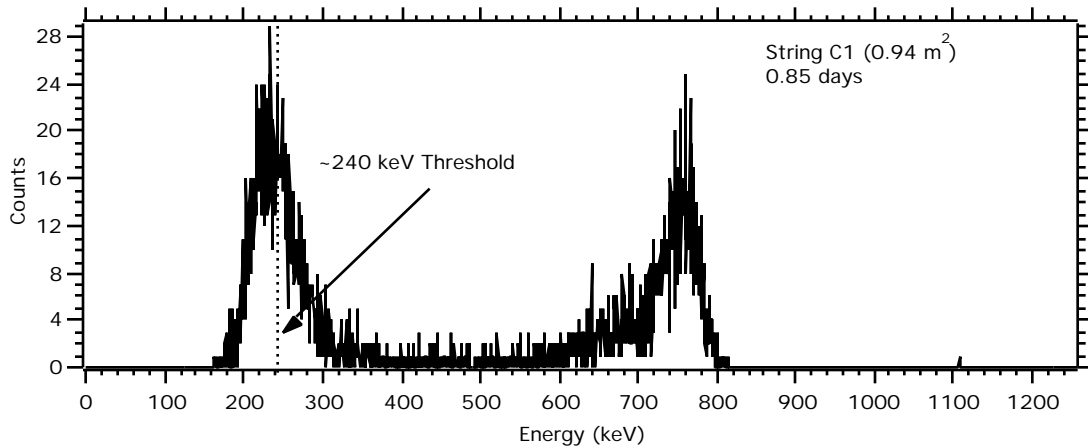
Figure 4.34: Underground neutron spectrum.

Initially, a background subtraction method was tested by using spectra obtained from the ^{4}He counters. Obtaining the flux through spectral subtraction requires a relative energy calibration between the ^{3}He and the ^{4}He proportional counters. This calibration is initially accomplished after production at the University of Washington using an ^{241}Am source. The 59.54 keV gamma interacts with a k-shell electron of a Ni atom to produce a 51.21 keV photoelectron. Because this interaction can occur anywhere in the bulk of the Ni, the electron spectrum is a continuum up to the 51.21 keV edge. It is this edge which is used to calibrate the counters. Measurement of the k-shell edge is not possible underground however due to the high gamma flux. Therefore, data taken to ascertain surface ^{210}Po contamination was used underground to cross calibrate the ^{3}He and ^{4}He counters (The details of the ^{210}Po measurement can be found in Section 4.5). The limited statistics of the 5.3 MeV alphas proved to be exceedingly inaccurate at providing an energy calibration of the counters in the region of a

119

few hundred keV. As a result, subtraction of the steeply-sloped Compton spectrum was not possible.

A second attempted method for removing the Compton component utilized the topology of events for separation of electrons from neutrons. It has been shown that by plotting the rise time versus energy (T vs E plot) of proportional counter events, some particle separation is possible. In the specific case of neutrons and gamma-induced electron events, total separation can be achieved [51]. Despite the ability to identify and subtract the Compton events off-line, it became impractical to digitize thousands or even hundreds of these events due to dead-time considerations. As a result, the threshold for the thermal neutron flux measurement from digitized data was set between 300 and 400 keV, resulting in the loss of some neutron events. In order to determine how many neutron events were not recorded, a statistical estimate was applied.

Studies indicate that at a gas gain of 100 (1835 V NCD operating voltage), 80% of all neutron events will fall between 600 and 900 keV [51]. To verify this number, approximately 3400 neutron events were digitized at the University of Washington with a threshold of 180 keV and an operational voltage of 1835 V. The events were analyzed using UW_Analyst, and binned according to 3 energy regions within the window populated by neutron events. This data set is shown as a scatter plot of rise time versus energy in Figure 4.35. In region 3 (600 – 900 keV), 78.7 ± 2.0% of the neutron events were recorded, agreeing with the Monte Carlo estimate within the statistical errors.

The thermal neutron flux can then be estimated by applying a correction to the number of observed counts which fall in region 3. The correction used is

the UW measurement of region 3's population density (78.7 $\pm$ 2.0% of the entire neutron window). The flux is then given by the corrected number of events normalized to counting time and counter surface area.
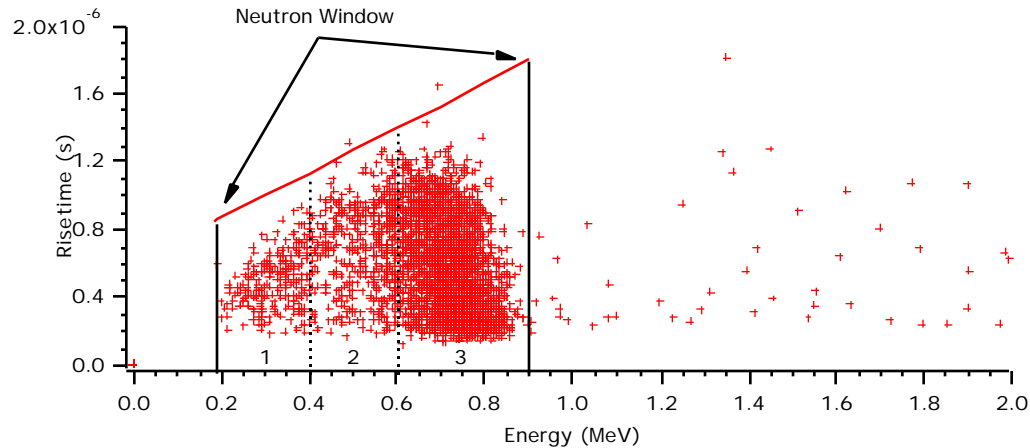
Figure 4.35: Rise time versus energy plot of digitized neutron events recorded at the University of Washington. Higher energy events are cosmic ray interactions in the counter, and do not contribute significantly to the neutron window.

In Figure 4.36, the results of the analysis of run I_DIG_UG_02_17_99_001 are displayed in the typical T vs E plot segmented into the three neutron energy windows. Table 4.3 contains the number of events observed in each region.
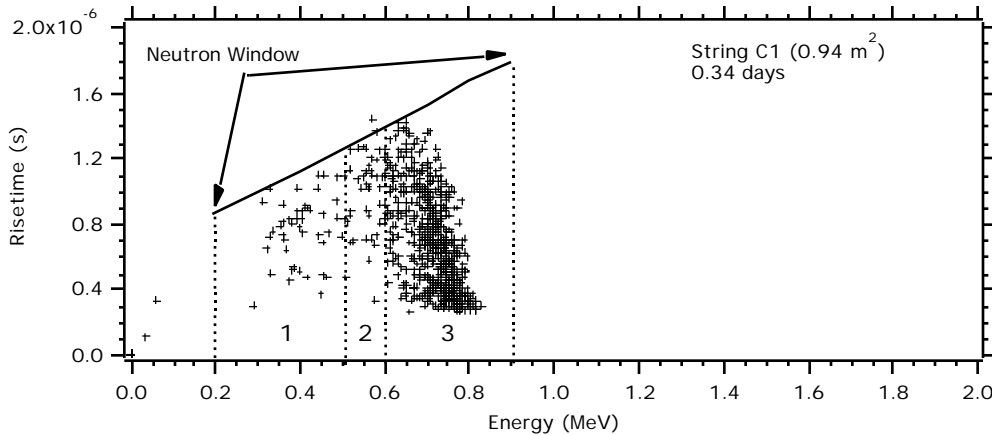
Figure 4.36: Rise time versus energy plot of I_DIG_UG_02_17_99_001

Table 4.3: Tabulated events for I_DIG_UG_02_17_99_001

Point	Neutron	region1	region2	region3
0	761	33	56	672

Estimation of the total number of neutron events is given by Equation 4.6.

$$\text{TotalCounts} = (672 \pm 25.9)/(0.787 \pm 0.02)$$
$$= 853.9 \pm 32.9(\text{stat.}) \pm 17.0(\text{syst.})$$

(4.6)

Normalized to a run time of **8 hours and 5 minutes, and a counter length of 6 m,** the estimated flux is **2671 ± 102.9(stat.) ± 53.2(syst.) neutrons** $/\text{m}^2/\text{day}$.

A check on the analysis technique used for this measurement was performed by calculating the flux from the corresponding ADC data. Once again, only the observed counts between 600 and 900 keV (region 3) were used - no background subtraction was performed on this region. The ADC spectrum and integrated number of counts for I_ADC_UG_02_17_99_001 (ADC data of Figure 4.24) is shown in Figure 4.25. The flux calculated from this data is 2858.6 ±

122

106.3(stat.) ± 72.6(syst.) neutrons /m^2/day. Comparison of the ADC derived flux to the digitzation derived flux is for purposes of analysis checks only, and does not constitute a separate measurement.
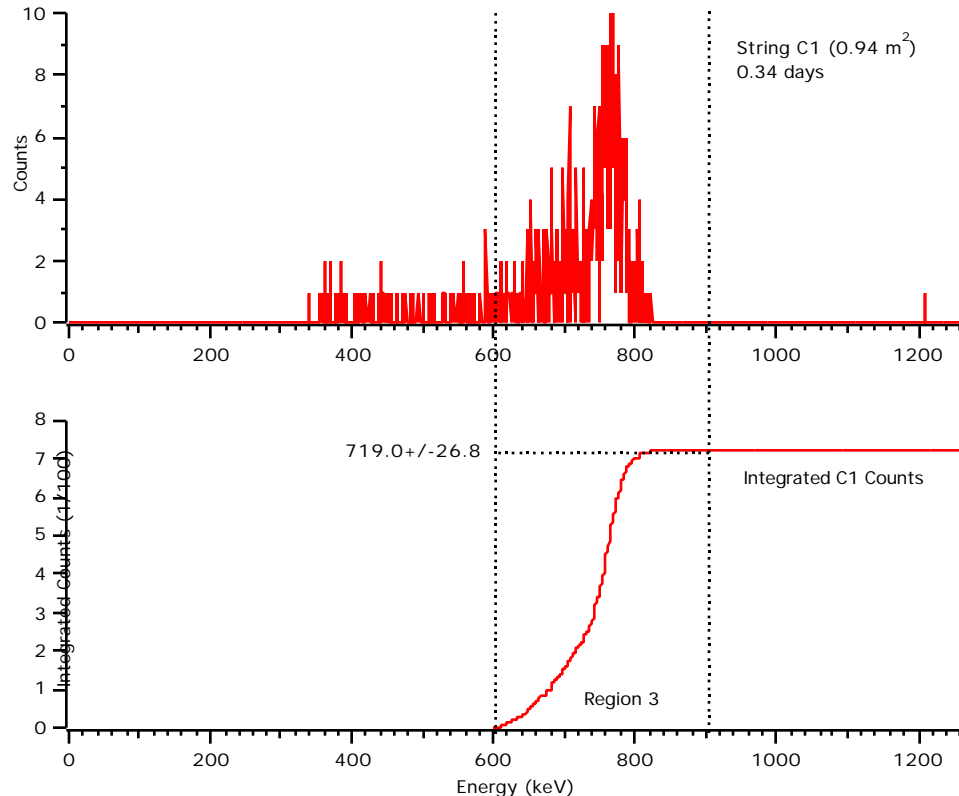
Figure 4.37: ADC histogram and integrated count rate of I_ADC_UG_02_17_99_001.
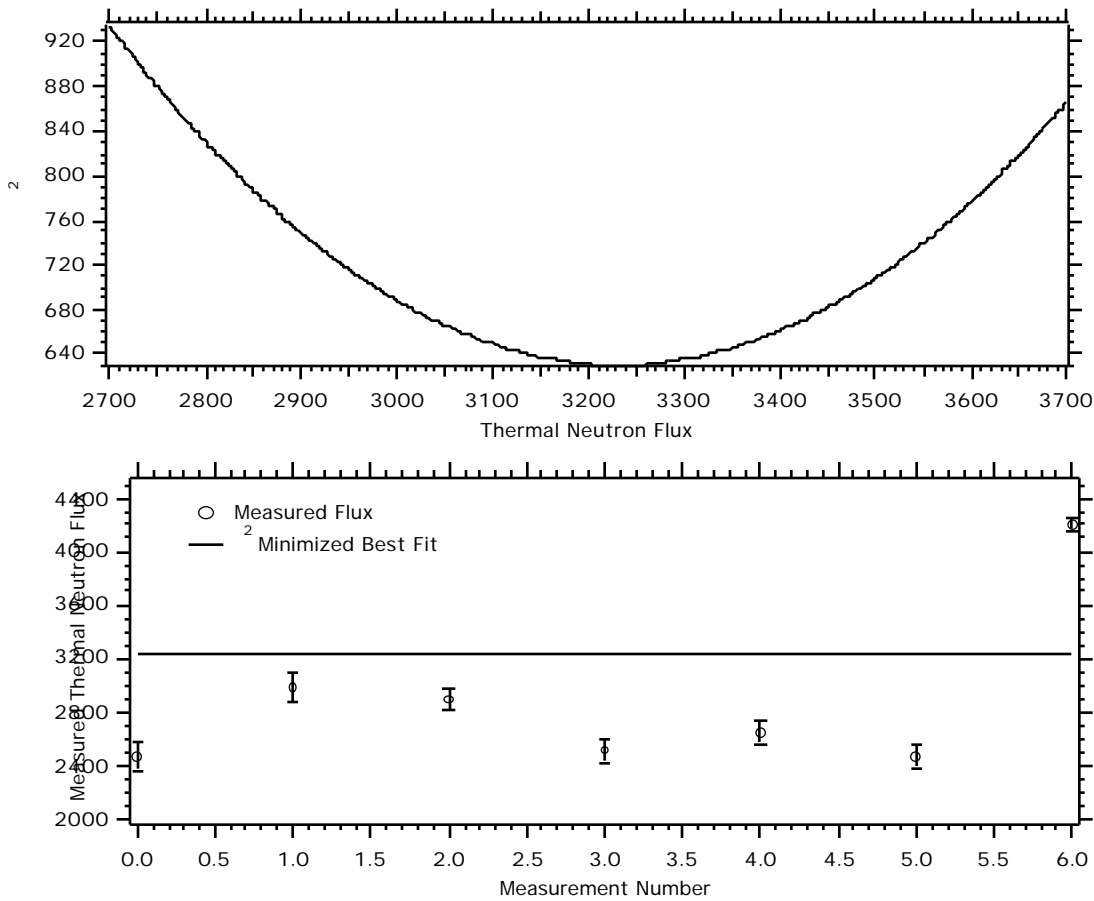
A total of 8.2 m^2 days of thermal neutron data was recorded on strings D8, C4, C1, B2, B4, B7, and counter S5-200A-1. A summary of calculated fluxes from these measurements can be found in Table 4.4

123

Table 4.4: Summary of thermal neutron measurements. Flux results are in units of neutrons /m^2/day. The first error is statistical, the second is systematic.

String	Digitized Data Result	ADC Data Result
D8	N/A	2438.4±82.5±62.1
	2329.6±84.8±59.0	2483.9±87.7±62.9
	N/A	2505.5±117.4±63.7
C4	3057 ±160.2 ±77.8	3075 ±160.9 ±77.8
	N/A	2885.1±77.9±73.3
C1	2671 ±102.9 ±53.2	2858 ±106.3 ±72.6
	N/A	2818 ±66.8 ±71.6
	N/A	2902.0±78.3±73.8
B2	N/A	2516.7±108.2±63.8
	N/A	2522.5±75.5±64.2
B4	N/A	2682.4±77.6±68.2
	N/A	2610.2±110.4±66.4
B7	N/A	2470±107.1±62.7
	N/A	2466.3±74.6±62.7
S5-200A-1	N/A	4144.9±49.8±105.3

A χ^2 test was performed on the average flux measurement obtained from each string in Table 4.5. The test indicates very poor agreement between measurements. The upper panel of Figure 4.38 shows the calculated χ^2 as a

function of thermal neutron flux value. The lower panel shows the data in relation to the χ^2–minimized best fit value.

Figure 4.38: Upper frame: χ^2–test for a straight line fit to the thermal neutron flux data. Lower Frame: χ^2–minimized best fit thermal neutron flux value plotted with the data.

In an attempt to explain the data, the geometry of the strings in the cooldown phase was examined. The strings are assembled and operated in an array as depicted in Figure 4.27. It was originally believed that the geometry of the array would not have an impact on the measurement of the neutron flux owing to the gas-like properties of thermal neutrons. In a more realistic model, the

detection solid angle was calculated for each counter via geometrical methods by considering only the proximity of other ^{3}He counters. These calculated values expressed as a fraction of the maximal 2π azimuthal detection angle are listed in Table 4.5.
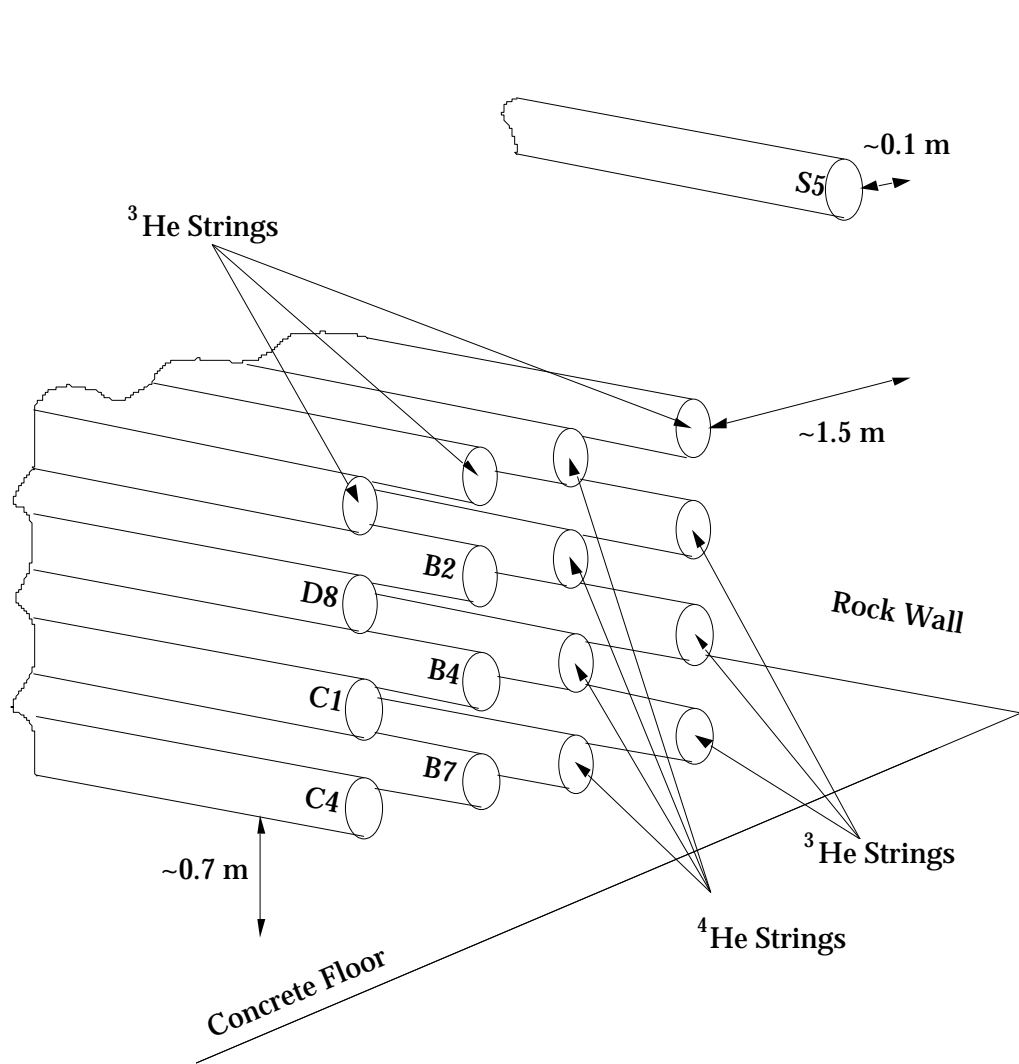
Figure 4.39: Layout of the array used to measure the thermal neutron flux. The rock wall and the concrete floor were about 1 m away from the array.
Table 4.5: Calculated fractional detection solid angle (detection solid angle$/2\pi$) for the NCD strings in the geometry shown in Figure 4.27.

String	Detection Solid Angle

D8	0.697
C1	0.697
C4	0.797
B2	0.57
B4	0.57
B7	0.707
S5-200A-1	1.0

A χ^2 test was then applied to the data with the thermal neutron flux estimates for each string that were attenuated by the respective solid angle factors. The upper panel in Figure 4.40 shows the calculated χ^2 as a function of thermal neutron flux value. The middle panel shows the data in relation to the χ^2–minimized best fit value, and the bottom panel shows residuals.
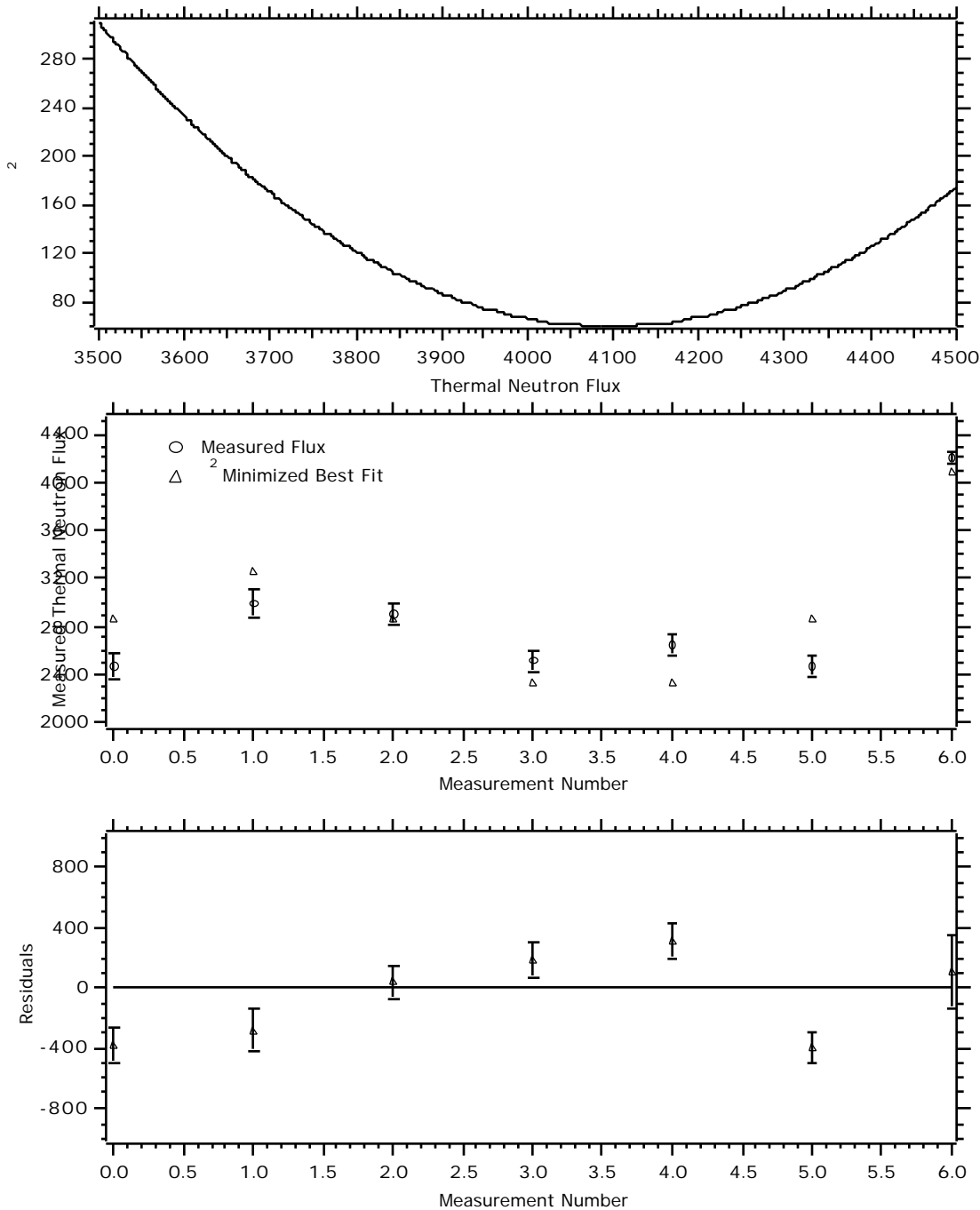
Figure 4.40: Upper frame: ^{2} test for a solid angle attenuated fit to the thermal neutron flux data. Lower Frame: ^{2}-minimized best fit thermal neutron flux value plotted with the data.

128

While the solid angle attenuated χ^2 distribution does not offer compelling evidence as to the accuracy of the best-fit thermal neutron flux value of 4100 neutrons /m²/day, it does appear to suggest that the data can be partially explained via solid angle arguments. It should be noted that the data taken on the counter S5-200A-1 was recorded prior to the cool-down array installation[4]. The assigned fractional detection solid angle of 1 is therefore viewed as quite accurate. Additionally, the measured flux of 4144.9 ± 49.8 ± 105.3 neutrons /m²/day from this counter appears to agree with the best fit estimate.

The calculated solid angle attenuation constants are most likely too simplistic to comprehensively explain the observed shadowing. It would be naïve to expect a high degree of success from such a simple treatment considering the random nature of thermal neutron scattering. The use of a neutron transport code would provide the most comprehensive description of shielding.

Previous measurements of the underground neutron flux [65] utilizing BF_3 counters yielded deduced flux values between 3000 - 28,000 /m²/day at various depths and in the vicinity of different rock types in the mine housing the SNO experiment. The measurement corresponding most closely to the rock type and depth of SNO yielded a deduced flux of 3024 /m²/day.

4.8 Summary of Cool-down Phase Measurements

The primary goal of the NCD cool-down phase is to allow the cosmogenically activated ^{56}Co to decay away prior to the installation of the array in SNO.

---

[4] At the time data was taken on counter S5-200A-1, only 3 ^{3}He counters were underground, and these counters were stored several meters away.

Additionally, during the cool-down phase, measurements were performed to asses the operational characteristics of the counters, measure the inherent U and Th contamination in the counters, and measure the thermal neutron flux underground at the SNO site.

Determining the operational characteristics of the NCDs included verifying that the counters remained intact after shipment, assessing the operational gain and resolution of individual counters and composite strings of counters, as well as attempting to ascertain the long-term stability of the counters. There are currently xxx NCDs underground, representing approximately xx% of the array. Of the counters shipped underground, 96% have passed the characterization, gain, and resolution tests. The remaining 4% have been shipped back to UW for repair.

Three analysis techniques were employed to assess the U and Th contamination in the NCDs. All three techniques required the analysis of digitized data to enable the separation of ^{210}Po alphas from U and Th alphas. RNAA studies indicate that the Th contamination is at the 1-2 ppt level. The measurements taken during the cooldown phase were designed to provide independent confirmation of these results from completely assembled counters. The results of the cooldown phase measurements are consistent with the RNAA results, indicating a best-fit estimate of less than 1 ppt of Th, and less than 9.5 ppt of U. The associated uncertainties of these results are relatively large due to the limited statistics. An estimate of the run-time required to reduce these uncertainties to 20% can be found in Section 5.3.

The final measurements described in this chapter involved data taken to determine the underground thermal neutron flux. These measurements utilized an array of ^{3}He counters operated as strings to maximize detector surface area. Solid angle attenuation coefficients were attributed to each string, describing the proximity of other ^{3}He counters in order to explain the observed neutron "shadowing" in the array. Chi-squared minimization of the solid-angle-normalized measurements indicate an underground flux of 4100 neutrons/m^2/day. This result is in good agreement with an earlier NCD measurement of 4144.9 $\pm$ 49.8 $\pm$ 105.3 neutrons/m^2/day taken prior to the installation of the cooldown array. Furthermore, this result is comparable to a much earlier measurement of 3024 neutrons/m^2/day utilizing BF$_3$ counters.

Data taken during the cool-down phase of the NCD program has provided valuable information regarding potential backgrounds to the NC measurement in SNO. A detailed discussion of the impact of the anticipated backgrounds to the NCD NC measurement is provided in Chapter 5.

5.1 Estimation of NCD Array Backgrounds from Cool-Down Phase Measurements

While the cool-down phase of the NCD program is still in the early stages (nearly 30% of the array underground), an estimation of the NCD array NC backgrounds can be made from the initial measurements. The background scenario described below assumes that the nickel for the entire array will have reached saturation by cosmogenic activation[1], and includes an underground storage period of at least six-months prior to deployment.

The backgrounds associated with the NCD array NC measurement in SNO can be divided into two categories: events intrinsic to the counters, and external sources of background neutrons. The former category includes events that can be energetically identical to the ^{3}He(n,p)t reaction in an NCD (Compton events, alpha events from U, Th and Po). Separation of these events from neutrons will be accomplished primarily through analysis of the background-free window that was described in Chapter 4. This window provides a region in the charge-pulse risetime versus energy phase space in which 45% of all neutron events are contained, but that is free from the intrinsic background events.

There is an additional source of intrinsic background which is not included below, but should be mentioned for completeness. The potential

---

[1] As discussed in Chapter 4, this most likely will not be the case. This scenario is intended to provide an upper limit on the backgrounds for the NCD array.

contamination of the background free window from "end-effects" was discussed in Section 4.3.2. Alpha particles emitted from the decay of ^{210}Po, as well as from the U and Th decay chains, near the endcap region of the NCDs can give rise to an event topology which may contaminate this window. The extent of this contamination has yet to be quantified, but a combination of Monte Carlo studies and test counters is currently planned. The modeling of this potential background involves the modification of existing Monte Carlo code to include the effects of alpha particle emission in the end-cap region of the NCDs. The code is capable of describing the shape of the current-pulses from various particles of interest in the NCDs, and will be modified to determine the effect on the background free window of abnormal ionization profiles as a result of the quartz field tubes. A specially-made "end-effect counter" is nearly complete, and will provide data as to the extent to which the background free window may be contaminated. This counter was produced in a nearly-identical manner as a typical NCD, with the exception of feedthrough s made of aluminum. Aluminum tends to contain large amounts of U and Th (on the order of a few Parts Per Million (ppm)), and thus will provide a sizable number of alpha emissions in the endcap region.

The second NCD array NC measurement background category is the result of neutrons produced from the photodisintegration of deuterium, cosmic ray spallation, antineutrino reactions in the D_2O, and the fission of U. These neutrons are not separable from NC neutron events, and so these backgrounds must be calculated or measured to enable a subtraction of their contribution.

There are several sources that give rise to the photodisintegration background. These are attributed to the decay chains of U and Th, as well as the decay of the cosmogenically activated ^{56}Co present in the Ni bodies of the NCDs. As previously mentioned, U and Th is present at some level in all the materials used in the construction of SNO – the criticality of this contamination ultimately depends on the proximity of the material to the D_2O. In assessing the NC background, the maximum allowable limit as listed in Table 2.2 was used unless the contamination has been measured, in which case the measured value was used. The maximum limit equates to 2 photodisintegration neutrons per day from the decays of U and Th for each of the following regions: D_2O volume, acrylic vessel, and H_2O volume. Additionally, a comprehensive photodisintegration assessment needs to include the contribution from U and Th in the nearly 10,000 PMTs, and the associated support structure (PSUP).

U and Th contamination in the D_2O and H_2O is monitored via sampling locations in the fill and circulation systems. The current measured limits on the contamination in the D_2O is < 20 fg/g Th, and < 20 fg/g U. The limit on the H_2O is < 0.09 pg/g Th, and < 0.01 pg/g U. The uncertainty associated with assaying the U and Th contamination is about 10% [66]. The anticipated photodisintegration background based on these measured values is negligible from the H_2O volume, but approximately 1.5 neutrons/day from the D_2O, representing a sizable background to the NC measurement.

After the D_2O, the volume most sensitive to U and Th contamination is the acrylic vessel. Throughout the construction of the vessel, the U and Th content of

the materials was determined via neutron activation, mass spectrometry, and alpha spectroscopy techniques. In order to accommodate the likely introduction of additional contaminants during the construction phase, the limits on the virgin acrylic sheets were placed at 2 pg/g Th and 7 pg/g U. Measurements taken of acrylic samples indicated a contamination of Th < 0.1 pg/g at the 2 level [67] - well below the design limits. While inclusion of additional contaminants was unavoidable during construction of the vessel, extraordinary efforts were made to minimize the possibility. *In situ* measurements of the U and Th contamination of the completed vessel were not possible, however, tape lifts of the vessel were analyzed via X-Ray Florescence techniques (XRF) to determine if excessive surface contamination was present. The combined information from the acrylic measurements and the post construction measurements appear to indicate that the vessel has met the design contamination limits. The photodisintegration background as a result of these contaminants is anticipated to be 2 neutrons/day, and represents the single-largest source of photodisintegration neutrons.

There are several additional sources of background neutrons that require consideration. The largest contribution is the result of cosmic ray spallation in SNO. Despite the 5900 m.w.e. of overburden, the muonic flux is approximately 90 /m^2/year. At this depth, it has been calculated that 2.0×10^{-3} neutrons/g/cm^2/μ are produced [68], which equates to almost 40 neutrons/day in SNO. The average energy of the muons is between 500 and 600 GeV [69], indicating that virtually all the muons will pass completely through the detector

138

volume. The C̆erenkov light signature of these extremely high energy events is very characteristic, thus providing an anticipated 99+% identification efficiency [70].

In order to remove the muon-induced neutron background, a coincidence window veto will be utilized. The window is started upon detection of a muon, and the width of the window is set by the characteristic lifetime of neutrons in SNO. Neutrons in the D_2O volume rapidly thermalize through multiple scattering, and subsequently are captured by deuterium, hydrogen or an NCD. The mean lifetime for this process is on the order of about 15 ms [71]. Any neutrons detected within this period of time after a muon event will be attributed to muon spallation.

An estimate of the number of neutrino-induced NC events which are accidentally rejected as a result of a muon coincidence veto can be made based on the anticipated muon and NC rates, and the neutron lifetime. The number of neutrons produced in SNO as a result of NC interactions is anticipated to be between 6 and 42 /day according to the latest SuperK results [72]. This range represents the number of SuperK observed events scaled to the NC reaction in SNO for the scenarios of neutrino oscillations (42/day) and no oscillations (6/day). Assuming a NC signal of 42 /day (R_{NC}), and a muon flux of about 40 /day (R_μ), the rate of NC accidental coincidences ($R_{accidentals}$) in a t time window is given by Equation 5.1. The NC detection efficiency ($_{NC}$) is anticipated to be about 45%, and the muon identification efficiency ($_\mu$) is approximately 100%.

$$R_{accidentals} = {}_{NC}R_{NC} {}_\mu R_\mu \ t \qquad (5.1)$$

139

This rate is exceeding small (< 0.3×10^{-3} /day) for a 30 ms coincidence window, and can be considered negligible in determining the NC signal.

Deuterium breakup by alphas also gives rise to a neutron background in SNO. There are only three decays in the U and Th chains with an alpha of sufficient energy to drive the reaction shown in Equation 5.2.

$$\alpha + d \rightarrow n + p + \alpha \tag{5.2}$$

The rate of this reaction has been calculated [68] to be 22 neutrons/year from the U decay chain assuming 20 µg of U contamination in the D_2O volume, and 5 neutrons/year from the Th decay chain (assuming 3.7 µg of Th contamination in the D_2O volume).

The presence of U in the D_2O volume is an additional source of background neutrons via spontaneous fission. The current measured upper limit on the U content in the D_2O volume is 20 µg (20 fg/g D_2O) [73]. For a specified number of U atoms, N_U, the number of fission events is given by Equation 5.3.

$$\# \text{ fission events} = (N_U) \times (\lambda_U) \times (\text{fission probability}) \tag{5.3}$$

The decay rate of ^{238}U (λ_U) is $0.693/t_{1/2}$, where the half-life ($t_{1/2}$) is 4.468×10^9 years, and the fission probability is 5.5×10^{-5}. For the measured 20 µg of U contamination, 4.3 U fission events/year can therefore be expected in SNO. Each fission gives rise to 2 neutrons, thus indicating 8.6 neutrons/year from the spontaneous fission of U.

Given the measured U and Th contamination in the D_2O, neither the d(α,n)p reaction or the fission of U represent a serious contribution to the

140

neutron background. Even a factor of 10 increase in the contamination would imply a small number of neutrons from these sources.

The relative natural abundance of ^{17}O is 0.038%. Assuming that this isotope is not enriched in the D$_2$O, there should be approximately 1.3×10^{19} ^{17}O atoms in the D$_2$O volume of SNO. These atoms can give rise to a free neutron through the reaction shown in Equation 5.4.

$$^{17}\text{O} + \alpha \rightarrow n + {}^{20}\text{Ne} \qquad (5.4)$$

The source of the alphas is the decay of ^{210}Po present on the surface of the NCDs, as well as the decay chains of the ^{238}U and ^{232}Th in the D$_2$O. For a concentration of 20 μg U and 3.7 μg Th in the D$_2$O volume, and a ^{210}Po decay rate of 10^5 /m^2 of NCD/d, the rate of the reaction shown in Equation 5.3 was calculated [68], giving a production of 35.52 neutrons/year. Even if there was a significant enrichment of ^{17}O, the measured limits on the U, Th, and Po contamination indicate that alpha bombardement of ^{17}O will not be a significant source of background neutrons.

The final presumed source of neutrons in SNO are the result of antineutrino interactions. In addition to the antineutrinos emitted by the U and Th decay chains, terrestrial fission reactors also produce a non-negligible antineutrino flux in SNO. There are three reactions (Equations 5.5 - 5.7) through which antineutrinos can produce a free neutron.

$$\bar{\nu}_e + p \rightarrow n + e^+ \qquad (5.5)$$

$$\bar{\nu}_e + d \rightarrow n + n + e^+ \qquad (5.6)$$

$$\bar{\nu}_x + d \rightarrow p + n + \bar{\nu}_x \qquad (5.7)$$

141

The neutron production rate in SNO via antineutrino reactions from these sources has been calculated in References **68** and **74** to have an upper limit of 49 /year.

Table 5.1 lists the individual contributions to the photodisintegration background neutrons, and Table 5.2 lists the additional sources of background neutrons.

Table 5.1: Sources of photodisintegration backgrounds.

Photodisintegration Neutron Source	Concentration (Goal)	Concentration (Measured or Estimated)	Neutrons (/day)
^{56}Co (NCD)	none	Saturated w/ 6 mo. u/g	0.5
U and Th (NCD)	1-2ppt Th 25 ppt U/NCD array	<1 ppt Th <9.5 ppt U	< 0.5
U and Th (D$_2$O)	3.7 fg Th 45 fg U/g D$_2$O	<20 fg Th <20 fg U	1.5
U and Th (H$_2$O)	0.13 pg Th 1.0 pg U/g D$_2$O	<0.09 pg Th <0.01 pg U	~0
U and Th (Acrylic Vessel)	2 pg Th 4 pg U/g D$_2$O	2 pg Th 4 pg U/g D$_2$O	2.0
U and Th (Rock)	3.3 µg Th 1.2 µg U/g norite	3.3 µg Th 1.2 µg U/g norite	~0
U and Th (PMTs and PSUP)	4.2 mg Th 4.3 mg U /PMT	4.2 mg Th 4.3 mg U /PMT	1.8
Total:			6.3

Table 5.2: Additional neutron sources in SNO

Additional Neutron Source	Neutrons (/day)
Cosmic Rays	38.4
Uranium Fission	0.01
d(,n)p	0.07
$^{17}O(,n)^{20}Ne$	0.1
Antineutrino Reactions	< 0.13
Total:	< 40

Many of the background sources listed in Table 5.1 and 5.2 have been shown to contribute negligibly, or can be separated with high efficiency. The photodisintegration sources, however, give rise to a significant neutron background which cannot easily be separated from the NC signal. From the perspective of an individual string or counter, this is certainly true. Some degree of background separation is possible, however, by exploiting the geometry of the NCD array.

5.2 Separation of Backgrounds after Deployment

The NCD array detection probability of various neutron spatial distributions was studied through Monte Carlo analysis [74]. The purpose of this study was to quantify if different background sources could be separated based on detection distributions using the symmetry of the array. In addition to the five primary sources (NC signal, photodisintegration events from U and Th in NCDs, D_2O, acrylic vessel, and PMTs/PSUP), the distribution of photodisintegration neutrons as a result of localized "hot-spots" in both the NCDs and acrylic vessel were studied. These hot-spot events were generated to model the effect of a concentration of U and Th in either a single counter (string) or in the acrylic vessel itself.

The simulated neutral current interaction neutrons were produced isotropically in the D_2O as would be expected for a flux of neutrinos incident on the D_2O volume. The photodisintegration neutrons from the U and Th in the NCD material and the U and Th in the D_2O were also distributed isotropically in the detector volume. In the case of the latter, this distribution is assumed to be valid as the U and Th will most likely be uniformly distributed throughout the D_2O. The photodisintegration neutrons from the U and Th in the NCD material are most likely to be captured on the string which gave rise to the neutron (as opposed to another string) because of the short interaction path length of neutrons in D_2O. If the U and Th contamination in the NCD material is uniformly distributed, this neutron component will therefore manifest itself as an isotropic

144

background. Photodisintegration neutrons as a result of U and Th in the acrylic vessel were produced preferentially close to the walls of the vessel due to the comparatively short mean free path of the -ray (18 cm) with respect to the radius of the vessel. Finally, hot-spots were generated similarly to the NCD and acrylic vessel backgrounds, only without the symmetry.

Figure 5.1 shows the Monte Carlo results of the NCD neutron detection probability for the isotropic, acrylic vessel, and hot-spot distributions as a function of radial NCD location.

In a test of the ability to separate the isotropic background from the acrylic vessel background (AV background), 1000 simulations were run generating 2730 isotropic neutrons and 125 neutrons from the AV background according to the detection distributions shown in Figure 5.1. The isotropic neutrons number (2730) is the sum of 2500 NC events (1/2 SSM), and a combined 230 events from the U and Th in the heavy water at the 10^{-15} g/g level, and a 2 ppt U and Th contamination in the NCD material. The results of these simulations indicate a less than 3% error in the ability to extract the isotropic signal from the AV signal.

Difficulties in accurately separating the isotropic and radially-dependent distributions arose when localized hot-spots were included in the simulations. In one example, a hot-spot on the equator of the vessel was included as contributing 50 neutrons per year. The impact on the fit was to decrease the extracted isotropic component by 1 . A non-uniform contribution of this magnitude would therefore have an obvious adverse effect on the extracted NC signal.

145
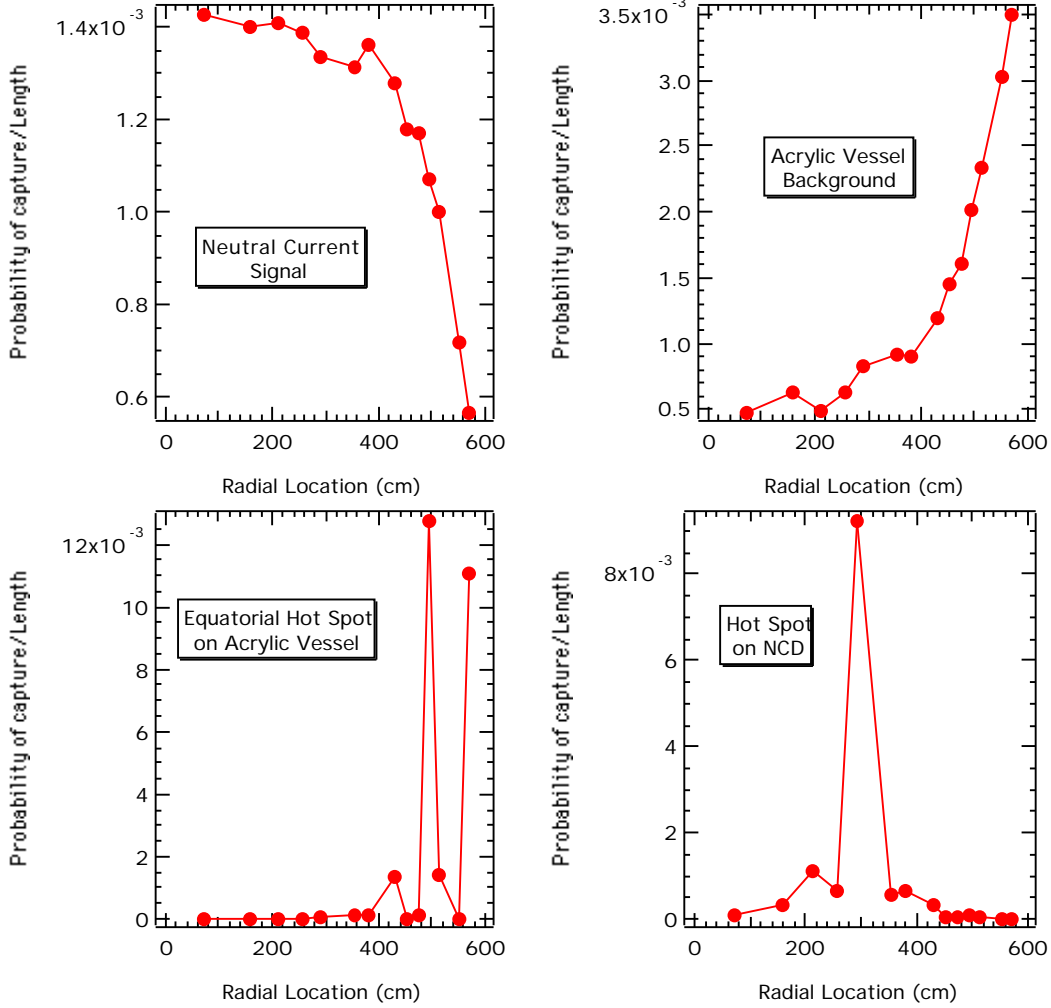
Figure 5.1: NCD array detection probability for isotropic (upper left), acrylic vessel (upper right), acrylic vessel hot-spot (lower left), and NCD hot spot (lower right) neutron distributions [75, 76].

Fortunately, a hot spot can be identified *in situ* by exploiting the azimuthal symmetry of the NCD array. Figure 5.2 shows a "floor-plan" of one quadrant of the NCD array. The strings can be grouped by radial distance into 13 rings (It has since been decided not to deploy the strings corresponding to the 14th ring of the drawing). If the isotropic and AV backgrounds contributions are assumed to be

146

azimuthally symmetric, a hot-spot (almost by definition), will be azimuthally asymmetric. By examining the neutron capture distribution as a function of the NCD radial location, hot spots will become evident by strings which demonstrate a statistically inconsistent rate in comparison to other "ring-mates". Identifying and removing the hot-spot contribution has been demonstrated through Monte Carlo studies to regain the original separation accuracy. A complete description of these studies can be found in References 75 and 76.
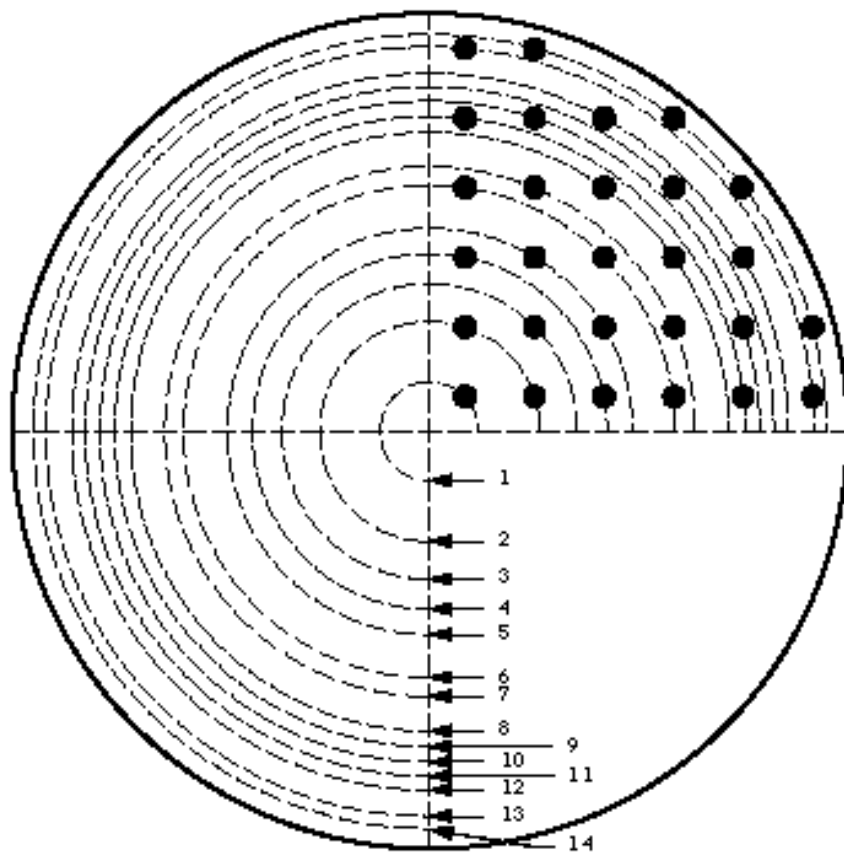

Figure 5.2: Plan view of one quadrant of the NCD array.

5.3 Calculation of the NC Signal

Once hot-spots have been identified and isolated, extracting the NC signal can be accomplished as described below. A more detailed description of this method can be found in Reference 76. The total number of neutrons (N_T) is the sum of the isotropic neutrons (N_I) and radial neutrons (N_R). Monte Carlo studies have shown that these components can be separated to a high degree of accuracy. This leaves only the separation of the various contributions to N_I in order to extract the NC signal (N_{NC}). The observed N_I is a combination of the NC signal and isotropic neutrons from the photodisintegration of deuterium ($N_I^{,n}$) multiplied by the NCD array detection efficiency, . (Equation 5.8)

$$N_I = (N_{NC} + N_I^{,n})$$
(5.8)

Inverting Equation 5.8 and solving for N_{NC} yields Equation 5.9.

$$N_{NC} = \frac{1}{}N_I - N_I^{,n}$$
(5.9)

The array efficiency needs to be determined from calibration with a ^{252}Cf source, requiring the conversion of individually measured string detection efficiencies into an overall array efficiency. N_I is obtained from the fit mentioned above, and $N_I^{,n}$ can be deduced from *in situ* measurements with the PMT array.

The error on the NC measurement can be expressed in terms of the errors of the elements of Equation 5.9, and is shown in Equation 5.10. The 's are the uncertainties associated with the individual contributions to Equation 5.2.

$$_{NC}^{2} = (\,^{2} + \,_{I}^{2}) \times (1 + \frac{N_I^{,n}}{N_I - N_I^{,n}})^2 + (\frac{N_I^{,n}}{N_I - N_I^{,n}})^2 \times (\,_I^{,n})^2$$
(5.10)

148

The uncertainty associated with the determination of the array efficiency ( ) is driven by many factors; source standardization, source position, string position, and D_2O purity/enrichment among others. A comprehensive treatment of these parameters and the calibration of the NCD array can be found in Reference 77. In general, the contributions to this efficiency are well understood, and the overall uncertainty is presumed to be less than 10%.

The uncertainty on the number of observed isotropic neutrons ($_I$) is a combination of counting statistics, and the uncertainties associated with separating the isotropic from radial neutron components described in Section 5.2. The separation efficiency was demonstrated through Monte Carlo studies to be about 3%, and the statistical uncertainty associated with the observed isotropic neutrons can be estimated from Tables 5.1 and 5.2. The only significant sources of isotropic signal comes from the anticipated NC signal in SNO (6 - 42 /day), U and Th in the D_2O (1.5 /day) and NCDs (0.5 /day), as well as the ^{56}Co in the NCDs (0.5 /day). Combined, these sources give rise to an anticipated 8.5 - 44.5 neutrons /day. Assuming an array detection efficiency of 45%, and a year of NC data, the statistical uncertainty on the isotropic component of the signal would be less than 3% over the entire anticipated range of the NC signal.

The uncertainty associated with the isotropic photodisintegration neutrons ($_I^n$) depends on how well we understand the U and Th contamination in the NCDs, how much ^{56}Co has decayed away, and the U and Th contamination in the D_2O. The total uncertainty is a combination of these three factors coupled with the isotropic/radial extraction uncertainty of 3%

149

mentioned above. The measured U and Th content of the D_2O is listed in Table 5.1, and has an uncertainty of 10%. The amount of ^{56}Co in the NCDs depends on the underground storage time prior to deployment, and its contribution in Table 5.1 assumes that the array would be underground for at least 6 months. The calculated neutron production rate in SNO due to this effect has about a 20% uncertainty.

Attempting to understand the U and Th content of the NCDs was a major part of this thesis work. The best-fit estimate described in Section 4.6.2 indicates that the U contamination is less than 9.4 ppt, with a 20% fractional uncertainty, and the Th contamination is less than 1 ppt, with an extremely large, ~700%, fractional uncertainty. Any estimate of the NC signal uncertainty using these values will yield an unsuitably large number. The question becomes: How long will it take to achieve reasonable (~20%) uncertainty levels on the NCD U and Th contamination using the methods outlined in Chapter 4?

The analysis of the U and Th contamination utilized 56.67 m^2 days of data. If only the two truly independent techniques are considered (analysis Region 1 and analysis Region 4), how much additional data is required to understand the U and Th contamination at the 20% level? These uncertainties are driven primarily by counting statistics, and thus, the fractional uncertainty as a function of m^2 days of data can easily be calculated. Figure 5.3 shows a plot of the U and Th fractional uncertainty, at concentrations of 9ppt and 1 ppt respectively, as a function of m^2 days of data.

150
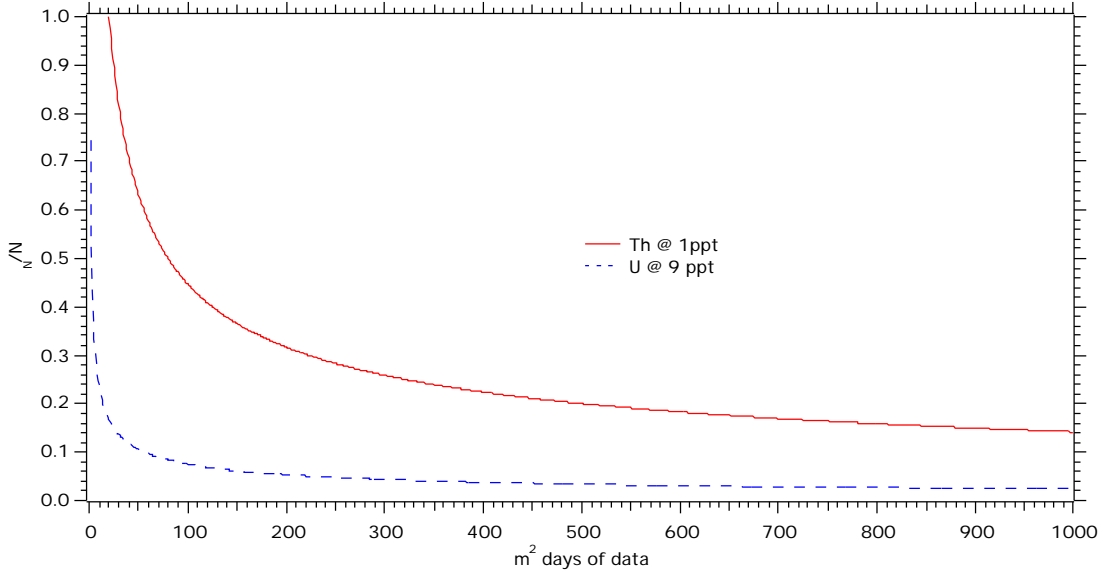
Figure 5.3: Fractional uncertainty in the measured U and Th contamination as a function of m^2 days of data.

As is evident by examining Figure 4.33, the U contamination has already been constrained at the 9 ppt level with better than 20% uncertainty. Constraining the Th contamination at the 1 ppt level to a similar uncertainty will take a bit more time given the current cool-down configuration. Once deployed and operational in SNO, however, the array consists of 120 square meters of counter. Figure 5.3 shows that running the array for just over 4 days will yield the desired sensitivity.

Table 5.3 lists the anticipated uncertainties that contribute to $_{NC}$. The total estimated uncertainty is shown to range from 11 - 17% for a NC signal rate of 42 /day and 6 /day respectively. It should be noted that this estimate assumes that the U and Th contamination in the NCDs has a fractional uncertainty of 20%. As

151

shown above, this uncertainty will decrease rapidly upon operation of the entire NCD array.

Table 5.3: Anticipated NCD uncertainties.

Uncertainty	Assumption(s)	Anticipated Value
		10%
$_I$	1 yr NC data (6-42 n/day)	< 3%
$_I{}^{,n}$	U and Th in NCDs known with 20% unc.	20%
$_{NC}$	= 45% 1 yr NC data (6-42 n/day)	11 - 17%

5.4 Extracting the CC/NC Ratio

As mentioned at the end of Chapter 2, the most interesting potential of SNO is its sensitivity to neutrino oscillations via the NC interaction. The CC interaction in SNO will provide high-statistics for the $_e$ flux, and the NC reaction will provide the total flux of all neutrino flavors. By comparing the fluxes of CC to NC as a ratio, the correlated uncertainties associated with the neutrino cross-sections cancel. A ratio less than 1 would be indicative of neutrino oscillations, while a ratio of 1 would imply no neutrino oscillations.

Figure 5.4 shows a plot of the anticipated sensitivity of SNO to this ratio assuming a year of CC data, and a year of NC data. This estimate assumes a total NC uncertainty ($_{NC}$) of 11% (bottom plot) and 17% (top plot), an array detection

152

efficiency of 45%, and a NC background of 1000 events/year. This background estimate excludes neutrons as a result of cosmic ray interactions, and radial photodisintegration sources (i.e. acrylic vessel, PMT and PSUP contributions). These backgrounds are presumed separable based on the discussions in Sections 5.1 and 5.2. The remaining background neutrons are the result of U and Th in the NCDs (185 /year) and D_2O (550 /year), and the cosmogenically activated ^{56}Co in the NCDs (185 /year).

The CC to NC ratio is plotted against the $_e$ flux normalized to SSM flux predictions. The two hypothesis are clearly resolvable in both plots, indicating that after a year of NC and CC data, SNO will be sensitive to neutrino oscillations over the entire range of the anticipated NC signal.
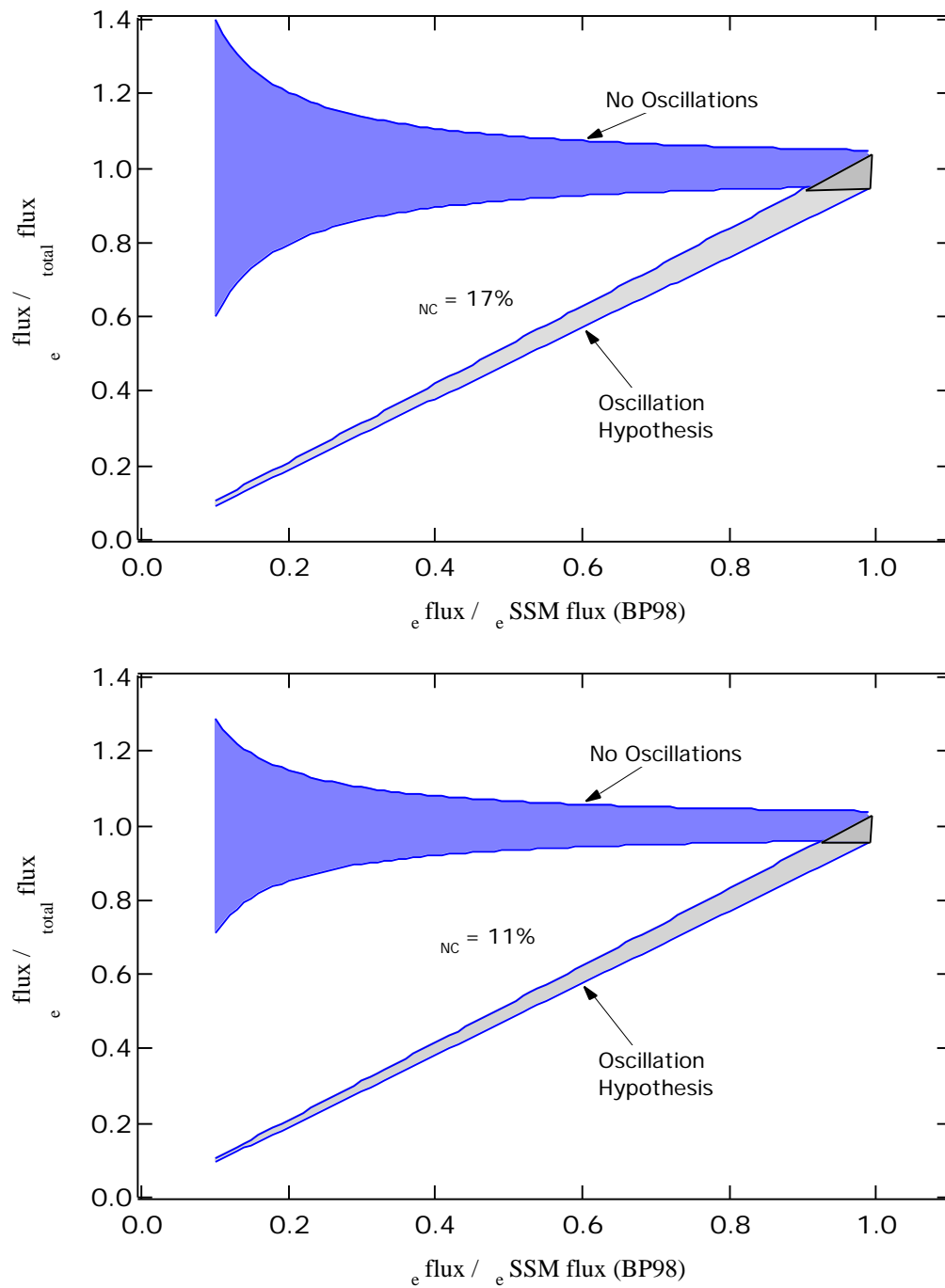
Figure 5.4: CC/NC ratio plotted versus the ν_e flux (normalized to SSM (BP98)) [78].

5.5 Current NCD Status

The overall status of the NCD program can currently be separated into four major categories: counter production, electronics/data acquisition development, data analysis, and deployment preparation.

The counter assembly facility at the University of Washington is currently preparing for increased counter production. A recent drop in the supply of endcaps from the manufacturer has resulted in a temporary production delay. There are currently 56 counters at site, and an additional 42 counters tested and boxed at UW for shipment to site. Once counter production resumes, all NCDs should be completed and at site mid-fall 1999 assuming a production rate of 10 counters/week.

The final electronics for the NCD program consists largely of custom designed and built components. The initial design, prototype, and testing has been completed. Preliminary data acquisition software exists for the individual

electronics components. Work is underway to develop the control software to integrate the NCD operation into the overall SNO data acquisition system.

The analysis of digitized waveforms will most likely prove to be an ever-evolving aspect of the NCD program. The pulse topology carries a wealth of information regarding the nature of the ionizing event, and current analysis techniques utilize only a small part of this information. Regardless, these analysis techniques enable the separation of bulk alpha activity from surface activity, and provide a window in which 45% of the neutron events are contained free of background events. Work is underway to improve on the neutron separation efficiency using neural networks and maximum likelihood fitters.
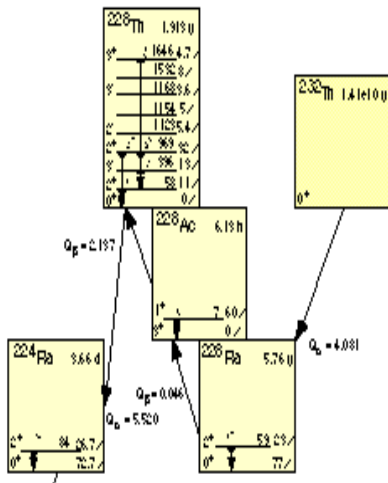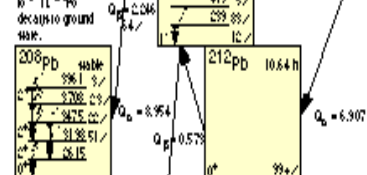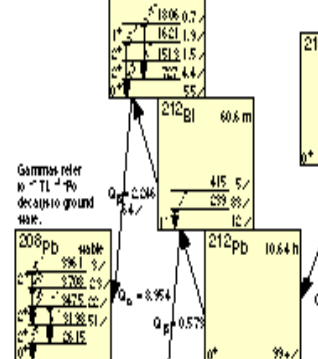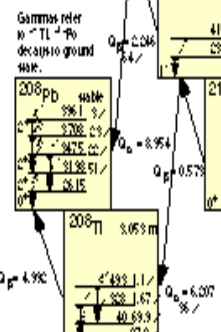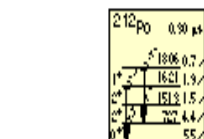
The deployment plan for the NCDs requires a submersible Remotely Operated Vehicle (ROV), and a large assortment of hardware. The design of the deployment materials is complete, and most of the components have been constructed and tested. In April 1999, a large scale test of the major deployment systems is scheduled in a 6 m deep water pool in Los Alamos. The test pool contains a mock-up of the neck of the acrylic vessel through which the NCDs must be deployed. It also contains NCD anchors on an acrylic panel at the bottom of the pool, thus enabling a nearly complete simulation of an NCD string deployment.

Appendix 1
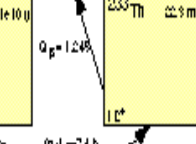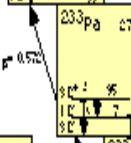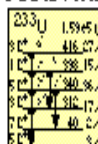
Decay of ^{232}Th to ^{208}Pb

Alpha Lines

|	MeV	%	Level
^{232}Th	4.011	77	0
	3.957	23	59
^{228}Th	5.423	72.7	0
	5.340	26.7	85
^{224}Ra	5.686	95.0	0
	5.449	5.0	241
^{220}Rn	6.288	99.9	0
^{216}Po	6.778	99+	0
^{212}Bi	6.090	27.2	0
	6.051	69.9	40
^{212}Po	8.785	??	0

Neutron Activation of - ^{232}Th
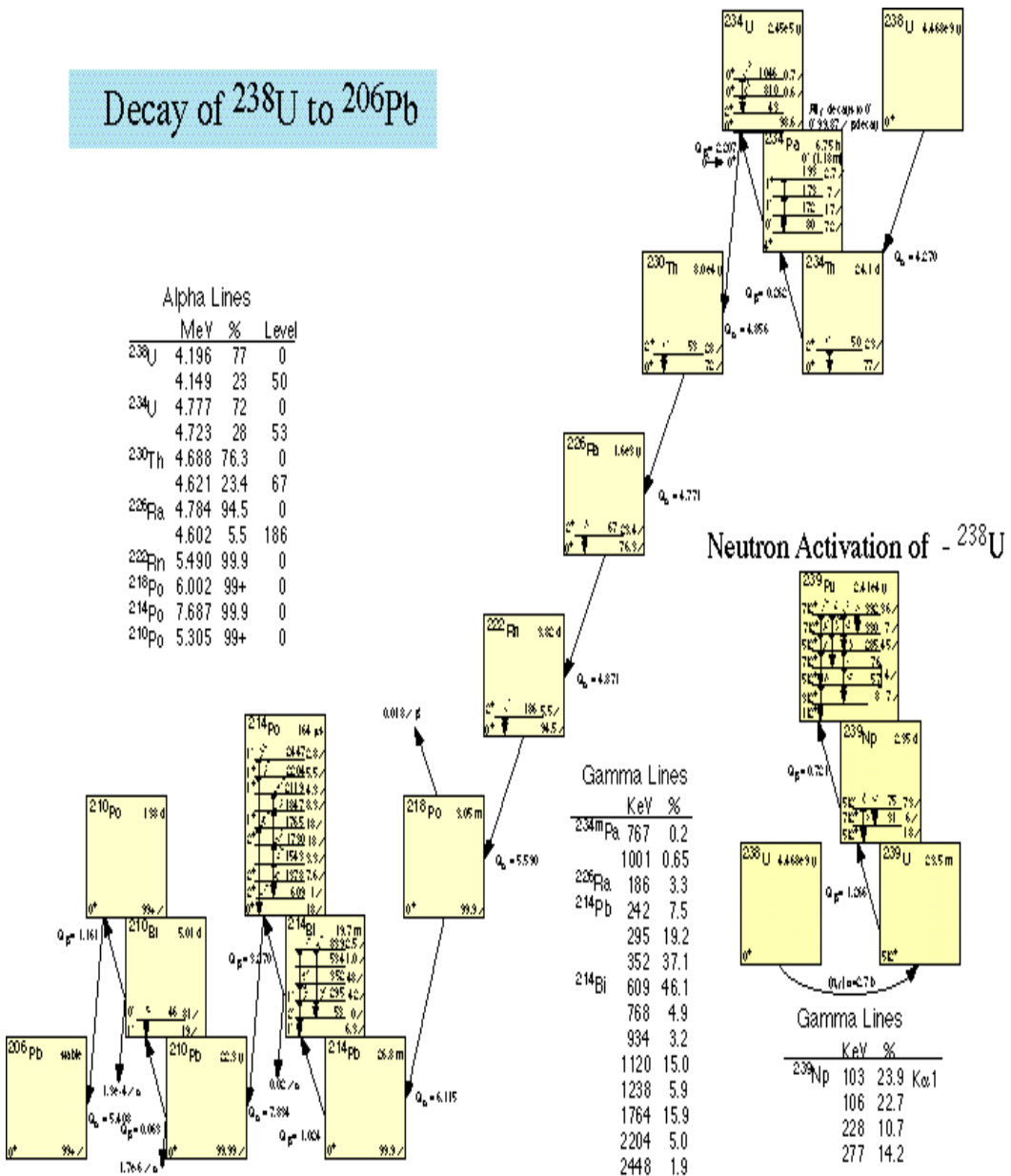
Gamma Lines

|	KeV	%
^{228}Ac	911	29?
	969	17.4
	1588	3.6
^{224}Ra	241	3.9
^{212}Pb	239	43.6
^{212}Bi	727	6.6
^{208}Tl	511	7.8
	583	30.9
	860	4.3
	2615	35.9

Gamma Lines

	KeV	%	
^{233}Pa	95	10.2	Kα2
	98	16.0	Kα1
	300	6.2	
	312	36.0	
	341	4.2	

155

Decay of ^{238}U to ^{206}Pb

Neutron Activation of - ^{238}U

Alpha Lines

	MeV	%	Level
^{238}U	4.196	77	0
	4.149	23	50
^{234}U	4.777	72	0
	4.723	28	53
^{230}Th	4.688	76.3	0
	4.621	23.4	67
^{226}Ra	4.784	94.5	0
	4.602	5.5	186
^{222}Rn	5.490	99.9	0
^{218}Po	6.002	99+	0
^{214}Po	7.687	99.9	0
^{210}Po	5.305	99+	0

Gamma Lines

	KeV	%
^{234m}Pa	767	0.2
	1001	0.65
^{226}Ra	186	3.3
^{214}Pb	242	7.5
	295	19.2
	352	37.1
^{214}Bi	609	46.1
	768	4.9
	934	3.2
	1120	15.0
	1238	5.9
	1764	15.9
	2204	5.0
	2448	1.9

Gamma Lines

	KeV	%	
^{239}Np	103	23.9	Kα1
	106	22.7	
	228	10.7	
	277	14.2	

156

A2.1 Logamp Characterization

The logarithmic amplifier is used to increase the dynamic range of the digitizer while maintaining acceptable digitization errors. Prior to the analysis of individual events, the waveforms must therefore be "de-logged" to extract the true information of the event. The general form of the amplification is shown in Equation A2.1.

$$V_{out} = a \times \log(1 + V_{in} / b) + c \qquad (A2.1)$$

The constants a, b, and c are routinely extracted and updated in the de-logging routine.

The constants are obtained through a fit of V_{out} vs V_{in} using the analytical form of Equation A2.1. The input and output of the logamp are digitized to obtain these voltages. Figure A2.1 shows a typical logamp input and output pulse. The pulse is chosen to be a slowly varying waveform over the amplitude of interest. In Figure A2.1 this waveform is a half-sine wave.

The extraction routine looks for the input and output waveforms to cross a pre-determined threshold. The routine then works back the pulse until it has reached the RMS value of the baseline noise. This point is determined to be the start of the pulse. A graph of V_{out} vs V_{in} is then generated, and a fit to the analytical expression is performed. This graph is shown in Figure A2.2.
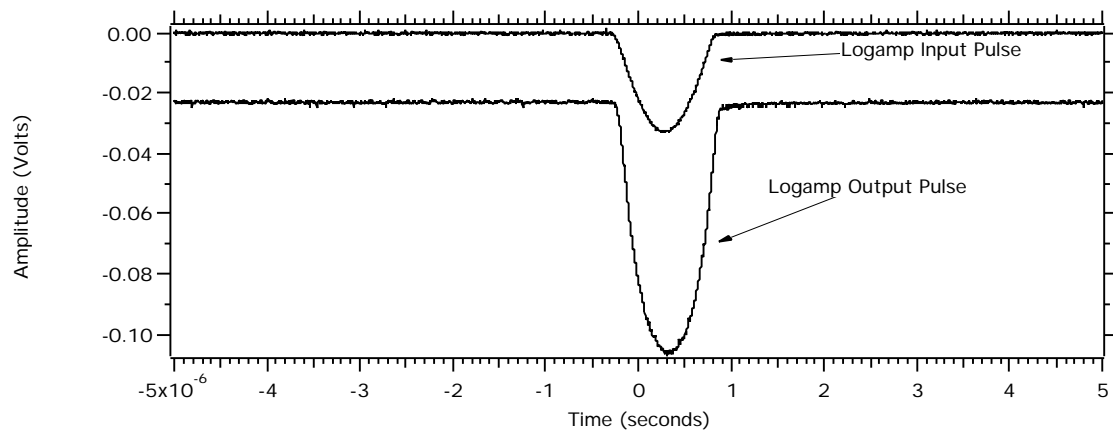
**Figure A2.1: Logamp input and output pulses.**
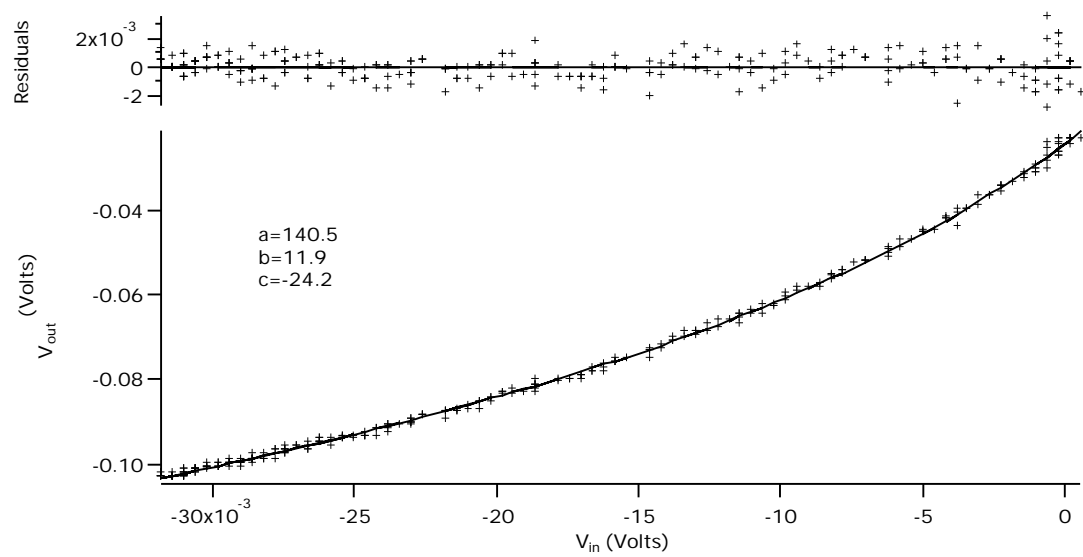
Figure A2.2: Fitted V$_{out}$ vs. V$_{in}$ graph.

158

The fit parameters are the constants a, b, and c. These values are then used to reconstruct the input pulse for comparison with the digitized input waveform. Figure A2.3 shows this comparison. The reconstructed pulse is offset to the right for clarity.
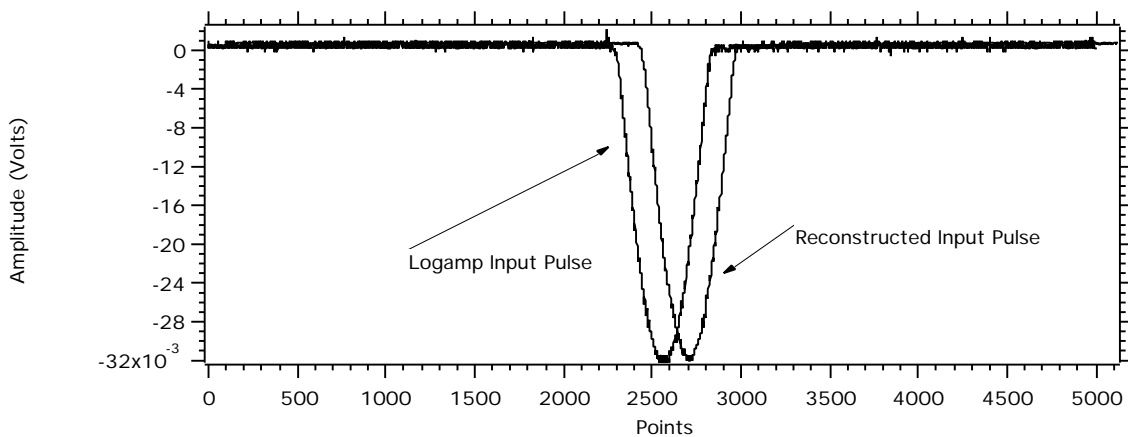

Figure A2.3: Logamp input pulse and reconstructed input pulse. The reconstructed pulse is displayed delayed for clarity.

Once the constants have been obtained and verified, they are entered into the digitized waveform analysis routine. Each digitization channel has its own logamp, and the constants for each channel are obtained separately. A concern is the stability of these constants over time and temperature. Tests performed at the University of Washington have indicated minimal dependence on temperature, and little drift over time. The cool-down setup has been in place for over one year, with a drift of ~14% in the constant a. During this time however, the electronics were not operated in a stable manner. There were several controlled and emergency power outages. For this reason, the constants are routinely extracted to avoid problems associated with electronic drift.

159

<center>**Appendix 3**</center>

A3.1 Shaper/ADC Board

The Shaper/ADC is a custom 6U VME-based fast shaper/peak-detect ADC. This eight channel board contains switchable input coupling and programmable input attenuation. Each channel has a four-stage integration shaping network. Additionally, each channel has an independently controlled level crossing discriminator. The peak detection circuit consists of a transistor buffered, dual-differentiating network. Shaped pulse conversion is accomplished via a 12-bit ADC and read out through the standard VME bus. The board also contains status monitoring, and two scalers. The board can be run independently, or in parallel with additional boards, and is controlled through an Altera 7192 Field Programmable Gate Array (FPGA).

The board was developed for the emiT experiment [79] as the acquisition hardware for the data collected from silicon PIN diode detectors. Using this board for the NCD program required modification to accept proportional counter signals. A typical PIN diode signal is less than a microsecond in width while the NCD pulses can reach up to 4 μs. The primary modification was simply longer integration time constants.

The decision to design and build this hardware was based on the economics of 64 ADC channels and application requirements. Experiment constraints for emiT required both the detectors and the electronics to be

<center>160</center>

elevated to 30-37kV. For this reason, the board was designed to be compact, and capable of remote operation and monitoring through a fiber-optic link to a standard VME bus. The VME interface was chosen due to its simplicity and the flexibility it allowed in the design process and implementation.

Board construction has proven financially acceptable, with costs running $150/channel for a production run of 20 boards (160 channels). This figure includes the cost of board layout, prototyping, tooling charges, and component costs. The cost of populating the boards is not included, and did not represent a significant dollar amount due to our use of in-house labor, and existing surface-mount population equipment. A comparable NIM-based system easily exceeds $1000/channel for a similar number of channels, and does not provide the same flexibility as a custom design.

The board is an eight layer, VME-standard 6U module, consisting of a combination of through-hole and surface mount components. The choice in using an admixture of component packages was driven by product lead-time and costs. The board is divided into a digital and an analog portion, each with a separate ground plane. The digital realm contains the buffers and logic necessary to run the board and interface to the VME bus. The digital area also includes the peak-detect network, and discriminator components. The majority of the digital logic is contained in the FPGA, and is capable of being reprogrammed. The analog realm consists of the shaping network, and ADC circuitry. During the board layout procedure, special care was taken to minimize the proximity of analog and digital signal lines.

The board contains eight analog signal inputs that are independently jumperable to either capacitive coupling, or 50 input termination. The discriminator outputs for the eight channels are available through a D-Sub connector for timing information, or connection to an external scaler. The board also contains two connections which allow several boards to be interfaced together. The standard connectors P1 and P2 are used to connect the board to the VME bus. See Figure A3.1 for a description of board inputs and outputs.
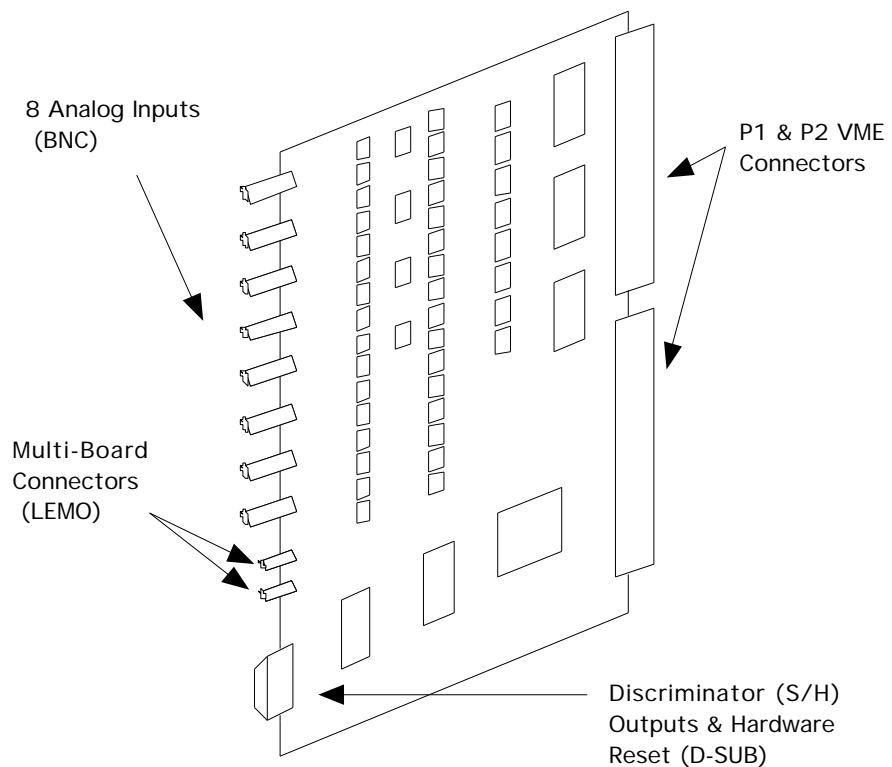
Figure A3.1: Shaper/ADC board connections.

A3.2 Input Attenuation / Shaping / Peak-Detection Networks

The board was designed to accept negative pulses from 5 to 175 millivolts in amplitude (see Figure A3.2). In order to allow adjustment of the dynamic range of the board, a programmable attenuation network was added. This network allows for individual channel gain adjustment via VME control of an on-board register. The register sets an LF13331 analog switch which selects parallel combinations of attenuation resistors prior to the first stage of shaping. This allows the shaping stages to operate in a near unity-gain manner while yielding a front-to-end attenuation of 60-100% of the input pulse. Individual channels can also be remotely disabled with this switch.

The shaping network for the NCD Shaper/ADC boards consists of four successive 4.0 μs integrations, and a 50 μs preamp tail cancellation. The emiT time constants require a much shorter 0.5 μs integration time. The integrations are primarily done by MAX437 op-amps. Figure A3.3 shows a test input, and its corresponding shaped pulse after the fourth integration stage.
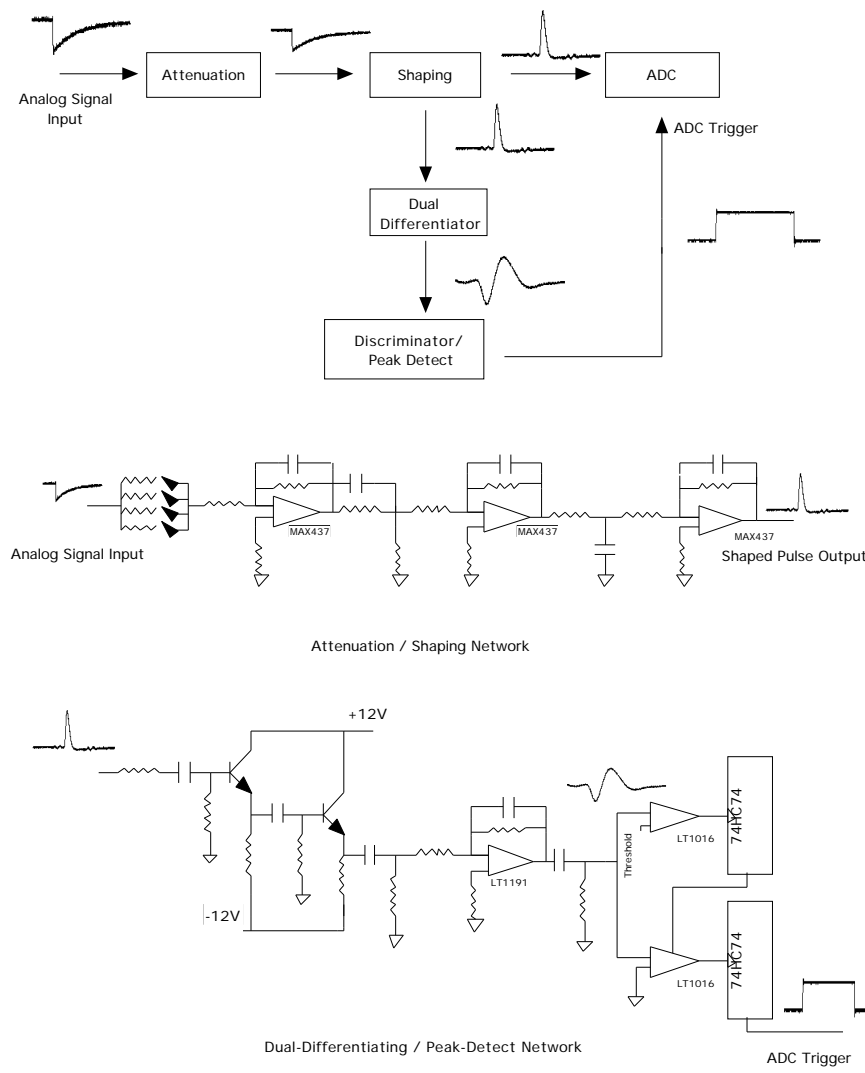
Figure A3.2: Shaper/ADC signal flow and pulse shapes at various stages of the shaping and peak-detect circuits.
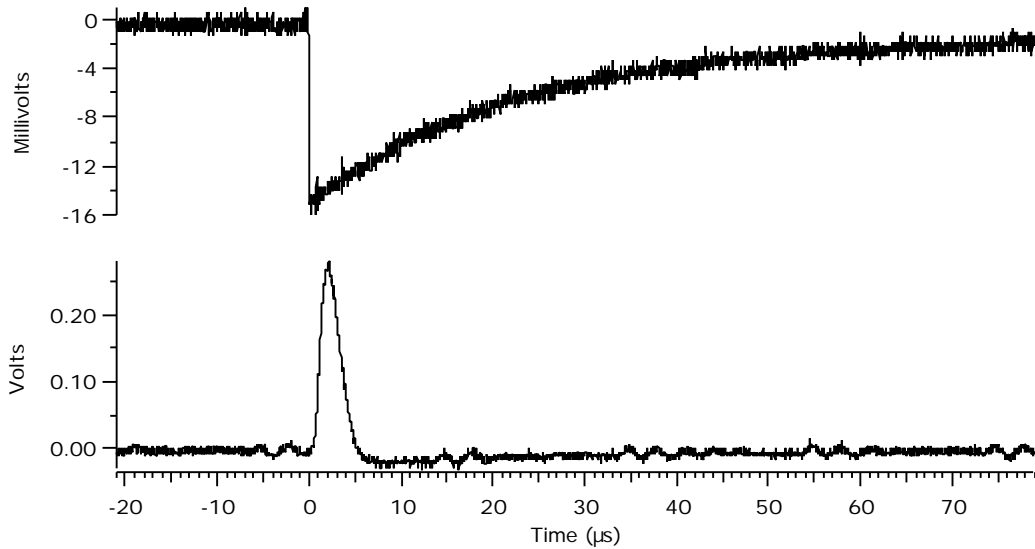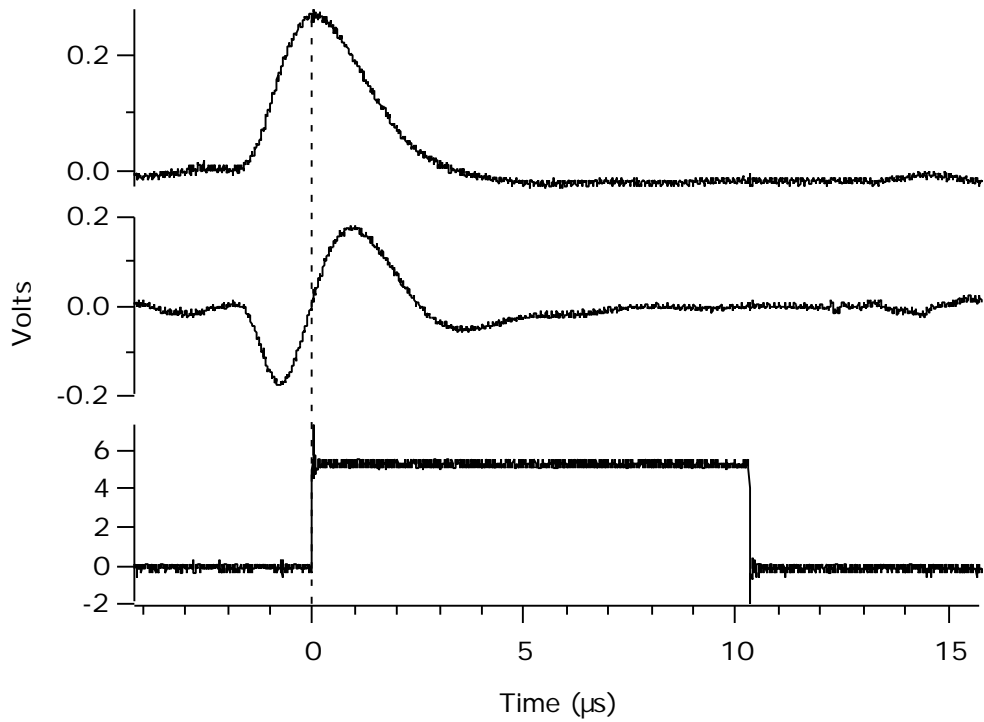
Figure A3.3: The top waveform is an injected pulser signal with a 0.5 μs risetime and a 20 μs tail. The bottom waveform is the shaped signal (emiT time constants) at the input to the ADC.

Peak detection is accomplished with the use of a transistor buffered network. This provides a steep-sloped bi-polar pulse, centered on the peak of the shaped signal. The differentiated signal is amplified using a LT1191 op-amp, and fed to a comparator. The signal is first compared to a DC level provided by a programmable buffered AD7226 DAC. A signal of sufficient amplitude then results in a Sample and Hold (S/H) assertion when the differentiated shaped pulse crosses zero. This method allows for user-defined pulse height discrimination with minimal S/H timing walk. Figure A3.4 shows a differentiated shaped pulse, and the S/H assertion in relation to the uni-polar shaped pulse.

165

Figure A3.4: The relative positions in time of the shaped pulse (top), the bi-polar pulse used to detect the peak of the shaped pulse (middle), and the S/H signal used to trigger the ADC (bottom) for the emiT time constants.

A3.3 Board Logic

The board operational logic and the VME interface logic were programmed into an Altera 7192 FPGA. This 160 pin device was socketed on the board in order to facilitate removal and reprogramming. The logic was designed and compiled into an Electronic Design Interchange Format (EDIF) using Cadence , a CAD-based electronic design and simulation system. The project was then compiled into a device-specific Programmer Object File (POF) with the use of MAX+Plus

166

II   software. Finally, the POF was used to program the logic into the FPGA using a Data I/O   chip burner.

The operational logic is responsible for defining board run modes as well as monitoring board activity and status. There are two distinct modes in which the board can be operated. The mode of each channel can be controlled separately, allowing the board to run selected channels in one mode, while simultaneously running a subset of channels in another mode. This admixture is set via the VME interface, and does not require the removal and reprogramming of the FPGA.

The first mode (Independent Mode) operates the eight channels on a board independently. An event on a channel asserts an inhibit only on the triggered channel. This channel then remains in the inhibited state until its ADC has been read, however the remaining channels on the board are not affected. In the second mode (One-Shot Mode), an event asserts an inhibit on all channels set to run in this mode. These channels remain locked-out until the ADC on the active channel has been read. In either mode, the number of effective channels can be increased by chaining several boards together via the multi-board connectors.

An external input and VME-controlled fast clear have also been incorporated into the operational logic. An assertion on either of these lines reverts all channels to a non-inhibited state without altering the mode in which they are operating.

The FPGA is also programmed to monitor board status. Data available registers and operational mode registers enable remote real-time information as to the current status of the board. Additional features include a 28 bit scaler which counts the OR'd discriminator triggers of all 8 channels. A second 12 bit scaler has been programmed into the Altera, and is capable of being remotely connected to count discriminator triggers on any one of the 8 channels.

A3.4 VME Interface

The VME interface was designed at Los Alamos in accordance with IEEE 87 specifications. Since there is no on-board buffered memory, data must be read out on an event-by-event basis. Therefore, the board operates in a polling mode, placing the major speed constraint on how quickly the data can be read-out once an event has initiated a trigger. This eliminates the need for an individual board to request service, and minimizes VME reads/writes prior to data transfer. The interface retains VME interrupt capabilities, but these have not been utilized.

The interface uses only 16 addressing lines (A0-A15), and 16 data lines (DO-D15). This minimized the number of on-board buffers required, and allowed for the allocation of board real estate to other components. It also allowed for a greater number of input and output pins on the FPGA to be dedicated for future expansion.

Individual board addresses and address modifiers are all programmed directly into the FPGAs. Changing a board's address is accomplished by either changing the FPGA, or reprogramming the FPGA with a new address.

A3.5 Operational Characteristics

The emiT experiment collects data at a rate below 10Hz, and the NCD rate is anticipated to be much lower. As a result the board was designed for operation in the few Hz region. Figure A4.5 shows a comparison of the observed to actual rates using a test pulser. This data was fit to the Knoll model of nonparalyzable response [80], yielding a deadtime of 87 μs. These measurements are strongly dependent on the machine running the data acquisition software. Ultimately however, minimization of the deadtime is limited by the length of the S/H assertion, which is currently set to 40 μs. Optimization of DAQ code as well as running with the faster PCI Bus as opposed to the current NUBUS would result in a lowering of the measured deadtime.

Operating at 60 Hz, the board resolution was 5-7%. While this was acceptable, a few modifications were made. Replacing the electrolytic filter capacitors on the power lines with tantalum capacitors, and changing the VME power supply to a non-switching unit had a notable effect. Typical channel resolution was improved to about 3%. Additionally, the non-switching power supplies enabled the thresholds to be run at significantly lower values. Figure A3.6 shows a pulser spectrum.
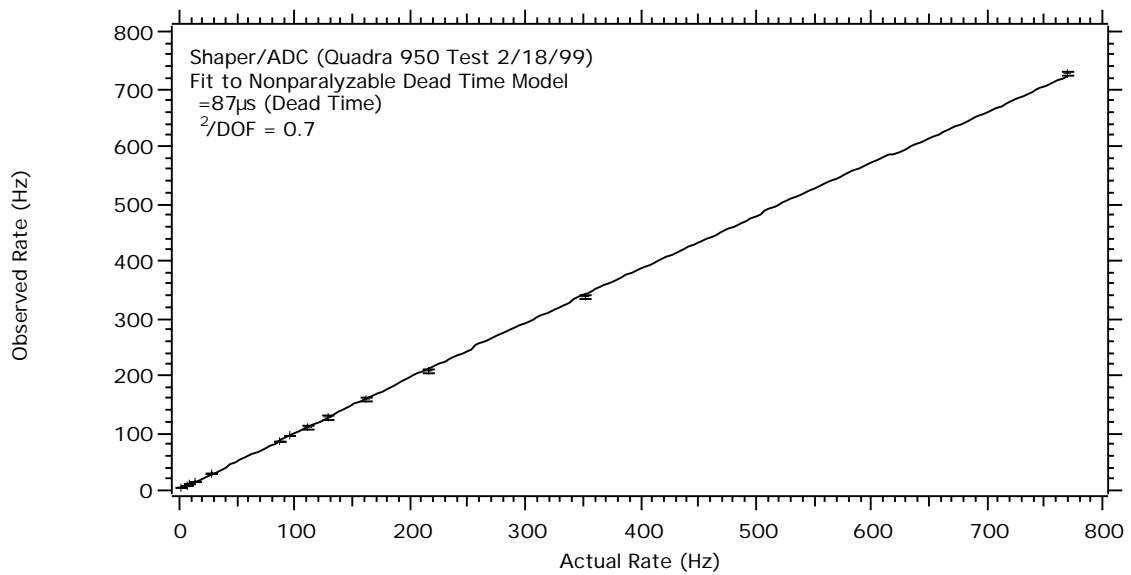
**Figure A3.5: Comparison of observed to actual rates.**
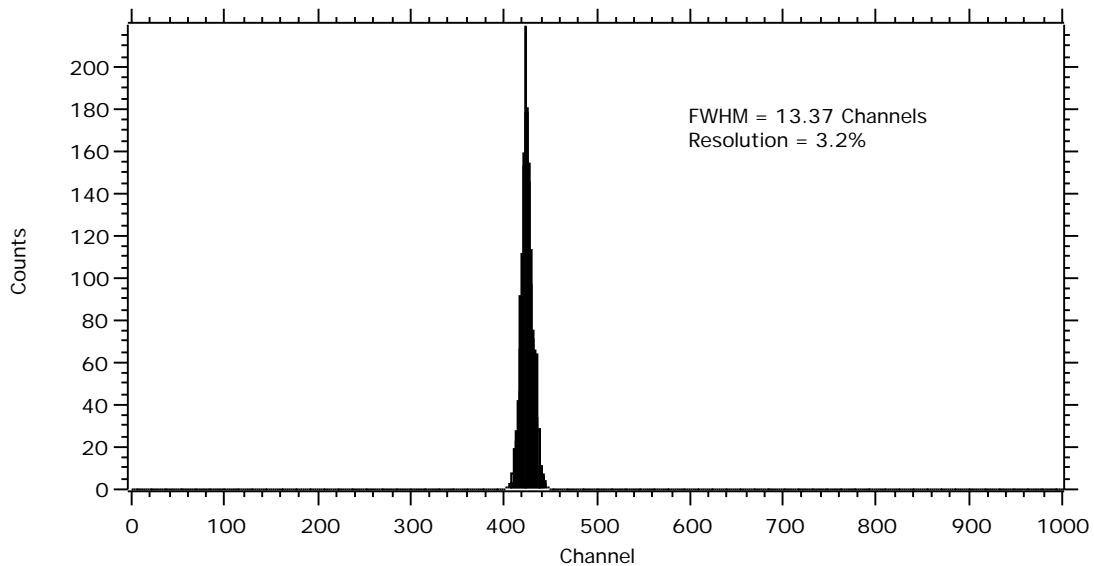
Figure A3.6: Channel resolution

170

A3.6 Future Directions

Revision B of the Shaper/ADC board has been designed and prototyped. This revision incorporates several changes to better accommodate both the emiT and NCD experiments. Additionally, modifications were included to enhance the performance characteristics of the board.

The shaper/ADC board was particularly prone to damage in the emiT experiment as a result of HV discharge. Revision B incorporates a fiber-optic readout enabling the board to be isolated from the HV. The threshold of revision A was also determined to be "spongy." The peak-detect network was re-designed, prototyped and tested, resulting in a sharper threshold included in the revision B design. The remote controlled gain of revision A was susceptible to induced noise. A new design increased the dynamic range of the gain while minimizing noise.

Revision B also incorporates a much larger FPGA to control the VME interface and board logic. The larger FPGA allows for each channel to have an independent scaler. Additionally, a floating scaler has been programmed into the FPGA which allows for direct measurement of independent channel deadtime. The operational logic of the board has been reworked to eliminate the primary source of this deadtime – the S/H assertion. The new logic allows the board to run in a manner limited only by conversion and read-out times.

Finally, several undesirable layout characteristics were identified in revision A. These resulted in induced noise in certain channels of the board. Special attention has been paid in revision B to correct these problems. One

171

particular difficulty noticed in revision A was excessive "read-induced" noise associated with improper connections of the analog and digital ground planes. As a result, VME bus-induced noise could be seen on the analog side of the board, resulting in relatively poor resolution at high DAQ rates. In order to compensate for this, a low-pass filter/isolator was placed before the analog input to the board in the cool-down phase electronics (see Figure 4.3). The schematic for the filter/isolator is shown in Figure A3.7. The shaper/ADC board resolution of a calibration pulser is shown in Figure A3.8, demonstrating the resolution with and without the filter/isolator.
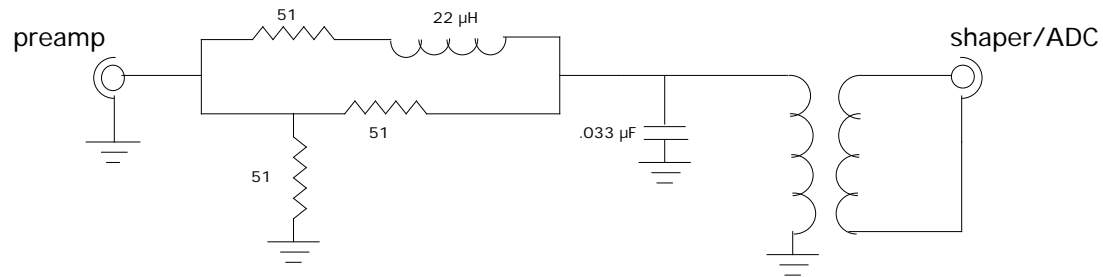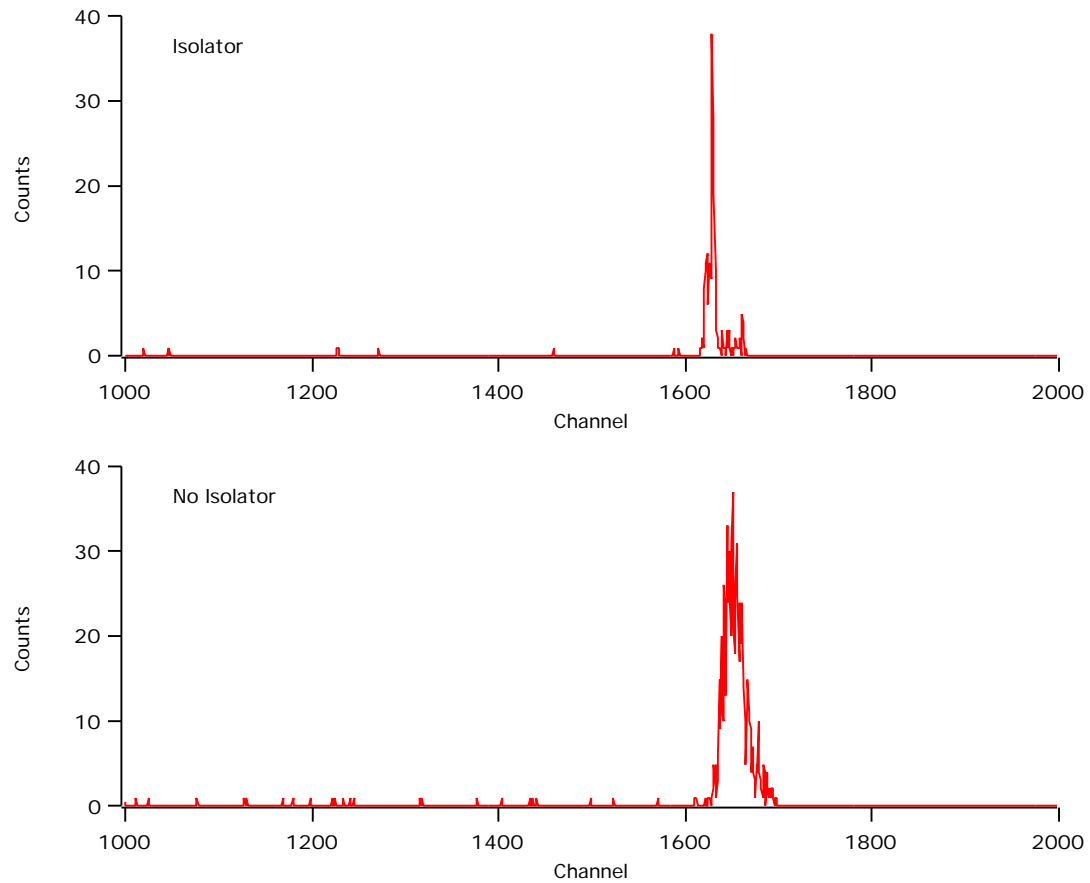
Figure A3.7: Filter/Isolator schematic

Figure A3.8: Pulser resolution with cool-down phase filter/isolator (top), and without (bottom).

A4.1 Monte Carlo Simulation of Fast Neutron Shielding

In Chapter 4, the fast neutron contamination of the regions used for the determination of the bulk U and Th content was discussed. The anticipated rate of these events was calculated, but an absolute measurement is obviously desirable. By attenuating the fast neutrons underground, we could compare the observed data rates with previously measured rates in an attempt to quantify the fast neutron component. It was decided to estimate the amount of shielding required to attenuate these neutrons, and determine the feasibility of assembling such a setup at the underground SNO facility.
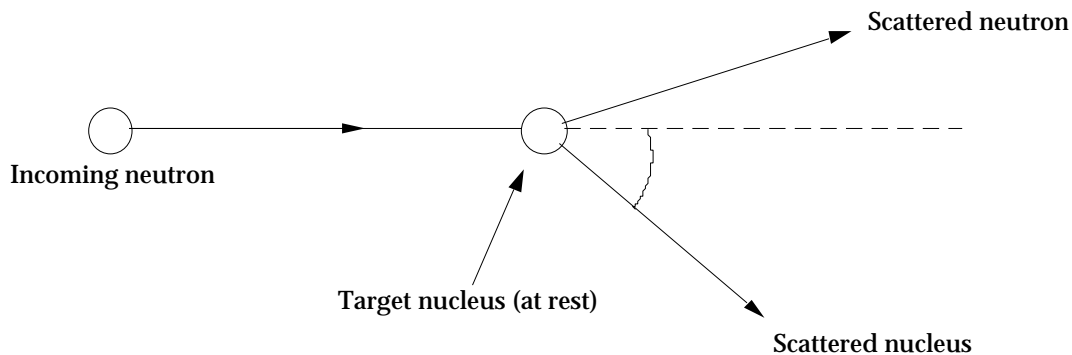
Figure A4.1: Elastic scattering of a neutron.

The dominant interaction for fast neutrons is elastic scattering (At very high neutron energies, the collisions become inelastic – these are not treated here.). Figure A4.1 shows a scattering diagram in the laboratory reference frame.

The transfer of energy from the neutron to the scattered particle is a purely kinematic two-body problem, yielding the relation in Equation A4.1 between the energy of the incident neutron (E_n) and the energy of the recoiling nucleus (E_R).

$$E_R = \frac{4A}{(1+A)^2} (\cos^2 \theta) E_n \qquad (A4.1)$$

Maximal energy transfer therefore occurs for the lightest target particle (A=1), making materials containing large amounts of hydrogen the moderator of choice. The interaction path length (λ) of a neutron in a material characterized by a density N (#/m³), and elastic scattering cross section σ, is given by $\lambda = 1/N\sigma$. Conservation of energy and momentum coupled with the calculated interaction path length are therefore all that is required for a simple treatment of scattering.

A Monte Carlo simulation was constructed in which an incident neutron multiply scatters from protons in a material with a hydrogen density of water (or paraffin). The scattering angle of the proton is randomly generated, and the neutron direction, energy, and new path length calculated from this angle (The elastic scattering cross section for hydrogen for neutron energies from 0.01 to 10 MeV was incorporated into the code to update the interaction path length after each scattering event). The code simulated a beam of 5 MeV neutrons incident on a semi-infinite slab, and calculated the transmission efficiency at various depths. Neutrons which either back-scattered out of the moderator, or had their energy attenuated below 1 MeV were no longer tracked. The code predicted that 90% of the incident neutrons would be attenuated by 0.25 m of shielding, 54% would be attenuated by 0.2 m, and 24% would be attenuated by 0.13 m.

In a test of the Monte Carlo results, an AmBe source was placed near an NCD to characterize the rate of events > 1MeV in a moderated and unmoderated setup. The moderator geometry utilized 0.13 and 0.2 m thicknesses of paraffin wax (~7.7×10^28 ^{1}H/m^3) placed between the source and an NCD. Figure A4.3 shows the T vs. E space of an unmoderated run (top frame), and a run with 0.20 m of moderation (bottom frame). There are 46.0 ± 6% fewer events in the moderated phase space. The shielding simulation predicts a 54% attenuation for this thickness of moderator.
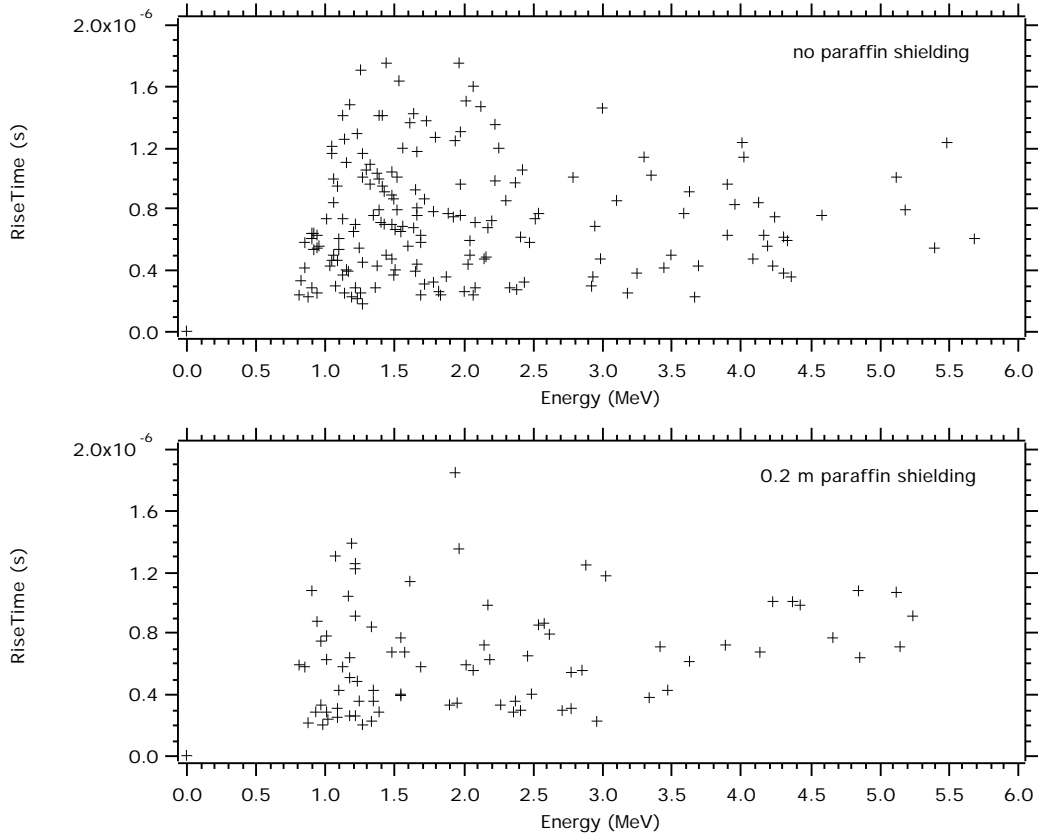

Figure A4.2: Rise time versus energy plot using an AmBe source. Top frame unmoderated, bottom frame utilized 0.20 m of paraffin moderator.

A similar test was run with 0.13 m of paraffin wax between the NCD and the source. The number of events recorded above 1 MeV indicated an attenuation of 29.8 ± 5% in comparison to the unmoderated run from above. The code predicts a 24% attenuation. The slight discrepancy in both cases may be the result of a decreased detection efficiency due to neutrons being scattered away from the detector.

The results of the Monte Carlo indicate that 90% of the anticipated underground fast neutron flux can be attenuated by surrounding a counter or string by 0.25 m of water. As was mentioned in Chapter 4, surrounding the entire cool-down array is not feasible, but surrounding a 5 – 6 m string is not unreasonable. Water is chosen for its availability underground. Amassing and transporting the required equivalent of paraffin wax presents several difficulties. Using water requires little more than 1 foot cubic boxes, and several hundred balloons. The shielding can be assembled rapidly "in place," and disassembled almost as easily.

A4.2 Monte Carlo simulation of "End-Effects"

In Section 4.5, the problems associated with the alpha decay of ^{210}Po on the inside surface of NCDs was discussed. One particular concern is the contamination of the neutron "background free window" – a region in the rise time versus energy phase space which is populated by neutrons, but not

accessible to alpha particles and Compton events based on pulse topology. An alpha particle which is emitted near the endcap region of an NCD, where electron-ion pair multiplication is attenuated by the presence of the quartz field tube, may give rise to an abnormal ionization event in the counter. The topology of this event would be a superposition of ionization from both a uniform and an attenuated component, and may contaminate the background free window.

In order to determine how many of these events are likely to occur, a Monte Carlo simulation was written to predict what fraction of decays will result in the alpha entering the active volume of the counters. The code only considers alphas which deposit the full 5.3 MeV of energy in the gas (80% of all ^{210}Po decays), and have a range of about 23.1 mm in the NCD gas mixture. The code randomly generates event positions on the surface of an NCD in the endcap region. The direction cosines of the alpha are also randomly generated, and the final position of the alpha is calculated. The number of events which result in the alpha entering the active volume are then recorded.

The code predicts that 12.2% of ^{210}Po decays which result in the deposition of 5.3 MeV of energy in the gas will enter the active volume of the counter. The code does not account for the fraction of events which do not deposit their full energy in the gas. This contribution is estimated to be small from solid angle arguments – on order of 2% (20% of ^{210}Po decays with 12% probability of entering the active volume). It should be noted that the simulation calculates the percentage of decays starting in the attenuated field region, and entering the active volume. There should be an equal number of events starting in the active

volume and entering the attenuated field region which give rise to the same pulse topology. The ultimate number of events is therefore increased by a factor of two.
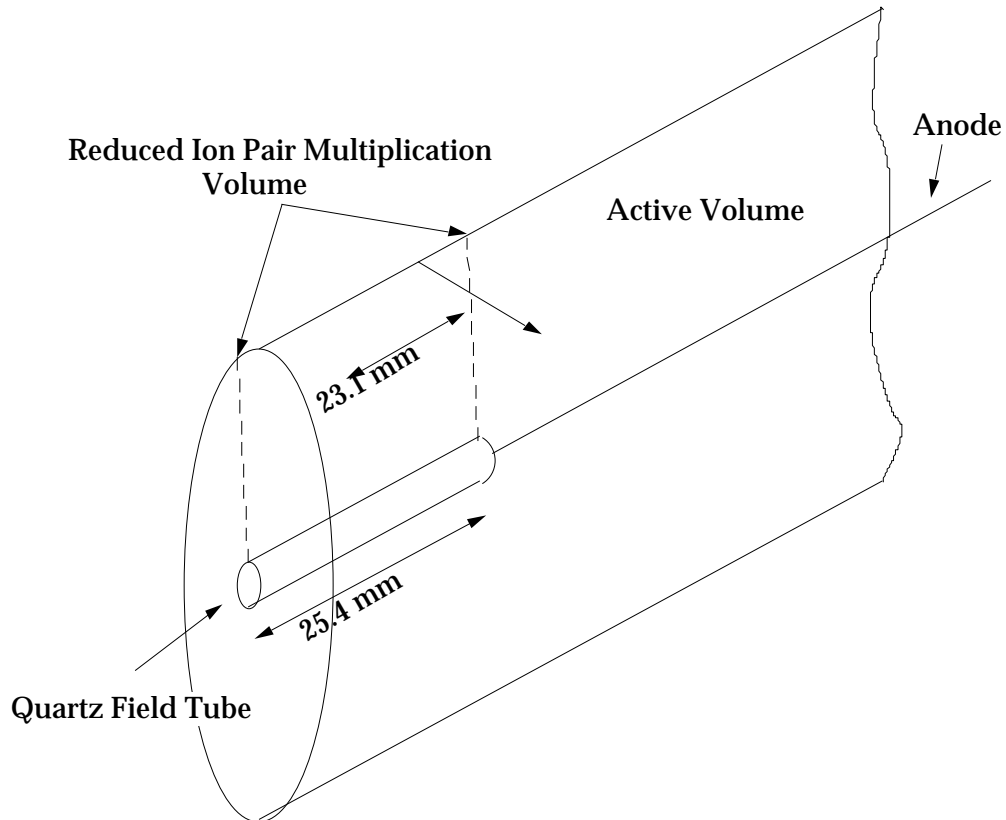

Figure A4.3: Geometry of the "end-effect" Monte Carlo simulation.

Bibliography

[1] A. Pais, *Inward Bound*, p.158, Oxford University Press, Oxford (1986)

[2] W. Pauli, Address to the Physical Institute of the Federal Institute of Technology – Zurich (1930)

[3] H.R. Crane, Rev. Mod. Phys. 20, 278 (1948)

[4] R. Davis, Phys. Rev. 86, 976 (1952)

[5] G.W. Rodeback and J.S. Allen, Phys. Rev. 86, 446 (1952)

[6] F. Reines and C.L. Cowan, Phys. Rev. 92, 830 (1953)

[7] C.L. Cowan *et al*, Science, Vol. 124, No. 3212, P.103 (July 20, 1956)

[8] G. Gamow, Phys. Rev., **53**, 595 (1938)

[9] H.A. Bethe, C.L. Critchfield, Phys. Rev., **54**, 248 (1938)

[10] A. Unsold and B. Baschek, *The New Cosmos* P. 217, Fourth Completely Revised Edition, Springer-Verlag (1991)

[11] *ibid* P. 212.

[12] J.N. Bahcall, *Neutrino Astrophysics* p. 58, Cambridge University Press (1989)

[13] J.N. Bahcall and M.H. Pinsonneault, with an Appendix on the Age of the Sun by G.J. Wasserburg, Rev. Mod. Phys. **67**, 781 (1995)

[14] J.N. Bahcall and M.H. Pinsonneault, Rev. Mod. Phys. **64**, 885 (1992)

[15] S. Turck-Chièze and I. Lopes, Astrophys. J. **408**, 347 (1993)

[16] C. R. Proffitt, Astrophys. J. **425**, 849 (1994)

[17] A. Kovetz and G. Shaviv, Astrophys. J. **426**, 787 (1994)

[18] J.N. Bahcall and R. Ulrich, Rev. Mod. Phys. **60**, 297 (1988)

[19] S. Turck-Chièze, S. Cahen, M. Cassè and C. Doom, Astrophys. J. **335**, 415 (1988)

[20] I.J. Sackmann, A.I. Boothroyd, W. A. Fowler, Astrophys. J. **360**, 727 (1990)

[21] S. Basu *et al.* Astrophys. J., **460**, 1064 (1996)

[22] S. Tomczyk *et al.* Solar Phys., **159**, 1 (1995)

[23] J.N. Bahcall, M.H. Pinsonneault, S. Basu, J. Christensen-Dalsgaard, Phys. Rev. Lett., **78**, 171-174 (1997)

[24] A. Cumming and W.C. Haxton, Phys. Rev. Lett., **77**, 4286 (1996)

[25] K.M. Heeger and R.G.H. Robertson, Phys. Rev. Lett., **77**, 3720 (1996)

[26] N. Hata and P. Langacker, Phys. Rev. D, **50**, 632 (1994)

[27] S.P. Mikheyev and A. Yu. Smirnov, Sov. J. Phys. **42**, 913 (1986); Nuovo Cimento **9C**, 17 (1986); L. Wolfenstein, Phys. Rev. **D17**, 2369 (1979)

[28] B.T Cleveland *et al.*, Nucl. Phys. B (Proc. Suppl.) **38**, 47, (1995)

[29] J.N. Bahcall and M.H. Pinsonneault, Rev. Mod., Phys., **67**, 781, (1995)

[30] Y. Suzuki, 4th International Conference on Solar Neutrinos, Heidelberg, Germany, 1997

[31] Y. Suzuki, Nucl. Phys. B (proc. Suppl.), **38**, 54 (1995)

[32] J.N. Abdurashitov *et al.*, Phys. Lett. **B328**, 234 (1994)

[33] W. Hampel *et al.*, Phys. Lett. **B388**, 384 (1996)

[34] S.R. Elliott et al. Preliminary Results from the Russian-American Gallium Experiment Cr- Source Measurement

[35] D. Vignaud et al. Proceedings of the IV International Workshop on Theoretical and Phenomenological Aspects of Underground Physics

[36] World Wide Web homepage: http://www.sns.ias.edu/~jnb/

[37] H. Chen, Phys. Rev. Lett., **55**, 1534 (1985)

[38] F.J. Kelly and H. Uberall, Phys. Rev. Lett. 16, **145** (1966)

[39] J.N. Bahcall, Phys. Lett., **13**, 332 (1964)

[40] SNO STR 98-001

[41] P.J. Doe *et al*, Construction of an Array of Neutral-Current Detectors for the Sudbury Neutrino Observatory, SNO-STR-95-023

[42] ibid

[43] J. B. Wilhelmy, New Monte Carlo Calculations for Neutron Detection in SNO, SNO-STR-92-058

[44] A.W.P. Poon, Energy Calibration of the Sudbury Neutrino Observatory using Monoenergetic Gamma-Ray Sources, PhD. Dissertation; University of British Columbia (1998)

[45] W. Diethorn, NYO-6628 (1956)

[46] A. Hime, Operating Constraints and Performance of a 3He Neutral Current Detector array in SNO

[47] Ref. 41

[48] L.C. Longoria *et al*, NIM **A299**, 308 (1990)

[49] G.F. Knoll, *Radiation Detection and Measurement* P. 200, J. Wiley and Sons (1979)

[50] A. Goldschmidt and A. Hime, private communications

[51] A. Hime, private communications

[52] Ref. 49 P. 96

[53] R.G.H. Robertson and T.D. VanWechel, Log Amplifier Application in SNO NC Detectors, unpublished (1997)

[54] Ref. 41

[55] G. Miller, J. Wilhelmy, and S.R. Elliott, private communications

[56] R.K. Heaton M.Sc. Thesis, Queen's University (1988)

[57] V. McLane, C.L. Dunford, P.F. Rose, *Neutron Cross Sections Volume 2*, Academic Press Inc. (1988)

[58] A Rindi, F. Celani, M. Lindozzi, and S. Miozzi, NIM **A272**, 871 (1988)

[59] E.A. Lorch, Int. J. Appl. Radiat. Isotopes, **24**, 588 (1973)

[60] Ref. 49 p. 574

[61] G.J. Feldman, R.D. Cousins, Phys. Rev. **D57**, 3873 (1998)

[62] W.H. Press, B.P. Flannery, S.A. Teukolsky, W.T. Vetterling, *Numerical*

Recipes in C P. 552, Cambridge University Press (1988)

[63] P. Belli *et al.*, Nuovo Cimento, **101A**, N.6 p959

[64] V. Chazal *et al.*, Lycen 9736 (1997)

[65] W.F. Davidson *et al.*, Background Measurements in the Creighton Mine
      Annex 10 to the SNO "White Book" (1987)

[66] SNO Collaboration, The Sudbury Neutrino Observatory, to be submitted to
      NIM

[67] E.D. Earle, and E. Bonvin, Measurements of Th and U in Acrlic for SNO,
      SNO-STR-92-061

[68] J.A. Dunmore, Background Neutron Sources to the
      Neutral-Current Signal in SNO, REU Research Paper, 1998

[69] T.J. Radcliffe, Fast Neutrons from Muon Spallation in
      the SNO Detector, SNO-STR-93-023 (1993)

[70] S. Brice, private communications

[71] R.G.H. Robertson, private communications

[72] The Super-Kamiokande Collaboration, Measurement of the Solar Neutrino
      Energy Spectrum Using Neutrino-Electron Scattering, hep-ex/9812011
      (1998)

[73] SNO Water Group, Fall, 1998 Collaboration Meeting

[74] A.B. Balantekin, and F. Loreti, Solar and supernova neutrino physics
      with the Sudbury Neutrino Observatory, Phys. Rev. D45, 1059 (1992)

[75] P.M. Thornewell, Detectors for the Sudbury Neutrino Observatory,
      D.Phil Thesis, Oxford (1997)

[76] A. Hime, Extracting the NC Signal from D_2O+NCDs,
      SNO Collaboration Meeting (May 1997), NC Signals and Backgrounds
      (June 1999)

[77] P.J. Doe, *et al.*, Calibration and Neutral-Current Detectors II
      SNO-STR-94-004 (1994)

[78] S.R. Elliott, et al., 3He Neutral Current Detectors at SNO,
      Invited Talk - New Era in Neutrino Physics, Tokyo, Japan (1998)

[79] L.J. Lising *et al.*, Intersections between Particle and Nuclear Physics: 6th Conference, ed. T.W. Donnely (AIP, New York, 1997), P. 399

[80] Ref. 49 P. 97